Atomic structure, electronic states and relaxation dynamics in photovoltaic materials and interfaces from photoemission-related spectroscopies

Min-I Lee

université PARIS-SACLAY

NNT : 2018SACLS220

UNIVERSITÉ PARIS SUD
Comprendre le monde, construire l'avenir

Atomic structure, electronic states and relaxation dynamics in photovoltaic materials and interfaces from photoemission-related spectroscopies

Thèse de doctorat de l'Université Paris-Saclay
préparée à l'Université Paris-Sud

École doctorale n°564 Physique en Île-de-France
Spécialité de doctorat: Physique

Thèse présentée et soutenue à Orsay, le 10 Juillet 2018, par

Min-I Lee

Composition du Jury :

Jean-Marc Themlin Professeur, Aix-Marseille Université	Président
Wendy Flavell Professeur, University of Manchester	Rapporteur
Karol Hricovini Professeur, Université de Cergy-Pontoise	Rapporteur
Emmanuelle Deleporte Professeur, Ecole Normale Supérieure de Cachan	Examinatrice
Antonio Tejeda Directeur de Recherche, Université Paris Sud	Directeur de thèse
Pere Roca i Cabarrocas Directeur de Recherche , Ecole Polytechnique	Co-Directeur de thèse
Pierre Audebert Professeur, Ecole normale supérieure de Cachan	Invité

Thèse de doctorat

Acknowledgment

First of all, I wish to express my gratitude to my supervisor, Antonio Tejeda, for giving me this great opportunity to work with him on this interesting subject, for leading me into the fascinating world of research by sharing his knowledge and experiences, and, especially, for giving me support and constant encouragement all along the past three years. Simultaneously, I would also like to show my sincere appreciation to my co-supervisor, Pere Roca i Cabarrocas, for sporting me with my Taiwan Paris-Sud scholarship and advising me in the research. Without these two wise and generous professors, I will not finished my thesis so smoothly and successfully.

Secondly, I would like to thank to Taiwan Ministry of Education and Université Paris Sud offer for a Taiwan Paris-Sud scholarship supporting my thesis for the past three years. Thanks to this program, I had a chance study my thesis in France. Of course, I would like to thank to all the people who have helped me in this scholarship program. With out their kind supports I would have not been able to complete my PhD here in France. Simultaneously, I would also like to thank all the funding that has supported my research, especially GOT Solar project, GDR HPERO, SOLEIL synchrotron, and COST action MP1306 - EUSpec.

For all the materials studied in this thesis, I would like to show my appreciation to our collaborators, the group of Emmanuelle Deleporte in Laboratoire Aimé Cotton (LAC) , especially, to Ferdinand Lédée and Gaëlle Trippé-Allard, who provided us the hybrid perovskites for our studies. Also, I would also like to thank to our cooperators Olivier Plantevin (CSNSM) and Alice Defresne (LPICM), who provided the amorphous silicon heterostructures for our studies.

For the inverse photoemission measurements, I would like to show my appreciation to our cooperators, the group of Jean-marc Themlin in Institut Materiaux Microélectronique Nanosciences de Provence (IM2NP), Marseille, in collaboration also with Younal Ksari, Luca Giovanelli, Hela Mrezguia, and Hamza Khelidj. During my stay in Marseille, they advised and helped me a lot. Without their help, I would have not been able to perform our nice data of conduction band of PEPI. For the two photon photoemission measurements, I would like to acknowledge our collaborator, Luca Perfetti and Evangelos Papalazarou in FemtoARPES lab, also with the help of Zailan Zhang, Zhesheng Chen, and Marco Caputo. In addition,

for our transport measurements, I would like to thank our cooperators, the group of Claude Pasquier, also with the help of Pascale Auban-Senzier and Miguel Monteverde.

For our experiments in SOLEIL synchrotron, I would like to appreciate all the help from local contacts of each beamtime we had. Especially during the beamtime in the CRISTAL beamline, I would like to thank Pierre Fertey and Claire Laulhe for their helpful support during all the experiments and during my analysis. I would also like to thank the help and support of our Group members in LPS, David Le-Bolloch, Vincent Jacques, Arlensiú Celis, Isabel Gonzalez-Vallejo, Maya Narayanan Nair, Ana Barragán, and Haoran Wanglan, as well as supports from Amina Taleb-Ibrahimi in SOLEIL synchrotron, during all my measurements and analyses.

The theoretical calculation done in this thesis were possible thanks to the support from EUSpec, in which I was introduced by Didier Sébilleau and Keisuke Hatada. Thanks to the guiding of the group of Hubert Ebert at Ludwig- Maximilians-Universität München (LMU) in Munich, Germany, especially with the guide of Sebastian Wimmer, and Alberto Marmodoro, I learn to use the SPRKKR code. At the same time, I would also like to thank our cooperator, Jan Minar and Saleem Khan from University of West Bohemia at Plzeň in Czech Republic, to advice and support for our photoemission simulations and band structure calculations. Also, I would like to thank to the help of Alberto Zobelli for helping me dealing with the cluster in LPS.

I would also like to thank to my mentor, Alexandre Gloter, and my scientific tutor, Pascale Foury-Leylekian for their kindness guiding during my three years studies.

Finally, I would like to thank to all my family members and friends for giving their full support in my academic pursuits. I would like to thank especially my dad, who help me to seize this opportunity to engage in a PhD, and the strong sports from my mom, my aunts, my sisters and brother, and my grandparents. Also, I would like to thank my boyfriend, Cheng-Yu Han, who came to study PhD with me and gave me all the support at anytime. In the end, I would like to conclude with my special thanks in advance to anyone who is reading this thesis for your patience and I hope you will enjoy it.

Abstract

The efficiency of the photovoltaic process depends on the electronic band structure of the active material and the charge carrier dynamics. In this thesis, we have studied how these issues are related to the atomic structure of the materials for two types of technologies of solar cells, namely silicon heterojunction solar cells, and hybrid organic-inorganic perovskite solar cells.

In silicon heterojunction solar cells, we have analyzed the impact of defects on the electronic properties of amorphous silicon heterojunction (a-Si:H/c-Si) by core level and valence band spectroscopies. In particular, we have quantified the number of dangling bonds in the a-Si:H layer upon irradiation, we have identified the electronic states associated to them, and have understood the transitions previously observed by photoluminescence.

In perovskite solar cells, we have correlated the atomic structure, the electronic structure and the electronic dynamics for two- and three-dimensional hybrid organic-inorganic perovskites. We have used for this goal a whole panel of complementary techniques: X-ray diffraction, angle-resolved photoemission spectroscopy, inverse photoemission spectroscopy, and time-resolved two-photon photoemission.

In the two-dimensional perovskite $(C_6H_5C_2H_4NH_3)_2PbI_4$, the valence and conduction bands have been determined experimentally and compared to spectral function simulations. In the three-dimensional perovskite $CH_3NH_3PbI_3$, we have again determined the band structure and simulated it. Very broad spectral features have been experimentally observed, which relax the optical transition conditions impacting in the solar cell efficiencies. In both experiments and calculations, we observe that the spectral weight follows a cubic periodicity while the system is structurally in the tetragonal phase. This apparent contradiction is explained by the band broadness, which hides the band folding of the tetragonal distortion. As for the relaxation dynamics, we have observed that the photoexcited carriers thermalize in a subpicosecond time scale through the coupling to organic cation vibrations. At longer timescales (10 ˜ 100 picoseconds), the electron diffusion controls the dynamics. This dynamics is affected by the annealing-induced defects, which localize the photoexcited electrons for more than 300 picoseconds.

Résumé

Cette thèse porte sur des matériaux pour cellules solaires, à savoir les hétérostructures de silicium, qui s'utilisent sur des cellules solaires commerciales très repandues, et les pérovskites hybrides, un matériau photovoltaïque émergent (voir fig. 1). Comme l'efficacité du processus photovoltaïque dépend du transfert de charge dans le matériau actif et de sa structure de bande électronique, cette thèse étudiera ces aspects sur les matériaux préalablement mentionnés par spectroscopies connexes à la photoémission (voir fig. 2).

Cellules solaires à hétérostructures de silicium

Les cellules solaires de silicium en couche mince constituent l'une des solutions possibles à la demande énergétique croissante. Le silicium amorphe hydrogéné (a-Si:H) est particulièrement intèressant pour les cellules solaires. Il peut être utilisé comme couche absorbante intrinsèque, entre deux couches dopées dans une jonction PIN, et il peut être combiné avec du silicium cristallin (c-Si) dans des cellules solaires à hétérojonction [1]. L'efficacité des cellules solaires à hétérojonction a-Si:H a atteint plus de 26%, ce qui se rapproche de la limite théorique d'efficacité de conversion des cellules solaires de Si (29,1%) [2].

L'un des facteurs qui affectent l'efficacité des cellules solaires sont les défauts, qui impactent l'efficacité à travers des états électroniques supplémentaires qu'ils génèrent dans la bande interdite. Une meilleure compréhension des défauts, en particulier dans l'interface entre le c-Si et le a-Si:H pourrait aider à augmenter la tension à vide (V_{oc}) et le courant de court-circuit (J_{sc}) des cellules solaires à hétérojonction, ce qui entraînerait une augmentation de leur efficacité.

Dans cette étude, des défauts ont été introduits par irradiation ionique avec des ions d'Ar. En contrôlant la fluence des ions d'Ar et leur énergie, la profondeur de la région d'impact, c'est-à-dire la localisation des défauts, a été contrôlée. Pour comprendre les états electroniques ainsi introduits, nous avons étudié leur localisation dans les hétérojonctions, leur nombre et leur position dans la bande interdite. Puisque ces défauts sont enterrés, nous les avons étudiés par spectroscopie de photoémission par rayons X de haute énergie (HAXPES). Avec l'HAXPES, les électrons photoexcités peuvent être extraits de différentes profondeurs de l'hétérojonction avec différentes énergies de photons (voir fig. 3). Nous avons étudié les

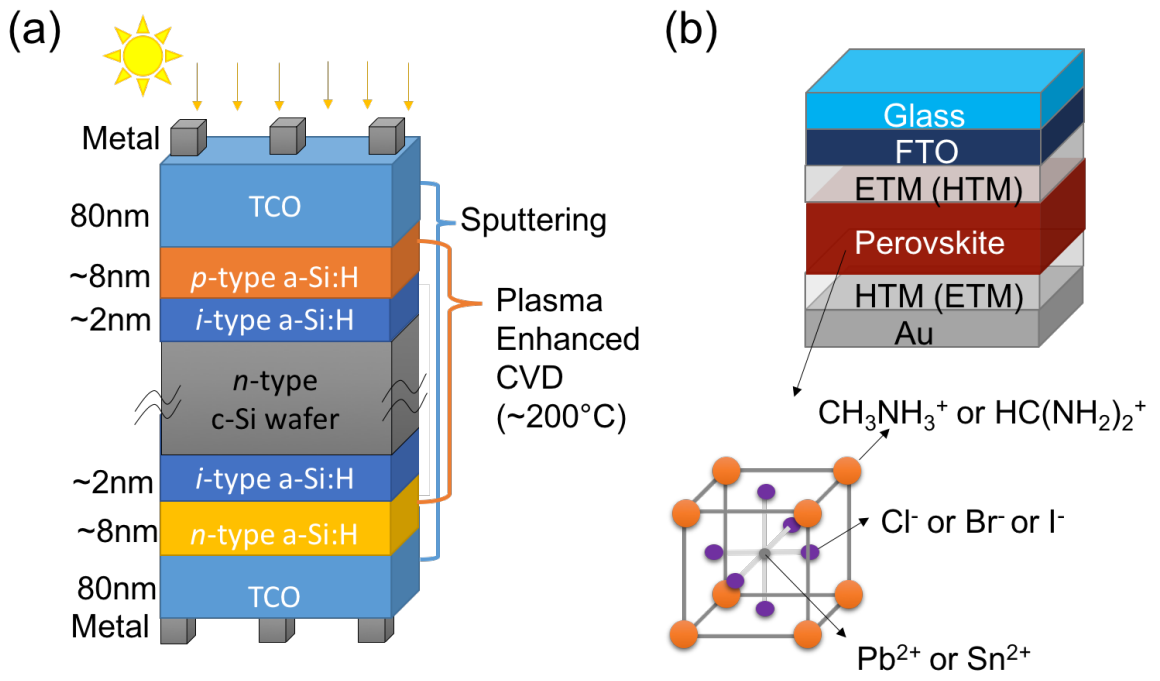

Figure 1: (a) Schéma de cellules solaires à hétérostructure de silicium. TCO est un oxyde conducteur transparent (Transparent Conductive Oxide). (b) Schéma d'une cellule solaire à pérovskite hybride et structure atomique des pérovskites hybrides organiques-inorganiques. HTM est un matériau de transport de trous (Hole Transport Material) et ETM un matériel de transport d'électrons (Electron Transport Material).

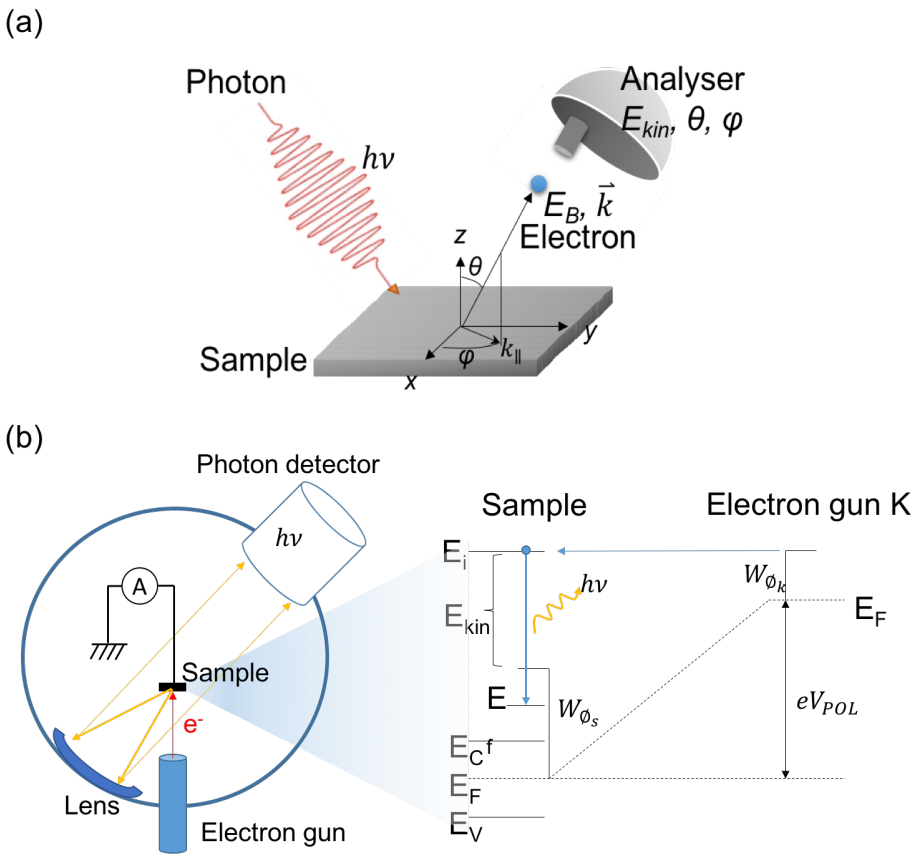

Figure 2: Principales techniques utilisées dans cette thèse. (a) Schéma de principe de la photoémission. Lors de l'absorption d'un photon, les électrons de la bande de valence et des niveaux de cœur peuvent être éjectés. En mesurant l'énergie cinétique de ces électrons, nous pouvons étudier la bande de valence et les niveaux de cœur des matériaux. (b) Principe de fonctionnement de la photoémission inverse. (à droite) Un canon à électrons émet un faisceau d'électrons d'énergie variable (de 8 eV à 18 eV dans notre cas) vers l'échantillon. Un miroir elliptique recueille les photons. (à gauche) Les électrons générés par le canon sont injectés dans les états inoccupés (état initial, E_i) de l'échantillon, et ensuite se relaxent à un état d'une énergie inférieure, toujours dans les états inoccupés (état final, E_f). Un photon est émis et détecté.

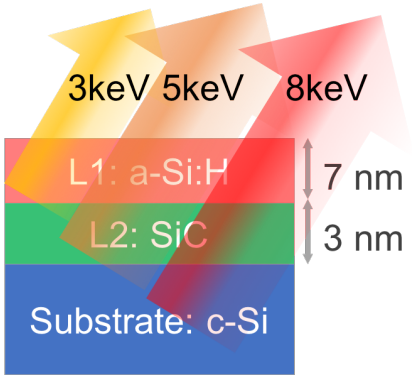

Figure 3: Les électrons photoexcités peuvent être extraits de différentes profondeurs de l'hétérojonction avec différentes énergies de photons dans le range des keV.

différents environnements chimiques des atomes de Si, afin de quantifier les liaisons pendantes genereés par l'irradiation. Par spectroscopie des niveaux de cœur, nous avons découvert que la quantité de liaisons Si-H diminue de 20±5% dans la couche a-Si:H (voir fig. 4(b)). Ces liaisons casseés par l'irradiation deviennent des liaisons pendantes et genèrent des états électroniques à 0,3 eV au-dessus de la bande de valence (voir fig. 4(d) et (e)). La densité d'états ici augmente environ $25 \pm 8\%$, en accord avec l'augmentation du nombre de liaisons pendantes après l'irradiation. Comme la position en énergie de ces états ne permet pas d'expliquer la transition optique de 1,2 eV observée en photoluminescence, nous suspectons donc la présence d'autres états de défaut à 0,2 eV en dessous du minimum de la bande de conduction (voir fig. 5). L'étude de ces états proches de la bande de conduction par photoémission inverse ainsi que des études de la guérison des défauts par traitement thermique sont de perspectives de cette étude.

Cellules solaires de pérovskite hybrides

Les pérovskites hybrides organiques-inorganiques ont attiré une attention considérable en tant que couche active pour les cellules solaires en raison de leur forte absorption de la lumière ainsi que du procédé de fabrication à faible coût [3, 4, 5]. La pérovskite iodure de plomb méthylammonium ($CH_3NH_3PbI_3$, $MAPbI_3$, ou MAPI) a notamment atteint un rendement supérieur à 22% [6]. En plus de cela, les pérovskites hybrides présentent une mobilité des porteurs de charge très élevée et des longueurs de diffusion des porteurs supérieures à 1 μm [7, 8]. En raison de ces propriétés uniques, une fois que le matériau devienne stable, ils pourraient devenir compétitives vis-à-vis des cellules solaires à base de silicium.

Certains détails experimentales de la structure de bande de ces pérovskites n'etant pas connus, j'ai donc appliqué toute une batterie de techniques complementaires pour comprendre ces systèmes. J'ai notamment étudié la structure atomique, les défauts, la structure électronique

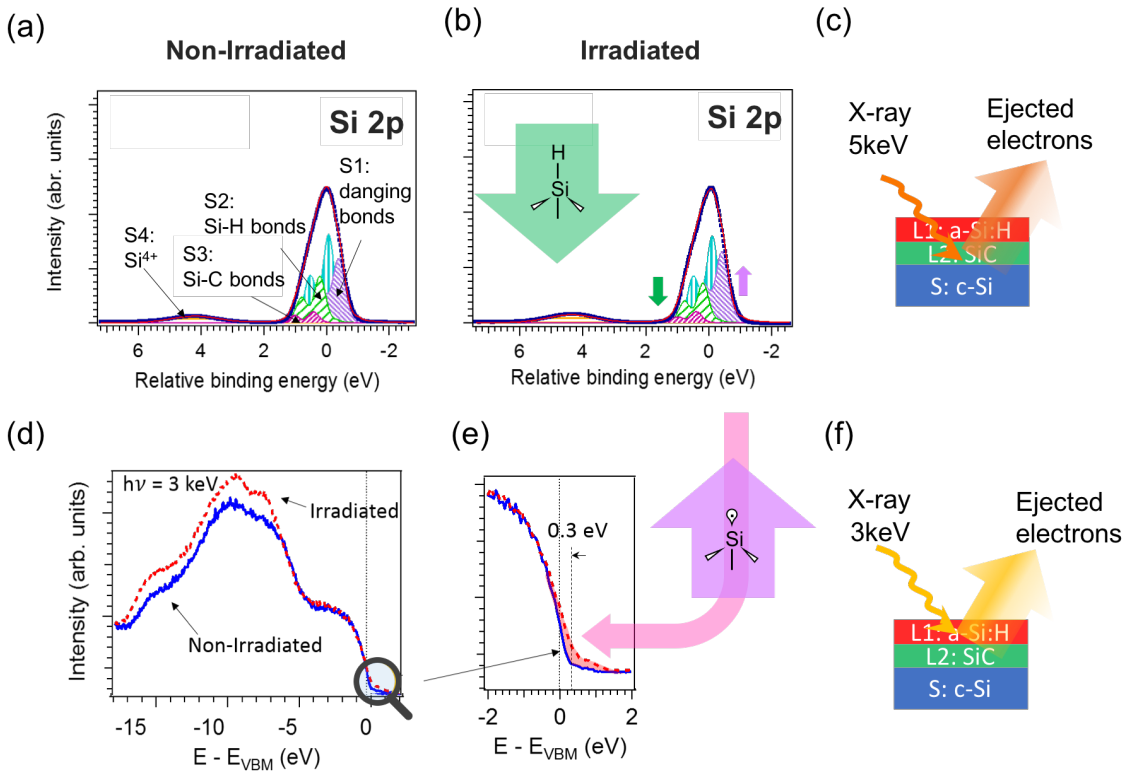

Figure 4: (a) Décomposition du niveau de coeur Si 2p pour les hétérostructures non irradiées et (b) irradiées. Mesures effectuée à une énergie de photon de 3 keV (c). Cinq composants sont nécessaires: La composante du volume associée au c-Si (B), une composante associée aux liaisons pendantes (S1), une composante associée aux atomes de Si liès à un H (S2), une composante associée aux atomes de Si liès au C (S3) et une composante associée au SiO_2 (S4). (d) Comparaison de la DOS expérimentale de hétérostructures irradiées (courbe rouge) et non irradiées (courbe bleue) dans des (f) d'hétérojonctions de 10 nm de a-Si: H mesurées à une énergie de photon de 5 keV. (e) Zoom proche du maximum de la bande de valence (VBM). Les états de défaut, situés à 0,3 eV au-dessus du VBM, sont indiqués en rose.

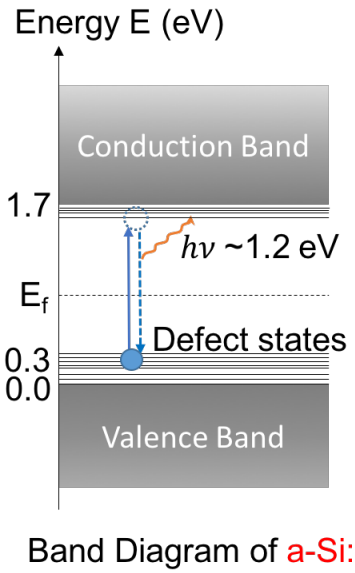

Figure 5: Diagramme des états électroniques dans le a-Si:H qui explique les expériences de photoluminescence.

et la dynamique électronique par diffraction des rayons X, spectroscopie de photoémission résolue en angle (ARPES), spectroscopie de photoémission inverse (IPES), et photoémission à deux photons résolue en temps (2PPE), ainsi que des simulations de photoémission réalisées avec le code SPR-KKR. J'ai étudié deux matériaux: MAPI, une pérovskite de structure tridimensionnel, avec un rendement photovoltaïque élevé et PEPI, une pérovskite de structure bidimensionnel, structurellement plus stable que MAPI.

Pérovskite bidimensionnelle (PEPI)

Les perovskites hybrides bidimensionnelles (2D), traditionnellement utilisées pour les dispositifs optoélectroniques [9, 10, 11], ont récemment attiré l'attention pour les cellules solaires en raison de leur meilleure photo-stabilité par rapport aux perovskites 3D [12]. PEPI est la pérovskite hybride prototypique à deux dimensions.

Dans cette étude, nous nous avons intéressé au phényléthylammonium plomb iodé (PEPI, $(C_6H_5C_2H_4NH_3)_2PbI_4$). Nous avons étudié les bandes de valence et de conduction de PEPI théoriquement. Afin de mesurer toute la structure électronique, la photoémission (PES) et la photoémission inverse (IPES) ont été utilisées (voir fig. 6). Nous avons aussi réussi à déterminer expérimentalement les bandes de valence et de conduction. Cette détermination a nécessité une étude préliminaire pour mesurer les échantillons sous ultravide, tel que requis pour les spectroscopies d'électrons. En outre, nous avons également comparé les bandes expérimentales à nos simulations de la fonction spectrale. L'accord global est satisfaisant.

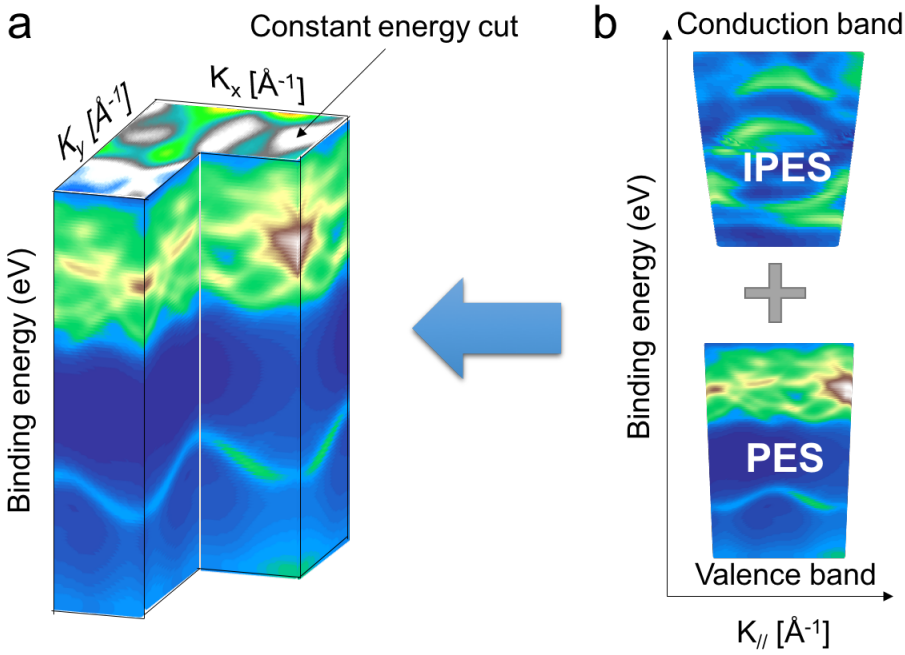

Figure 6: (a) Schéma de la structure de bande simulée pour la comparaison avec nos résultats expérimentaux. Les coupes verticales fournissent la dispersion en function de $k_{||}$. Les coupes horizontales fournissent des coupes d'énergie constantes. b) La photoémission inverse (IPES) et la photoémission (PES) permettent d'obtenir les bandes de conduction et de valence respectivement.

Les caractéristiques spectrales principales dans une coupe d'énergie constante de la structure électronique à travers le maximum de bande de valence sont reproduites par notre simulation. L'asymétrie de l'intensité du poids spectral en fonction de l'angle a également été observée. Des dispersions expérimentales plus plates de la bande de valence ont été observées et comparées à celles théoriques, indiquant des masses effectives plus élevées dans le système réel. De plus, nous avons observé le couplage spin-orbite dans la bande de conduction, là où il est plus évidente (voir fig. 7). Les bandes expérimentales sont en accord avec nos calculs.

Pérovskite tridimensionnelle (MAPI)

Dans la perovskite tridimensionnelle MAPI, nous avons étudié ses états électroniques et leur dynamique de relaxation, et correlé ces deux aspects à la structure atomique. Comme pour PEPI, nous avons effectué les premières mesures résolues en k de la structure électronique sur des monocristaux [13]. Des signatures spectrales très larges dans les bandes expérimentales sont évidentes. Cette largeure relaxe les conditions de transition optique et devrait avoir un impact sur l'absorption optique et sur l'efficacité des cellules solaires. Par ailleurs, nos mesures ont été reproduites avec nos simulations de la photoémission. Nous reproduisons de

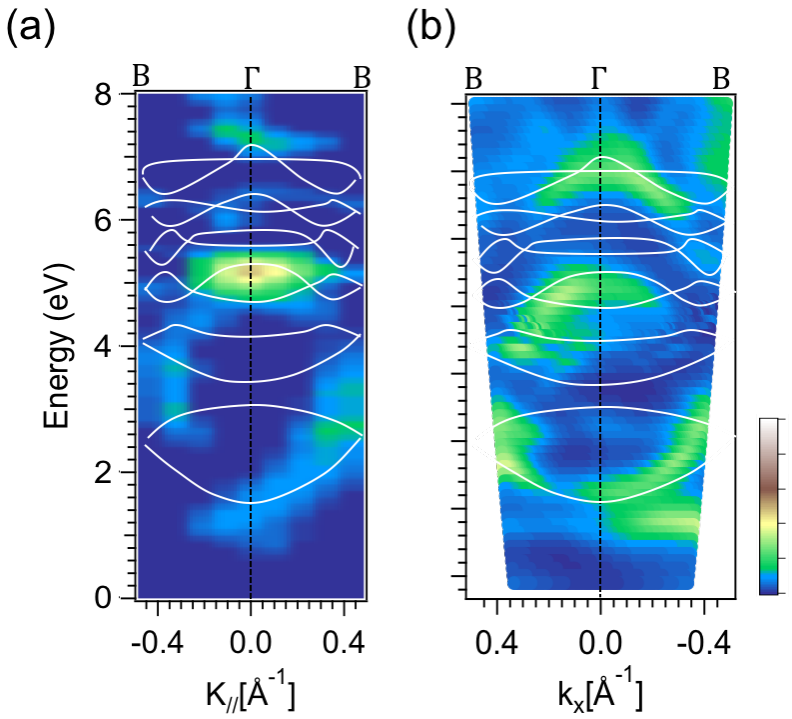

Figure 7: Bande de conduction de PEPI le long de ΓBΓ. (a) Données de photoémission inverse avec les bandes calculées superposées. (b) Spectres IPES simulés avec une structure sans molécules organiques.

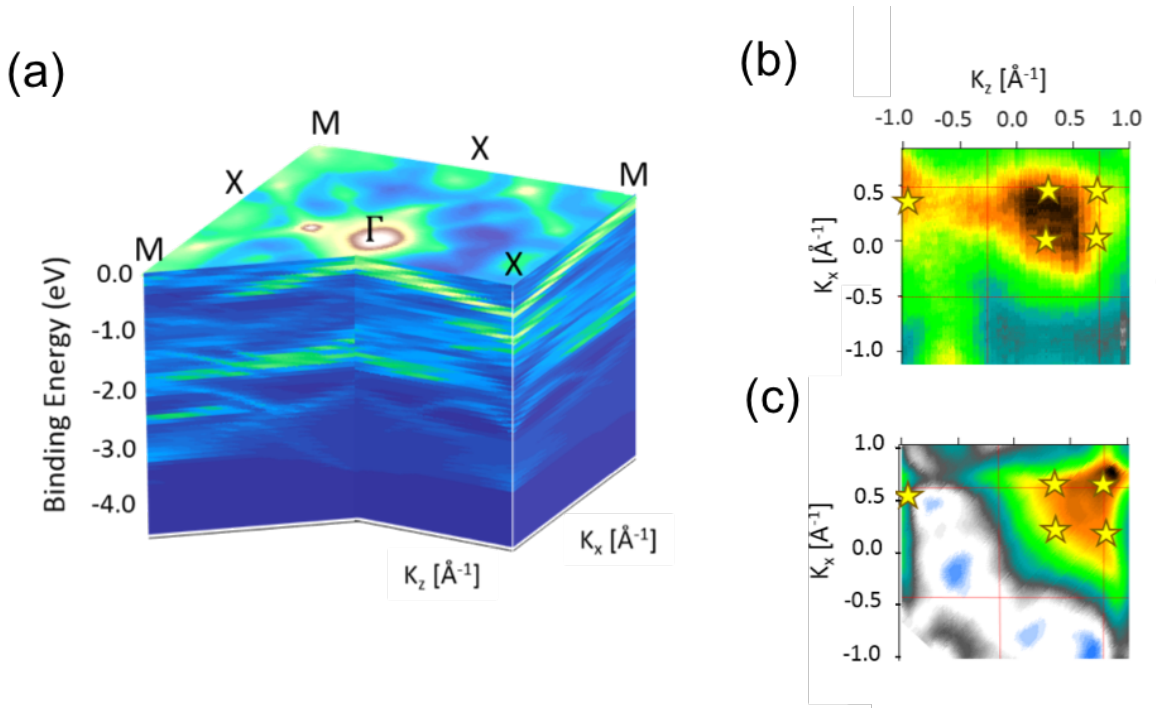

Figure 8: Coupes d'énergie constante de la structure électronique de MAPI. (a) Esquisse des principales bandes attendues dans le plan MXM. (b) Coupe dans le plan ΓXM à 300 meV en dessous du maximum de la bande de valence. (c) Coupe d'énergie constante calculée à 500 meV en dessous du maximum de la bande de valence. Les zones de Brillouin cubiques sont représentées par des carrés rouges. Les étoiles sont une aide pour la comparaison entre théorie et expérience.

manière satisfaisante les différentes coupes d'énergie constante de la structure de bande (voir fig. 8). Les dispersions de bande sont également reproduites qualitativement. Tant dans les expériences que dans les calculs, nous voyons que le poids spectral suit une périodicité cubique alors que le système est structurellement dans la phase tétragonale, comme observé par diffraction de rayons X. Cette contradiction apparente dans les périodicités observées peut s'expliquer par la largeure des bandes, qui cache le repliement de la bande dû à la distorsion tétragonale. Nous avons aussi déterminé la masse effective m^* de la bande d'energie de liaison plus faible, qui est de 0,21 m_e.

Quant à leur dynamique de relaxation, nous avons mesuré la relaxation des électrons photoexcités (voir fig. 9). À une échelle de temps de la subpicoseconde, la thermalisation des porteurs photoexcités se fait par le couplage avec les vibrations des cations organiques. À des échelles de temps plus longues (des centaines de picosecondes), la diffusion électronique contrôle la dynamique. Nous avons également étudié la dynamique en fonction de la densité de défauts. En recuisant les échantillons à différentes températures, un processus qui peut simuler des cellules solaires ageés, nous introduisons des défauts. Ces défauts constituent des

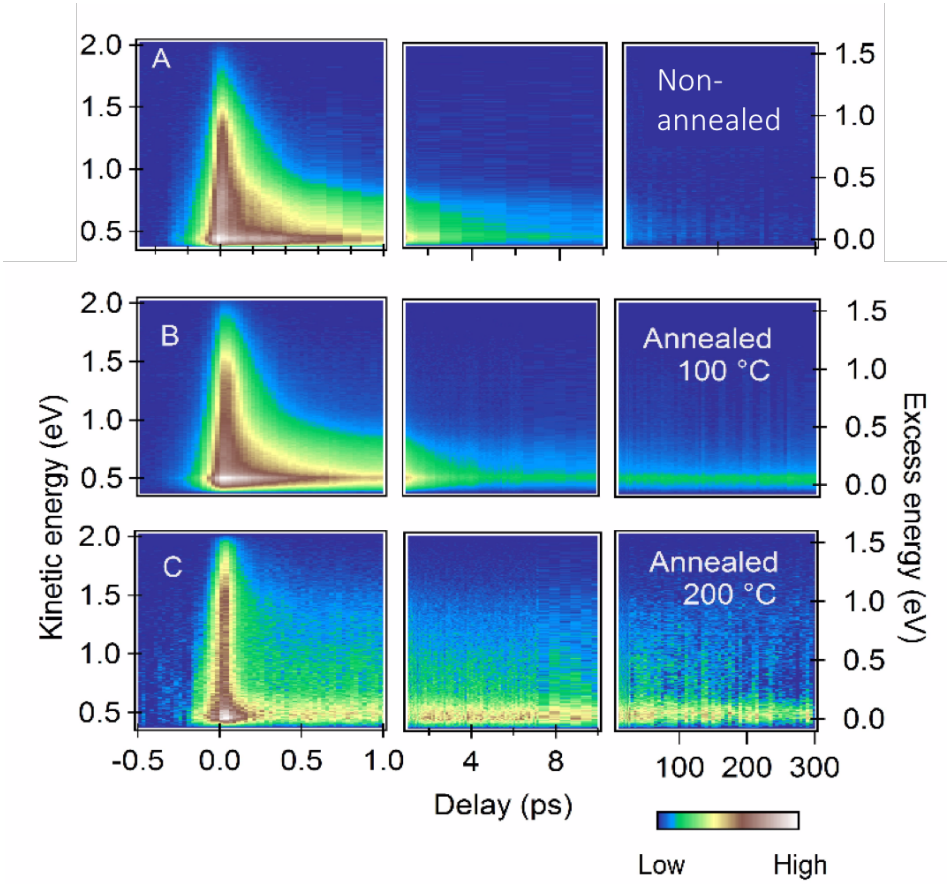

Figure 9: Carte d'intensité de photoélectrons en fonction de l'énergie cinétique et du retard de la pompe-sonde de (a) un échantillon non recuit et des échantillons recuits à (b) 100°C et (c) 200°C.

piéges qui localisent les èlectrons pendant plus de 300 picosecondes (voir fig. 9(b) et (c)) [14].

Les perspectives pour cette partie sont trois. La première perspective est de déterminer expérimentalement la bande de conduction de MAPI par photoémission inverse comme nous l'avons fait pour PEPI. Une deuxième perspective consiste à déterminer la nature, la densité et la mobilité des porteurs de charge. Nous avons commencé à faire des mesures préliminaires d'effet Hall avec cet objectif. Établir de bons contacts et mesurer ces échantillons hautement résistifs sont des défis à surmonter. Une troisième perspective consiste à corréler la dynamique de relaxation électronique avec la dynamique structurelle. En particulier, la structure de bande électronique est modifiée par l'orientation des cations. Pour corréler les propriétés électroniques et la structure, nous avons effectué des expériences préliminaires de diffraction des rayons X résolues en temps pour voir comment le cation organique se réoriente après l'excitation optique.

Conclusions

En conclusion, nos expériences de spectroscopies liées à la photoémission nous ont permis de saisir les propriétés fondamentales électroniques et atomiques de différents types de matériaux photovoltaïques. Les résultats de cette thèse pourraient aider à comprendre les défauts dans les matériaux photovoltaïques et améliorer ainsi l'efficacité des cellules solaires.

Contents

Part I

Generalities

Chapter 1

Introduction

1.1 Towards higher photovoltaics efficiency

Photovoltaics represents the conversion of the solar energy (photons) into electricity (voltage and current). As the energy irradiated by the sun in a minute is enough to power the energy needs of Earth for a year, photovoltaics (PV) is one of the potential solutions to replace fossil energies. However, PV is not yet the principal power supply of energy production in our daily life, though it has already been developed for more than 70 years. The reasons are simple. Up to now, most of the commercially available PV technologies had high costs, and high energy consumption for their production. Power conversion efficiency, which affects directly the overall cost in a PV installation, is thus a critical parameter for the PV generalization.

In 1961, Shockley and Queisser pointed out that the highest efficiency of a PV device, with an optimum semiconductor band gap of 1.34 eV, is around 33.7%. This limit is called nowadays the detailed balance limit or the Shockley Queisser (SQ) limit [15]. This limit is obtained when one photon creates one exciton on a single junction. The efficiency is limited because part of the energy is not absorbed (19%) and some energy is lost (Fig. 1.1). Thermal relaxation spends about 33% of the impinging energy, while about 15% of the solar energy is lost for extracting the carriers. The major energy loss occurs from the photons that have energies greater than the semiconductor band gap. The excess in energy is dissipated as heat through electron-phonon coupling and subsequent phonon relaxation.

To understand the performance of different technologies, it is necessary to compare their efficiency. Fig. 1.2 shows the theoretical SQ limit for the different technologies (crystalline silicon, thin film solar cells, perovskite solar cells), along with the record efficiencies corresponding to their band gaps [16]. It can be seen that monocrystalline materials, such as c-Si, GaAs, and GaInP, can achieve efficiencies higher than 75% of the SQ limit. All the other technologies can still improve. “How to improve the efficiency” is one of the major question that scientists and engineers are working on.

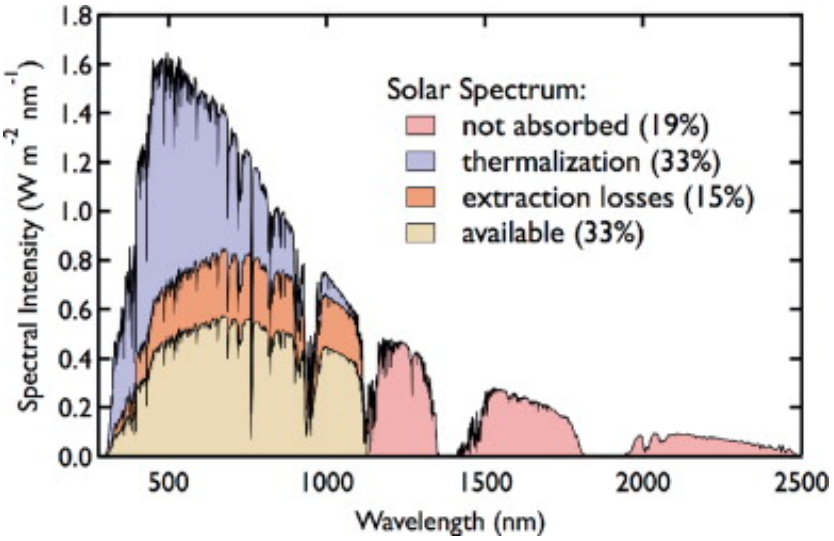

Figure 1.1: Solar spectrum of minimum losses of not absorbed, thermalization, and extraction losses based on SQ limit, representing an upper limit for a single-junction silicon solar cell. [17]

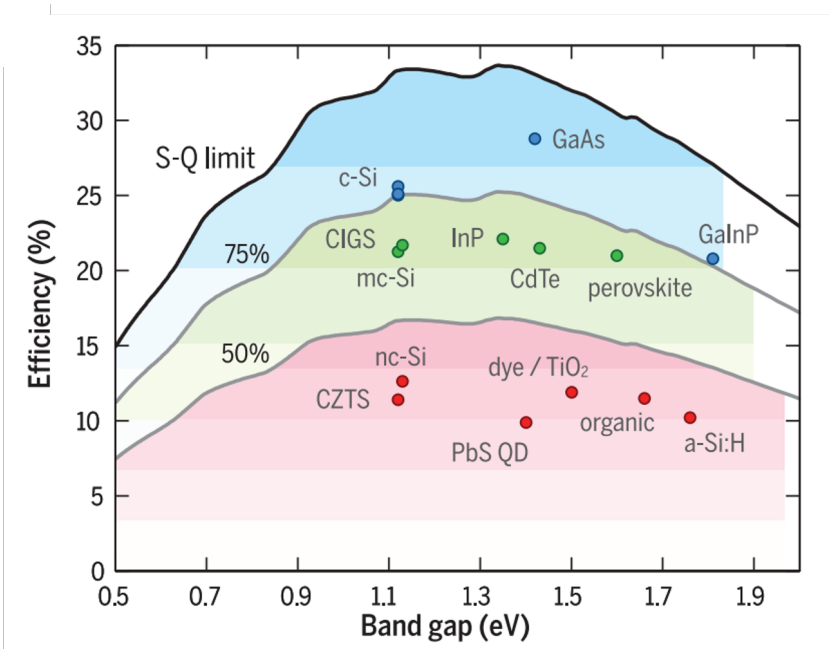

Figure 1.2: The theoretical SQ detailed-balance efficiency limit for different solar cell technologies, along with their record efficiencies. The SQ limit of different technologies depends on the band gap of the absorber material. [16]

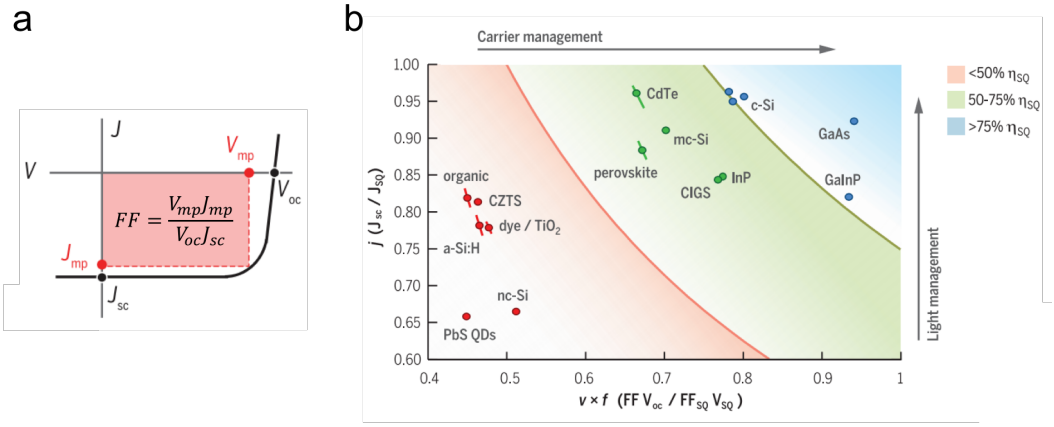

Figure 1.3: (a) A scheme of the current-voltage curve indicated with V_{oc}, J_{sc}, and the maximum-power operation of voltage and current, V_{mp} and J_{mp}. (b) The performance of different PV materials with respect to the limits settled by the SQ limit. "Light management" relates to the capability of light capturing and it is related to the short circuit current J_{sc}, while the "Carrier management" is related to carriers collection, and can be quantified by the product of the fill factor FF and the open circuit voltage V_{oc}. [16]

The energy conservation efficiency η of a solar cell is given by:

$$\eta = \frac{V_{oc}J_{sc}FF}{P_{in}}, \tag{1.1}$$

where the parameters are defined in Fig. 1.3(a): V_{oc} is the open-circuit voltage, J_{sc} is the short-circuit current, FF is the fill factor defined as $V_{mp}J_{mp}/V_{oc}J_{sc}$, (mp: maximum-power operation), and P_{in} is the input power. Eq. 1.1 allows therefore to identify the critical factors for improving the cell efficiency. Every solar cell technology has its own weaknesses and strengths. Fig. 1.3 shows how the different PV materials compare with respect to the SQ limit in terms of light capturing ("light management" in the figure) and how they convert the light into electrical carriers ("carrier management" in the figure). A J_{sc} lower than the SQ limit can result from incomplete light absorption or incomplete carrier-collection. On the other hand, a decrease of the V_{oc} and FF reveals the appearance of undesired carrier recombination, parasitic resistances, or other non-ideal electrical properties.

From Fig. 1.3, it is obvious that most of the PV technologies have a better light absorption than their electronic carrier collection. The carrier collection is affected for instance by the charge carrier transport or the electronic relaxation and trapping. To overcome this shortcoming and to reach the SQ limit, it is necessary to have a better understanding of the fundamental electronic properties of PV materials and interfaces. A straightforward method to understand the electronic relaxation and the recombination is by studying the dynamics of the electrons. The PV operating process is based on the separation of the electron-hole

pairs, which is strongly related to the electronic band structure of the different PV materials. Therefore, before studying electronic dynamics, having a better understanding of the electronic states is essential. In addition, the atomic structure of different PV materials affects strongly the electronic properties as well. A detailed study of the atomic structure will also help to improve the understanding of the electronic properties. Thus, in this thesis, we have studied the atomic structure, electronic states, and the relaxation dynamics of different kinds of PV materials and interfaces.

Among the different kinds of PV materials, we are interested in materials providing high efficiencies at low cost. Fig. 1.4 shows the evolution of the efficiencies of the different technologies as a function of the year. We have selected among all the technologies a settled technology as the silicon heterojunction solar cell (HIT), which has reached the efficiency of 26.6% in 2017 [2] and the emerging technology of hybrid perovskite, which has reached the efficiency of 22.7% in 2017 [18].

1.2 Silicon heterojunction solar cells

Silicon is an abundant material and has a suitable band gap to absorb sun light. Crystalline silicon solar cells have been developed and have dominated the PV market for more than 30 years thanks to their extremely high photo conversion efficiency and high stability. Their main drawback is the high temperature fabrication process at more than 800°C, which may induce the formation of defects and requires energy. In 1992, SANYO (now Panasonic) [20] developed a new technology partly solving these problems, based on silicon heterostructures, that was called "Heterojunction with Intrinsic Thin film (HIT)". These solar cells have reached since 2017 the high efficiency of 26% [2]. Heterojunctions are made by a sandwich-structure of hydrogenated amorphous silicon (a-Si:H), crystalline silicon (c-Si), and a-Si:H again, with an intrinsic thin film at the interfaces between a-Si:H and c-Si. The schematic diagram of a HIT solar cell is shown in Fig. 1.5.

1.2.1 Advantages of amorphous silicon in solar cells

The main advantage of amorphous silicon solar cells with respect cristalline silicon solar cells is a lower fabrication cost. The difference in price arises from the lower fabrication temperature of a-Si:H solar cells (200°C - 300°C), since high temperature is not required there to activate the diffusion of dopants inside the solar cell. Also, a-Si:H solar cells minimize the amount of required Si as they can be thinner (less than 1 μm). a-Si:H not only decrease costs, but also has technical advantages, since the thin films of this material can act as selective contacts, collecting electrons and holes at the different ends of the device to give rise to the photocurrent, as seen in the HIT band diagram in Fig. 1.6. a-Si:H has a larger band gap than c-Si (˜ 1.7 eV

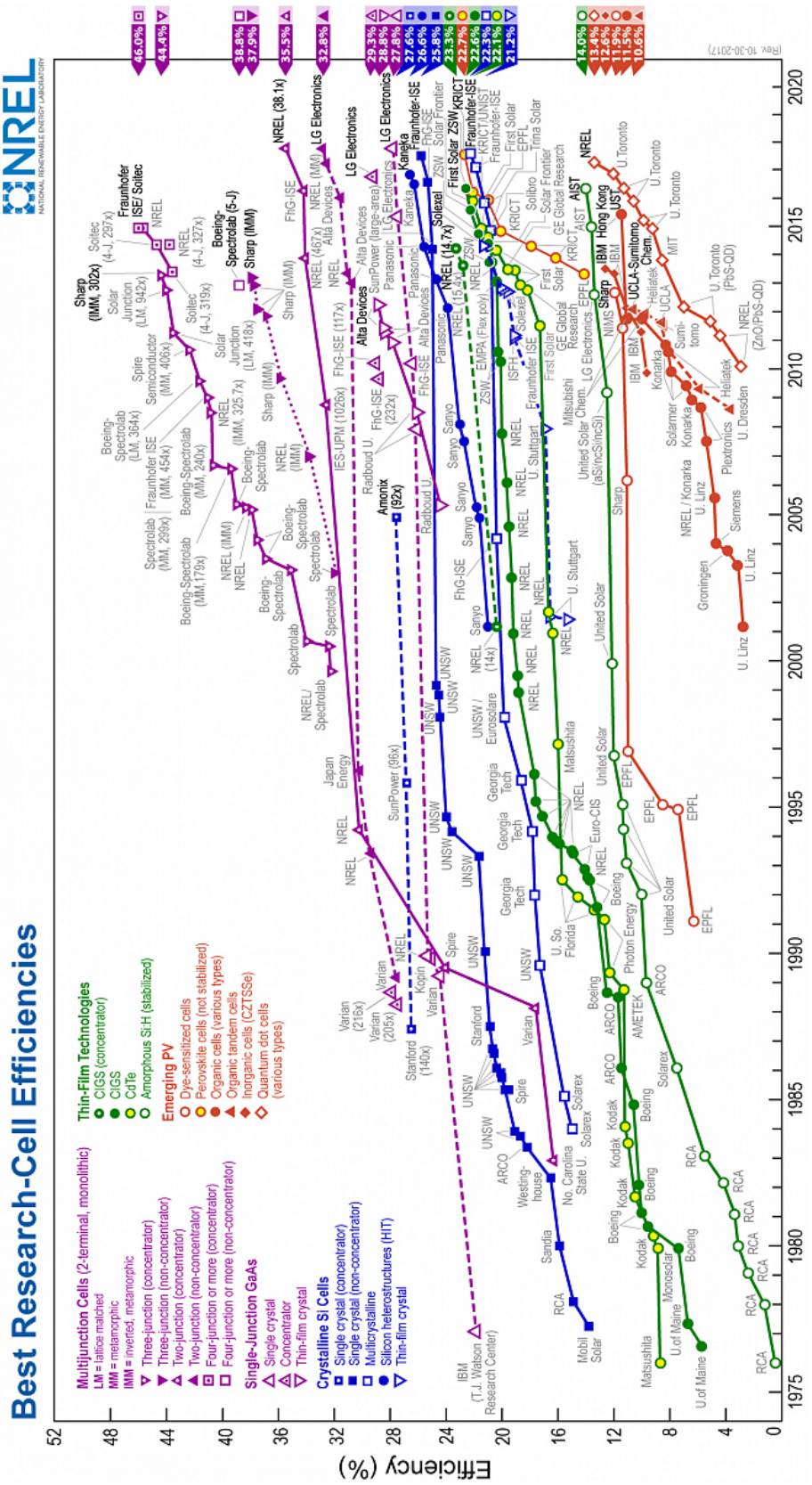

Figure 1.4: Best research-cell efficiency of different PV technologies as a function of year. [19]

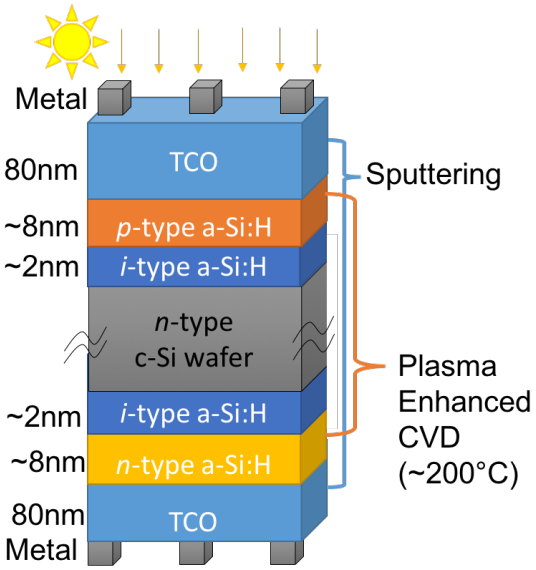

Figure 1.5: A schematic diagram of HIT solar cells. TCO stands for transparent conducting oxide.

and 1.1 eV respectively). Photons below this energy are later absorbed by c-Si if their energy is above 1.1 eV. a-Si:H can also be doped during the thin film growth, both n- or p-type, so it is easy to create hole blocking layers (HBL) and electron blocking layers (EBL) depending on the doping.

Another advantage of a-Si:H is that it can passivate the c-Si surface. Although c-Si has a tetravalent stable structure in the bulk, its surface exhibits dangling bonds that give rise to surface states. These surface states can act as recombination centers for electrons and holes. As recombination reduces the solar cell efficiency, passivation is necessary to suppress these states. In traditional c-Si solar cells, SiO_2, and a-SiN_x:H are the commonly used passivation layer. In the case of HIT cells, an additional passivation layer becomes unnecessary, because a-Si:H can be deposited directly to c-Si and reduce the dangling bonds, their associated surface states and their impact on the charge recombination. The surface recombination velocity (SRV) depends on the number of carriers as a function of the distance to the surface according to:

$$- SRV \cdot \Delta n = - \left[D_n \frac{\delta \Delta n}{\delta x} \right]_{surf}, \tag{1.2}$$

where D is the carrier diffusivity, Δn is the number of carriers, and x is the distance to the surface. If $SRV = 0$, Δn is constant at the surface and at the bulk. If $SRV = \infty$, Δn decreases to 0 at the surface. Therefore, with the surface passivation by a-Si:H, the SRV is reduced from 10^5 - 10^6 cm/s to 10 - 100 cm/s, and often less than 10 cm/s [21]. This extremely

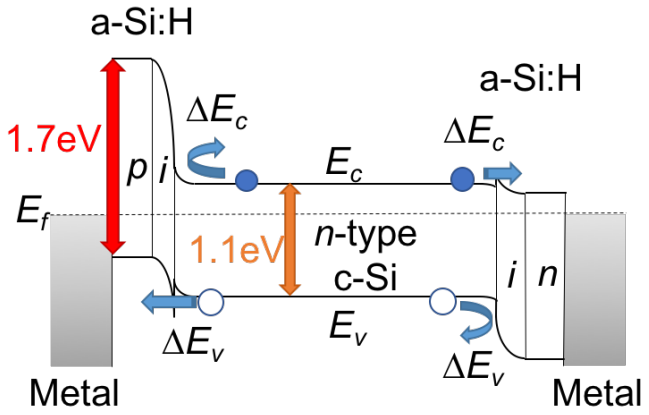

Figure 1.6: Band diagram of HIT solar cells, where E_f is the Fermi level, E_c is the minimum of the conduction band, and E_v is the maximum of the valence band. A larger band offset of a-Si raises the rear-side field and helps diffusing electrons and holes in the solar cells. At the same time, creates a larger barrier for electrons and holes to flow through the rear contact.

low SRV can however only be achieved with intrinsic a-Si:H, because when a-Si:H is doped, the SRV increases. This is the reason why it is necessary to add an additional intrinsic layer in HIT solar cells, which is very thin (˜ 2 nm) in order to let the electrons and holes to tunnel through it (see Fig. 1.6).

The most outstanding and important properties of HIT solar cells are their high efficiency of over 26% in 2017 [2]. Other interesting parameter of HIT solar cells are the open circuit voltage and the low temperature coefficient. HIT solar cells have the highest open circuit voltage V_{oc} (more than 0.7 eV) among the crystalline silicon solar cells thanks to the high passivation of the a-Si/c-Si interface, and according to Eq. 1.1, this is very important for increasing the efficiency in solar cells.

Another unique feature of HIT solar cells is their low temperature coefficient, which means that their efficiency does not drop significantly when the operation temperature increases. The reason for the efficiency decrease when operating at high temperature is related to the diode saturation current density J_0 [22]:

$$J_0 = AT^{\gamma} exp\left(-\frac{E_g}{KT}\right), \tag{1.3}$$

where A is a temperature independent factor, E_g is the band gap, and γ induces the temperature dependences of several parameters determining the recombination current. The recombination current J_0 thus increases when the temperature increases and the current density J in the solar cell becomes:

$$J \approx J_{sc} - J_0 exp\left(\frac{qV}{nkT}\right), \tag{1.4}$$

where J_{sc} is the short circuit current density, and V is the voltage. Thus, the open circuit voltage V_{oc} can be defined as:

By assuming that $J = 0$ at the open circuit voltage $V_{oc} = \frac{nKT}{q} \ln \frac{J_{sc}}{J_0}$ and by differentiating Eq. 1.4 with T, the temperature dependency of V_{oc} is found to be:

$$\frac{dV_{oc}}{dT} = -\frac{\left[\left(\frac{E_g}{q} - V_{oc}\right) + \gamma\frac{KT}{q}\right]}{T}, \tag{1.5}$$

which means that when the operating temperature increases, V_{oc} decreases, and the efficiency η drops. The above equation also shows that for high V_{oc}, close to the energy gap, the temperature dependency is smaller. This is precisely the case for HIT solar cells, that have a higher V_{oc} than traditional crystalline silicon solar cells, so the efficiency in HIT solar cells reduces less than in standard P-N junctions when the operating temperature increases.

1.2.2 Defect states in solar cells

The high efficiency in HIT solar cells strongly depends on the passivation of the dangling bonds by hydrogen. The passivation controls precisely the high open circuit voltage and the low temperature coefficient. An incomplete passivation of the dangling bonds leads therefore to defects that reduce the efficiency. During the deposition process of a-Si:H in the solar cell by plasma enhanced CVD, many silicon bonds can be broken and give rise to dangling bonds (Fig. 1.7).

The dangling bonds originate additional electronic defects in the band gap, which affect the efficiency because they introduce electronic states in the band gap (Fig 1.7). There are two kinds of defect states: mid-gap and bandtail states. Mid-gap states arise from dangling bonds and act as highly efficient recombination centers, so they reduce the efficiency. Dangling bonds, i.e. non passivated ones, are responsible for mid-gap defect states indicated by D_0 in Fig. 1.8. When the electron is missing in the dangling bond, the net charge of the silicon atom is positive, and the electronic state is denoted by D^+. If there is a second electron in the dangling bond, the atom is negatively charged, and the state is denoted by D^-. Dangling bonds are therefore amphoteric, as experimentally observed [24]. The bandtail states (Fig. 1.8) have their structural origin in the disorder of the material, such as an amorphous silicon. These states are less detrimental for the efficiency. They appear as bandtails close to the edges of the conduction and valence bands.

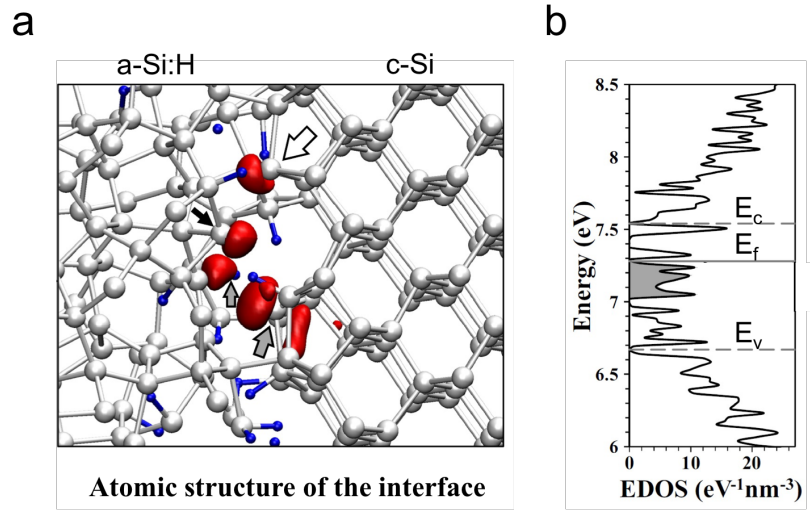

Figure 1.7: (a) aSi/c-Si interface with a non passivated dangling bond. The defect gives rise to an excess of density of states shown in red. (b) Density of states corresponding to the system in (a). The gray states correspond to the defects [23].

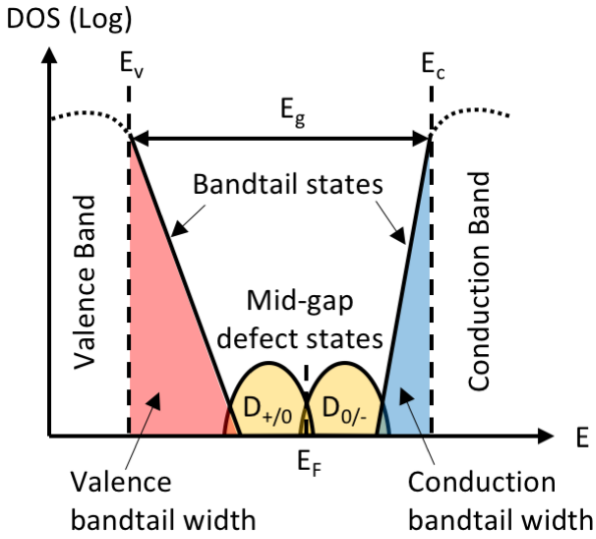

Figure 1.8: Schematic band diagram of hydrogenated amorphous silicon (a-Si:H) in the amphoteric model.

1.3 Hybrid organic-inorganic perovskite solar cells

Hybrid perovskites were first synthesized in 1980 [25]. Many years after, in 2009, they were first used as a light absorbers in a solar cell by the group of Prof. Miyasaka [26]. This early perovskite solar cell had an efficiency of only 4%, but soon the technology evolved and the efficiency rapidly raised. Fig. 1.9 shows the evolution of the perovskite solar cells.

The first perovskite cells were based on the architecture of dye-sensitized solar cells (DSSCs), also called Grätzel cells, that were co-invented by Brian O'Regan and Michael Grätzel [27]. Thanks to their suitable band gap for absorbing sun light [8, 28, 7, 29] and excellent charge transport properties [28, 30], hybrid perovskites replaced successfully the organic dyes of conventional DSSCs (Fig. 1.9(a)). Later on, meso-structures were introduced to increase the absorption area, by means of covering the TiO_2 nanoparticles with hybrid perovskites (Fig. 1.9(b)). Hybrid perovskites were therefore used not only as a light absorber, but also as an electron conductor. The efficiency was remarkable, but the perovskite was unstable because it was dissolved by the liquid iodine electrolyte. After this work, almost simultaneous studies from Grätzel and Park [31], and Miyasaka and Snaith [5] solved this problem by changing the liquid electrolyte by a solid hole transporting material, what is now called a solid-state perovskite solar cell (Fig. 1.9(c)). In this design, hybrid perovskites act as a hole conductor and favor the transport of electrons and holes. Solid-state perovskite solar cells brought the efficiency dramatically from 9.7% [32] to 20.1% [18] within three years. Finally, renouncing TiO_2 nanoparticles, the perovskite solar cells have reached a planar structure (Fig. 1.9(d)), which is more easy to fabricate and brings higher efficiency.

The good physical parameters (such as long carrier diffusion length, high carrier mobility, and high absorption coefficient) of hybrid perovskites are one of the reasons of their success. Another reason is their low cost fabrication. Materials are abundant and cheap and the manufacturing process in solution at low temperature is simple and inexpensive. Large areas can be covered and even it is possible to adopt them to flexible substrates.

1.3.1 Atomic and electronic properties

Perovskite, discovered by Gustav Rose in 1839 and named after Russian mineralogist Lev Perovski, has a specific three dimensional crystal structure $CaTiO_3$ of formula ABX_3, a three-dimensional crystal structure combining two cations and three anions. The structure consists of octahedra of BX_6. The element A is placed in the interstices between the octahedra. In hybrid perovskites, A corresponds to a monovalent organic cation (such as $CH_3NH_3^+$ or $HC(NH_2)_2^+$), B to a divalent cation (such as Pb^{2+} or Sn^{2+}), and X to a monovalent anion from the halide family (such as Cl^-, Br^- or I^-) (Fig. 1.10). A stable three-dimensional structure can be formed by considering the Gold-schmidt tolerance factor, t:

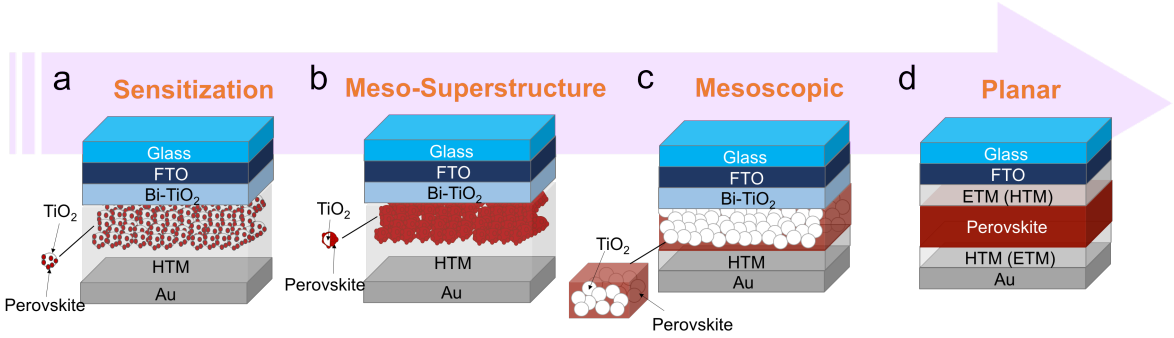

Figure 1.9: Structural evolution of perovskite solar cells from sensitization to meso-superstructure, mesoscopic, and planar structures. HTM stands for the hole transport material and ETM for the electron transport material.

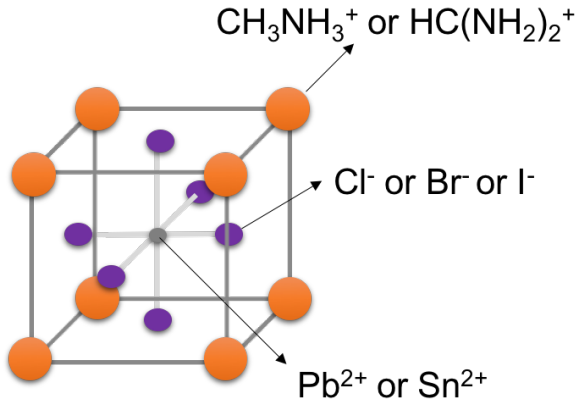

Figure 1.10: Atomic structure of hybrid organic-inorganic perovskites.

$$t = \frac{R_X + R_A}{\sqrt{2}(R_X + R_B)}, \tag{1.6}$$

where R_A, R_B and R_X are the radius of A, B and X ions, respectively. By controlling the value of t, different structures (such as cubic, tetragonal or orthorhombic) can appear [33, 34].

Different ions control the size of the unit cell, and also tune the optoelectrical properties as shown in Fig. 1.11 for $FAPbI_yBr_{3-y}$, where FA is formamidinium ($HC(NH_2)_2^+$). Depending on the composition of the perovskite, the parameter y varies and so does the gap, which changes the color of the hybrid perovskite (the color gets darker with the increasing value of y) and the efficiency of the solar cell. It is therefore particularly relevant to have an accurate understanding of the atomic and electronic structures of the materials in the solar cell.

In hybrid perovskites, the gap can also be controlled through the spin orbit coupling (SOC), because it has a strong effect precisely at the bottom of the conduction band. The

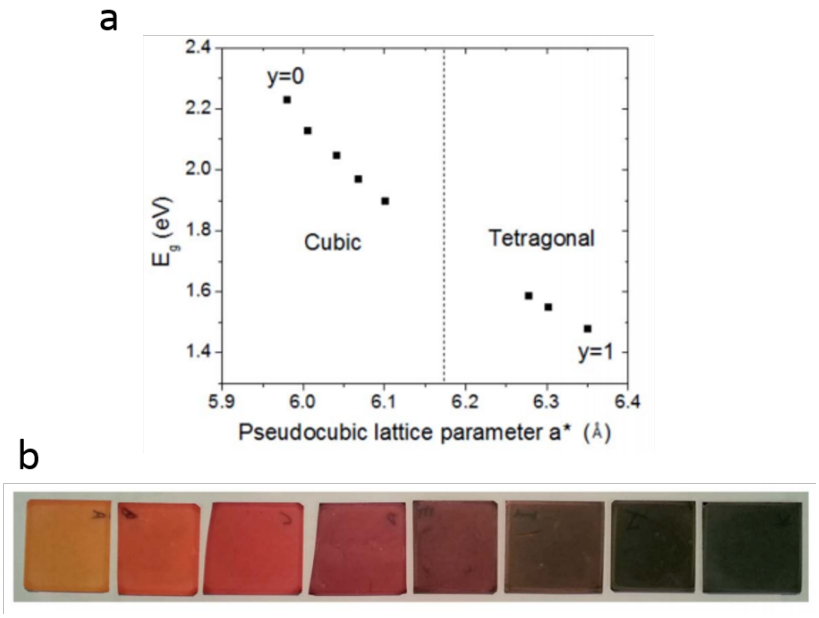

Figure 1.11: Optical band gap of $FAPbI_yBr_{3-y}$ as a function of its lattice parameter. (a) Depending on the y content of iodine in the material, the lattice parameter varies and the band gap changes accordingly. (b) Photographs of different perovskites with increasing y iodine content from left to right [35].

SOC is particularly important in these materials because of the presence of heavy atoms as Pb, which favors a relativistic interaction of the spin of electrons with the atomic potential. With a strong SOC, bands can split and reduce the band gap as shown in Fig. 1.12.

In addition to the gap, there are other parameters of the electronic structure that are important for solar cells. For instance, the effective mass reports on the localization of the charge carriers, i.e. in the intrinsic mobility of charges in the ideal material without defects. Close to the valence band maximum and the conduction band minimum the bands can be approximated by a parabola dispersion. From the second derivative of this parabola, the effective mass can be obtained. Many theoretical calculations have determined the effective mass. However, there are differences in the effective mass that can be as high as a factor of three (Fig. 1.13). An experimental determination of m^* is necessary, and the first step is the experimental determination of the band structure.

Finally, another factor impacting the efficiency of solar cells is the charge carrier generation and its eventual trapping in defects. After illuminating the solar cell, an electron-hole pair is generated and later dissociated to generate the carriers and create the photocurrent (Fig. 1.14). Therefore, to improve the efficiency of perovskite solar cells, the carrier dynamics can help to optimize the solar cell operation and will also be the object of this thesis.

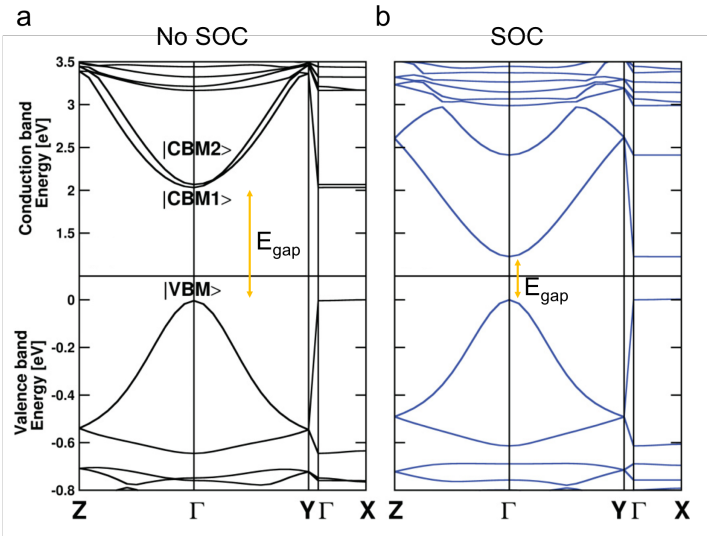

Figure 1.12: The theoretical electronic band structures of 4F-PEPI ($[pFC_6H_5C_2H_4NH_3]_2PbI_4$) (a) without and (b) with spin-orbit coupling (SOC) calculated by DFT [36].

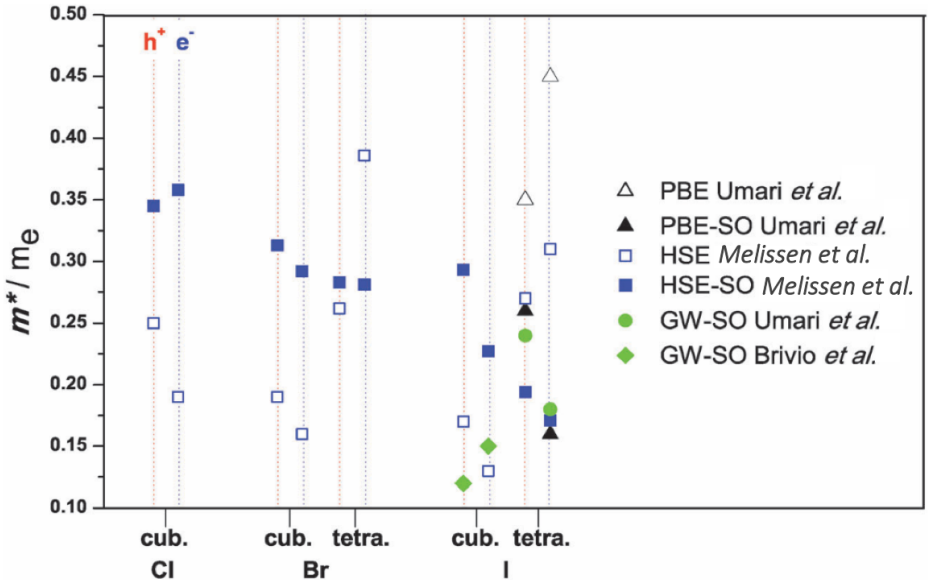

Figure 1.13: Effective masses of electrons and holes in different perovskite materials, namely different methylammonium lead halides (Cl, Br, I), in different crystallographic phases (cubic, tetragonal) and for calculations from different studies [37].

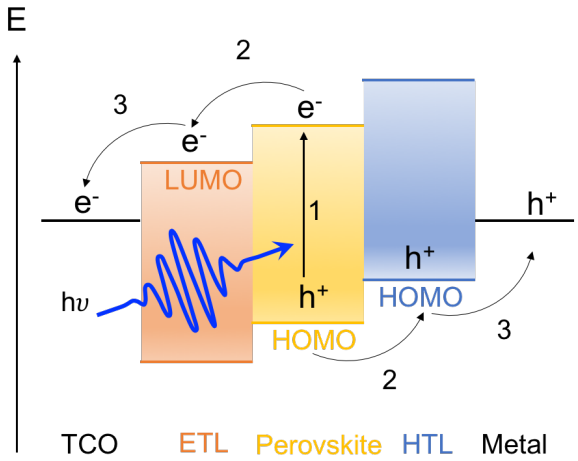

Figure 1.14: Energy levels in a perovskite solar cell and operating schema. During the illumination, the photon energy is absorbed in the perovskite layer and generates electron/hole pairs. The electron/hole pairs are collected by the electron transport layer (ETL) and the hole transport layer (HTL) to create the photocurrent. TCO is the transparent conducting oxide. HOMO is the Highest Occupied Molecular Orbital (or the valence band maximum) and LUMO is the Lowest Unoccupied Molecular Orbital (or the conduction band minimum).

1.3.2 Improvement of the solar cell stability

All the previously mentioned technologies use three dimensional hybrid perovskites, that are less stable than two dimensional ones. The latter are not optimized for photovoltaics because of their large band gap and because the transport perpendicularly to the organic layers is reduced. However, mixtures of 2D/ 3D perovskites in solar cells improve the stability and the transport in 2D can be easily performed along the inorganic layer (Fig. 1.15). Again, a good knowledge of the experimental band structure of 2D perovskites is missing.

1.4 Outline

In this thesis, we have studied two kinds of photovoltaic materials. One is a well stablished solar cell technology, heterojunction (HIT) solar cells, and the other is the emerging perovskite solar cells. In HIT solar cells, we have studied the defects at the interface between a-Si:H and c-Si, which are not completely understood. In hybrid perovskites, we have studied both the electronic structure and its connection to the structure of 2D and 3D materials. We have in particular studied the effective mass, the spin orbit coupling, the electronic relaxation dynamics and its connection to defects.

This manuscript is organized as follows. In chapter 2, experimental and theoretical methods used in this thesis are introduced. In chapter 3, the studies on the electronic properties

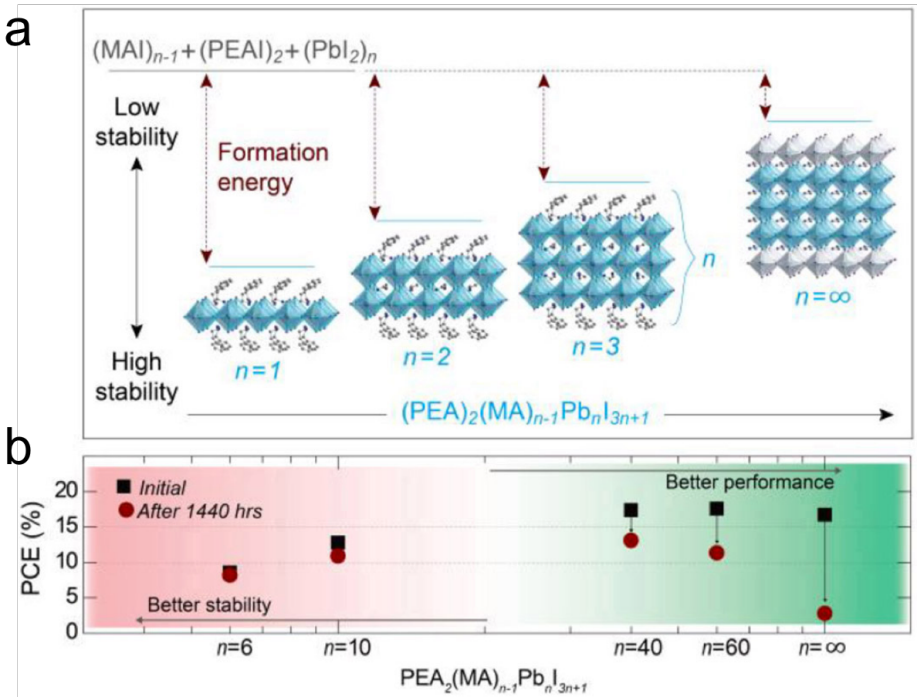

Figure 1.15: Stability and efficiency. (a) Stability of perovskite vs dimensionality. Different unit cells of $(PEA)_2(MA)_{n-1}Pb_nI_{3n+1}$. (b) Device performance and stability evolution of $(PEA)_2(MA)_{n-1}Pb_nI_{3n+1}$. Here, PEA is phenylethylammonium ($C_6H_5C_2H_4NH_3$), and MA is methylammonium (CH_3NH_3) [12].

of defects in amorphous silicon heterostructures will be presented and discussed. In chapter 4, the atomic and the electronic structure of a 2D perovskite, phenylethylammonium lead iodine (PEPI) will be analyzed. In chapter 5, both the atomic and the electronic structure of a 3D perovskite, methylammonium lead iodide (MAPI) will be presented together with the relaxation dynamics. Finally, the conclusions and the perspective of our work will be summarized in chapter 6.

Chapter 2

Experimental and Theoretical methods

The studies that we proposed in the previous chapter can only be performed thanks to high quality samples and appropriate techniques presented in this chapter. In the following sections, we will first introduce the growth method of two families of samples in this studies. Then, the experimental techniques will be separated into three groups, the technique allowing to determine the atomic structures, the techniques to characterize the electronic structures, and the technique to analyze the dynamics of electrons. In addition, a theoretical simulation method for calculating the photoemission band structure will be introduced as well. Thanks to all the techniques and methods, the studies in this thesis could be completed.

2.1 Sample growth

In this thesis, we mainly studied two families of samples. One are the hydrogenated amorphous-silicon (a-Si:H/ c-Si) heterostructures. The other are the hybrid organic/ inorganic perovskites. We will in the following describe how these samples were grown. In section 2.1.1, we will introduce the deposition processes of a-Si:H and the defect implantation method. In section 2.1.2, we will describe the solution growth processes for synthesizing 3-D and 2-D perovskites.

2.1.1 Amorphous-silicon heterostructures

The amorphous-silicon heterostructures we have studied consists of 7 nm of undoped hydrogenated amorphous silicon (a-Si:H) and a thin layer (about 3 nm thick) of hydrogenated amorphous silicon carbon alloy (a-SiC:H) grown on a n-doped (100) mono-crystalline silicon wafer. The thin silicon carbon layer serves as a buffer layer to avoid the epitaxy of the amorphous silicon [38]. The growth is done on both sides of the crystalline wafers. The schematic

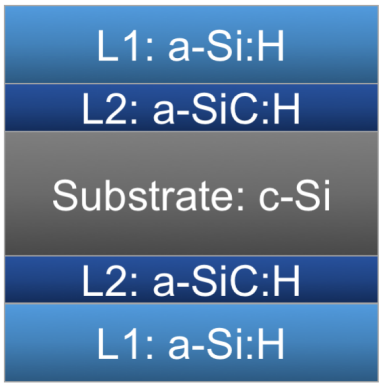

Figure 2.1: Schematic of a-Si:H heterostructure sample.

of one of the sample is shown in Fig. 2.1. These samples were prepared by Alice Defresne of LPICM [39]. More details about the growth procedure can be found below. Moreover, the electronic properties of these heterostructures may be tuned by introducing defects in the structure, that will also be addressed afterwards.

2.1.1.1 As-deposited hydrogenated amorphous-silicon film growth

The a-Si:H and a-SiC:H were deposited by Plasma-Enhanced Chemical Vapor Deposition (PECVD) method at 200 °C in the ARCAM reactor [40] (Fig. 2.2). The reactor uses a radiofrequency to generate a plasma from some precursor gases. One of the great advantages of this technique is that it is possible to deposit films of variable composition thanks to the different available gases. Different species in the plasma react in different ways with the substrate. The charged species bombard the sample surface while the neutral species deposit by diffusion. This technique can be performed over large areas and at low temperatures (˜200 °C), reducing the cost of technological processes.

With this technique, it is therefore possible to deposit a layer of a-SiC:H by mixing silane (SiH_4) and methane (CH_4), and it is also possible to deposit an intrinsic hydrogenated amorphous silicon (a-Si:H) layer using only silane. Doped layers can be achieved by adding trimethylborane, $B(CH_3)_3$, or phosphine, PH_3, respectively for p-type or n-type doping.

In our case, the plasma is obtained by performing electric discharges in the mixture of gas, by applying an radiofrequency voltage between two parallel electrodes. High-energy electrons dissociate or ionize the gaseous precursors through collisions. To initiate the plasma, SiH_4 is introduced into the chamber, and then, an alternating voltage (RF power) is applied between the electrodes. The species resulting from the ionization of the silane are: Si^+, SiH^+, $SiH_2{}^+$ or $SiH_3{}^+$ as well as the same species with negative charges. The species resulting from the

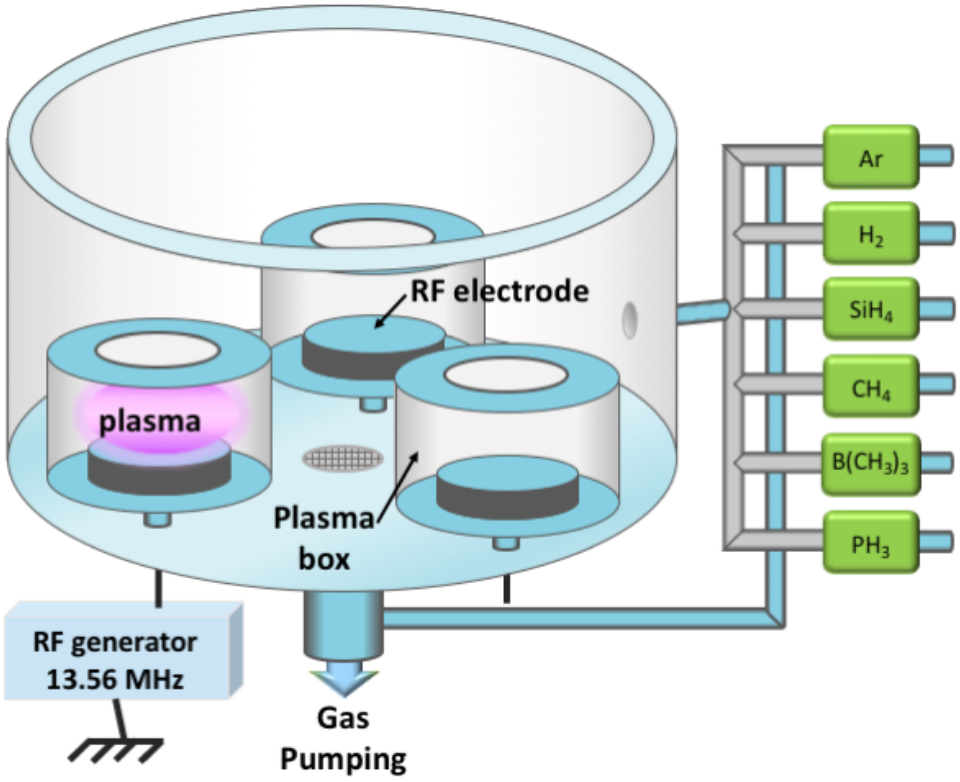

Figure 2.2: Diagram of the ARCAM reactor used for deposition. The distance between the two electrodes is 28 mm. Different available gases on the right-side can be introduced into the reaction chamber. A radiofrequency of 13.56 MHz is applied to sustain the plasma (adapted from [39]).

dissociation are mainly neutral: Si, SiH, SiH_2 or SiH_3 [41].

Before doing the PECVD process previously described, it is necessary to prepare the wafers in an adequate way. The wafers used for the PECVD were supplied by Topsil. Float Zone wafers, doped with phosphorus, that are polished on each side. They are 280 μm thick and have a resistivity between 1 to 5 $\Omega.cm^{-1}$. Before the PECVD process, the mono-crystalline silicon wafer (100) is immersed in a 5% of hydrofluoric acid (HF) bath for 30 seconds to dissolve the native silicon oxide layer present on the surface, then to passivate the dangling bonds on the surface by the hydrogen atoms [42].

After the passivation process, nitrogen gas was used to dry the wafers. The wafers were then directly transferred into the deposition reactor and placed under vacuum. In order to eliminate the molecules of air, water or any other undesirable molecules, acting as impurities in the deposited layer, the initial vacuum before deposition must at least reach 1×10^{-6} mbar. The defect density is minimal when the reactor temperature is constant at 200 ° C.

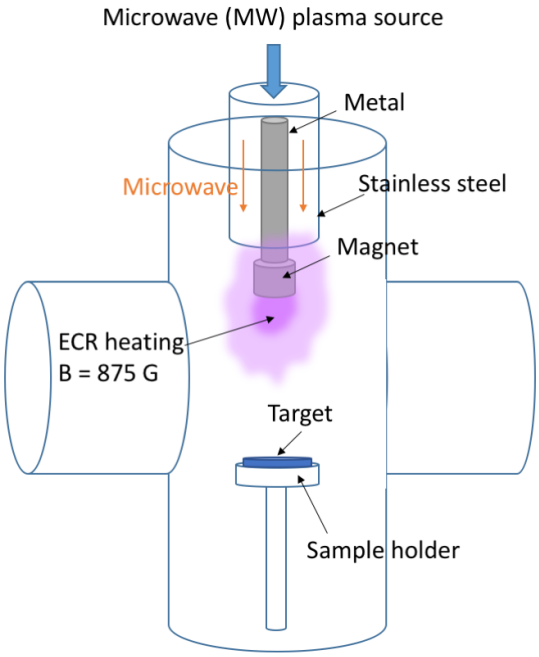

Figure 2.3: Diagram of the plasma reactor used for implantations (adapted from [39]). The plasma is created by a low-pressure microwave discharge. A magnet generates a permanent magnetic field that forces the electrons in the plasma to adopt a helical path in the source area, which increases the probability of collision with the gas atoms.

2.1.1.2 Defect implantation with a plasma reactor

Once the heterostructure was created by PECVD, defects were introduced by implanting Ar atoms with a microwave source plasma reactor. This Electron Cyclotron Resonance (ECR) reactor (Fig. 2.3) is located at the Laboratory of Process and Materials Sciences (Villetaneuse) [43]. The implantations were carried out by Karim Ouaras and in collaboration with Olivier Plantevin (CSNSM).

In this reactor, the plasma is created by a low-pressure microwave discharge according to the principle of ECR. A magnet generates a permanent magnetic field that forces the electrons in the plasma to adopt a helical path in the source area. The path is therefore longer and it increases the probability of collision with the gas atoms. The low pressure allows the plasma to spread throughout the chamber.

One key parameter in the irradiation process is the energy of the incoming beam. The Ar fluence was 10^{15} Ar.cm^{-2}. Its variation allows to control the defect number and its concentration [39]. Fig. 2.4 shows the number of defects with different Ar implantation energies as a function of located depth in the cell, 100 eV in black and 1 keV in red. The number of defects is presented using a logarithmic scale to better appreciate the penetration

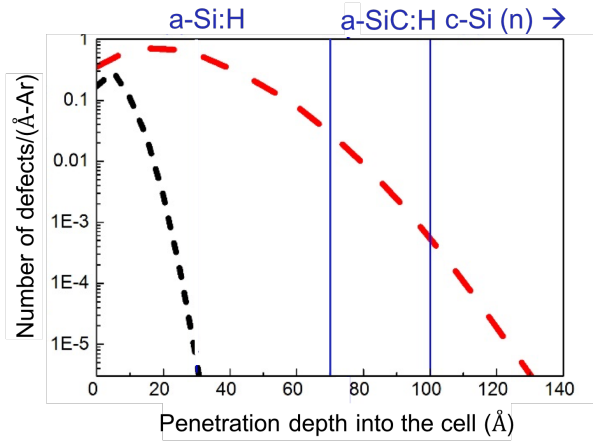

Figure 2.4: Density of defects as a function of depth for different Ar implantation energies. The black curve corresponds to a 100 eV beam and red to a 1 keV beam. The inset figure shows a log scale of the original one to better present the penetration depth. [39]

depth. It is shown that Ar^+ beam with an energy of 100 eV allows to generate defects up to a depth of 3 nm. The 1 keV beam allows to create defects down to 13 nm depth. In view of the previous results, an Ar^+ beam of 1 keV was used to create defects (about 10 at.% with the mean projected range of 3.5 nm for the argon ions) in the 10 nm thick heterostructure.

2.1.2 Hybrid perovskites

We have studied both the 3D perovskite MAPI, and the 2D perovskite PEPI. These hybrid perovskite single crystals were prepared with the low-temperature solution growth method in a two-step process. In the first step, the organic and inorganic precursors were prepared and diluted in γ-butyrolactone (GBL) as a solvent. In the second step, during the solvent evaporation, the precursors self-assembled into hybrid perovskites. Depending on the stoichiometry of the precursors and the nature of the organic moiety, different dimensionalities (3D, 2D...) of self-assemblies appear. The group of Emmanuelle Deleporte in Laboratoire Aimé Cotton (LAC) provided us the hybrid perovskites for our studies. Most of the samples were grown by Ferdinand Lédée and Gaëlle Trippé-Allard. In the following, the growth methods for these two molecules are described.

2.1.2.1 Methylammonium lead iodide growth

Methylammonium lead iodide, $CH_3NH_3PbI_3$ or MAPI, is synthesized from PbI_2 and methylammonium iodide, CH_3NH_3I. The CH_3NH_3I precursor solution is prepared from methylamine. The methylammonium iodide is obtained from a solution of methylamine CH_3NH_2 with a slight excess of hydroiodic acid (HI) placed in an ice bath at ambient atmosphere. The

methylamine is obtained according to the reaction:

$$CH_3NH_2 + HI \rightarrow CH_3NH_3^+I^- . \tag{2.1}$$

In our case, 17.2 ml of HI (57% stabilized) on 15 ml of cold methylamine were poured drop by drop. The mixture is agitated during 2 h. Methanol from the solution is evaporated in a rotary evaporator at 60 °C during 1 h. The aqueous solution is then poured in diethylether to precipitate the methylammonium iodide salt. The precipitation is filtered and washed with diethylether to remove any traces of I_2. The salt is then recrystallized in ethanol. Once the precursor salt is dried after baking at 60 °C overnight, the solution is ready.

In parallel, it is necessary to obtain the PbI_2 precursor solution. PbI_2 crystals are obtained due to the interaction between a $Pb(NO_3)_2$ solution and a KI solution. The mixture contains slightly more $Pb(NO_3)_2$ than KI in average. Crystals were washed several times on a paper filter using distilled water and then dried at T=60 °C in vacuum.

The last step corresponds to the synthesis of $CH_3NH_3PbI_3$ single crystal according to the reaction (2.2):

$$CH_3NH_3I + PbI_2 \rightarrow (CH_3NH_3)PbI_3. \tag{2.2}$$

The solutions of both precursors are mixed in a 1:1 proportion. In particular, a solution of 40% PbI_2 by mass in γ-butyrolactone (GBL) with one equivalent of $CH_3NH_3^+I^-$ is prepared. The solution is stirred at 60 °C for 8 h to dilute PbI_2. Then, the solution obtained is kept at T=150°C in order that the solvent evaporates. Under these conditions, the solution boils. Once the solution is limpid, the solvent is evaporated to self-assemble the hybrid perovskite within few hours, depending on the size of crystal needed. After this step, $CH_3NH_3PbI_3$ crystals are obtained and dried at the same temperature during 30 min. Fig. 2.5 shows an image of the precursor preparation of MAPI crystal assembling ($CH_3NH_3^+I^-$ + PbI_2) and a millimetric size single crystal using the above preparation. After the crystals are synthesized, they are kept in Ar to protect the crystals from the degradation in air before the experiments.

2.1.2.2 Phenylethylammonium lead iodide growth

Phenylethylammonium lead iodide, $(C_6H_5C_2H_4NH_3)_2PbI_4$ or PEPI is synthesized using the adapted Anti-solvent Vapor-assisted Crystallization (AVC) method, which gives good results for 3D perovskites [44], although in this case millimeter-sized crystal growth requires about one week instead of some hours. The so-obtained crystals are of high quality, with a very low traps density ($\tilde{}10^9 cm^{-3}$) [45].

Large single crystals are synthesized from $C_6H_5C_2H_4NH_3I$ (called PEAI here-after). To synthesize PEAI, first of all, 8 mL (0.064 mol) of phenethylamine $C_6H_5C_2H_4NH_2$ (Alfa Aesar,

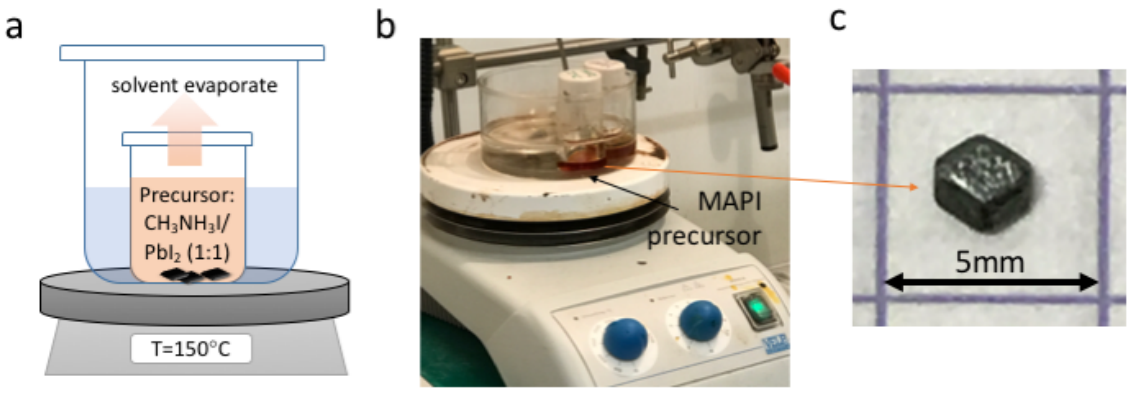

Figure 2.5: (a) Schematic of the MAPI precursor preparation. (b) The precursor preparation of MAPI crystal assembling ($CH_3NH_3^+I^- + PbI_2$). (c) Image of a typical MAPI crystal grown at Laboratoire Aimé Cotton.

99%) are dissolved in 300 mL of dry diethyl ether. Then, 12.6 mL (0.096 mol) of HI (Sigma-Aldrich, 57% in water) are added drop by drop to the solution in an ice bath. The reaction is:

$$C_6H_5C_2H_4NH_2 + HI \rightarrow C_6H_5C_2H_4NH_3^+I^-. \tag{2.3}$$

White crystals of PEAI immediately precipitate. Afterwards, the powder is vacuum-filtered and washed four times with dry diethyl ether. Finally, the PEAI white powder is recrystallized from a mixture of diethyl ether and ethanol and dried in an oven at 60°C overnight.[44]

After preparing the PEAI, PEPI crystals can be synthesized by the AVC method (see Fig. 2.6(a)). First of all, 2.305 g of PbI_2 (5 mmol) and 2.480 g of PEAI (10 mmol) are dissolved in 5 mL of γ-butyrolactone (GBL) (1:2 molar ratio) and stirred at 50°C until it is completely dissolved. Afterwards, the 1 mol/L solution is filtered with a 0.2 µm PTFE syringe filter and poured in a small vial, which is then placed in a bigger Teflon cap vial. Then,10 mL of dichloromethane (DCM) are finally poured in-between the inside of the big vial and the outside of the small vial. By the assistance of the diffused vapor of the DCM, the reaction giving rise to the PEPI crystal is:

$$C_6H_5C_2H_4NH_3^+I^- + PbI_2 \rightarrow (C_6H_5C_2H_4NH_3)_2PbI_4. \tag{2.4}$$

After 48 hours, millimeter-sized rectangle-shaped bright and transparent orange crystals start to grow in the small vial [44]. Fig. 2.6(b) shows a millimetric-sized single crystal of PEPI obtained by the AVC method. After the crystals are synthesized, they are kept in Ar

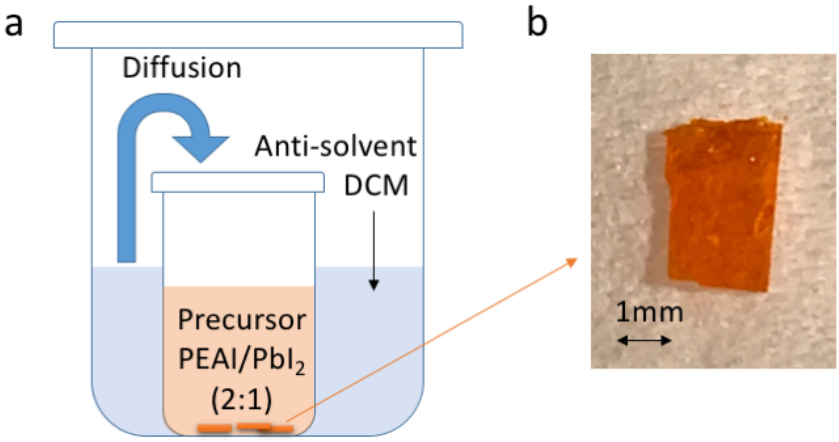

Figure 2.6: (a) Schematic of the AVC process. (b) Image of typical PEPI crystals obtained by AVC method (adapted from [44]).

to protect the crystals from the degradation in air before the experiments.

2.2 Atomic structure by X-ray diffraction

After a growth procedure to produce a known material, it is necessary to determine if the crystal corresponds to the expectations. It is therefore necessary to determine its atomic structure. To determine the atomic structure of a bulk crystal, there exist many different methods. The most straightforward one is X-ray diffraction (XRD). Single-crystal X-ray Diffraction is a non-destructive analytical technique, that provides many detailed information including lattice parameters, bond-lengths, bond-angles, and even the atomic positions of all the atoms in the unit cell.

XRD is based on the constructive interference of monochromatic X-rays scattered by a crystalline sample. Constructive interference between beams scattered in different (hkl) parallel planes appears when the Bragg's Law is satisfied:

$$n\lambda = 2d_{hkl}\sin\theta, \tag{2.5}$$

where λ is the X-rays wavelength, d_{hkl} is the spacing of the (hkl) scattering planes, and θ is the angle between the incoming X-rays and the scattering planes. In this situation, a maximum of the diffracted X-rays appears in the Bragg peaks. By changing the geometry of the incident rays, the crystal, and the detector, many Bragg peaks can be detected. The diffraction or reflection pattern and the crystalline lattice in real space are related by a Fourier transform, so the diffraction patten allows to determine the structure in the real space. The diffraction studies in this thesis were performed at the CRISTAL beamline of SOLEIL synchrotron, in

collaboration with Pierre Fertey.

CRISTAL is a diffraction beamline dedicated to single crystals and powders. The source of the beamline is an U20 undulator, that delivers photons between 4 and 30 keV. The highest possible energies can be reached without losing its brilliance. The desired photon energy is selected with a monochromator with a fixed exit Double Crystal Monochromator (DCM), which consists of one pair of Si(111) crystals for the energies between 4 and 30 keV, and one pair of Si(311) crystals for energies between 8 to 60 keV. Samples are mounted on three kinds of diffractometer, namely a 2-Circle, a 4-Circle, and a 6-Circle diffractometer, that are chosen according to the experiment. For our experiments on single crystals, we used the 4-Circle diffractometer (Fig. 2.7(a)). The oscillation data collection method was used. We measured the diffraction signal while rotating the sample at constant speed over a small angular range (typically 1°) for each image acquisition.

A schematic of a 4-circle diffractometer is represented in Fig. 2.7(b) showing the angles 2θ, χ, ϕ, and Ω, that define the relationship between the crystal lattice, the incident ray and the detector. At the intersection of all these rotation axis and the incoming beam, the sample holder with the sample is placed. We first mount the sample on thin glass fibers attached to brass pins, that are subsequently mounted onto a goniometer head that allows the turning of the X, Y and Z orthogonal directions to center the crystal in the X-ray beam. To prevent burning out the detector, a beam stopper is located at the opposite of the collimator to block the directly transmitted rays. The diffracted beams are detected in all the other directions. Once a complete data set is collected, the reflections were indexed with CrysAlisPro software. Finally, the structures were solved by a direct method strategy using JANA [46] and SHELX packages [47].

2.3 Electronic structure by electron spectroscopies

In this section, the tools used in this thesis for determining the electronic structure are described. Firstly, the two experimental techniques, photoemission (PES) and inverse photoemission spectroscopy (IPES) are introduced. Photoemission allows to determine the valence band dispersion and the core levels. On the other hand, inverse photoemission is used to determine the conduction band dispersion. Secondly, the SPRKKR code which can simulate the experiment data is presented.

2.3.1 Photoemission spectroscopy

Photoelectron spectroscopy is a technique based on the photoelectric effect. This effect was originally observed by Antoine Becquerel in 1839[48] and later explained as a manifestation of the quantum nature of light by Einstein[49]. The effect consists on the emission of electrons

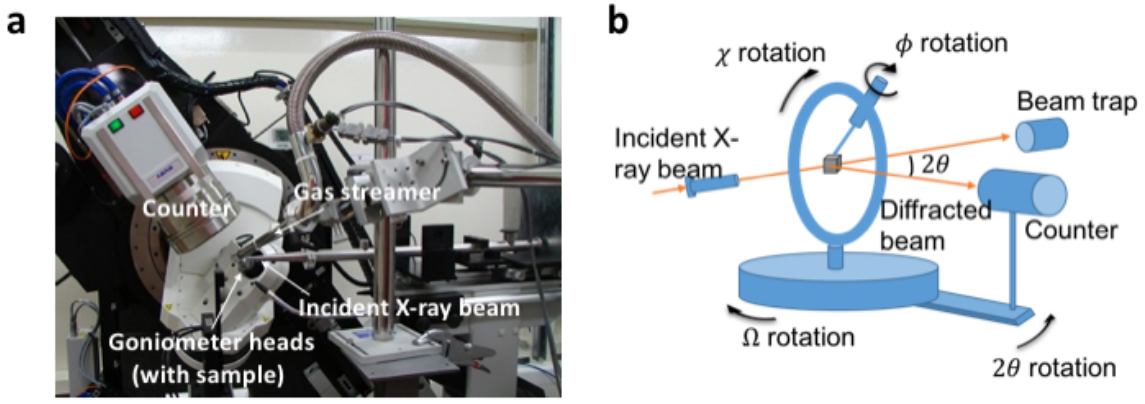

Figure 2.7: (a) Image of the 4-circle diffractometer at CRISTAL beamline. It is equipped with a gas streamer to cool the sample. (b) Schematic of the 4-circle diffractometer indicating, the relevant angles for the measurement: 2θ, χ, ϕ, and Ω, the incident beam, the detector, the sample, and the the beam stopper.

where a material is illuminated with photons of an energy above a certain threshold. The energy is of course conserved in the process:

$$E_k = h\nu + E_B + \phi, \tag{2.6}$$

where $h\nu$ is the light energy, ϕ is the work function of the material, and E_B is the binding energy of electrons inside the material [50].

The experimental working principle of photoemission is shown in Fig. 2.8. By injecting photons, the electrons inside the valence band of the materials can be ejected out. When measuring the kinetic energy and the emission angle of these electrons, we can study the electronic band structure dispersion of the valence band of the material.

Photoemission spectroscopy can measure also the core electrons instead of valence electrons. By measuring the kinetic energy of these excited core electrons, the binding energy of these core electrons, i.e. core levels, can be estimated. The working principle of core level measurement is shown in Fig. 2.9(a). Due to the bonding with the nucleus, the core electrons also play roles in chemical bonding and reactions. By measuring the shift of binding energies of these core levels, we can obtain the information of the chemical shifts of different atomic bondings. A classical example of chemical shifts of Si 2p core levels measured on an ultra-thin SiO_2/Si(100) layers is shown in Fig. 2.9(b) [52]. From the spectra, the core levels shift towards higher binding energy with the positive charge on the Si ion.

After having general concepts of photoemission spectroscopy, we are going to introduce more specific features of different photoemission spectroscopies in the following subsections.

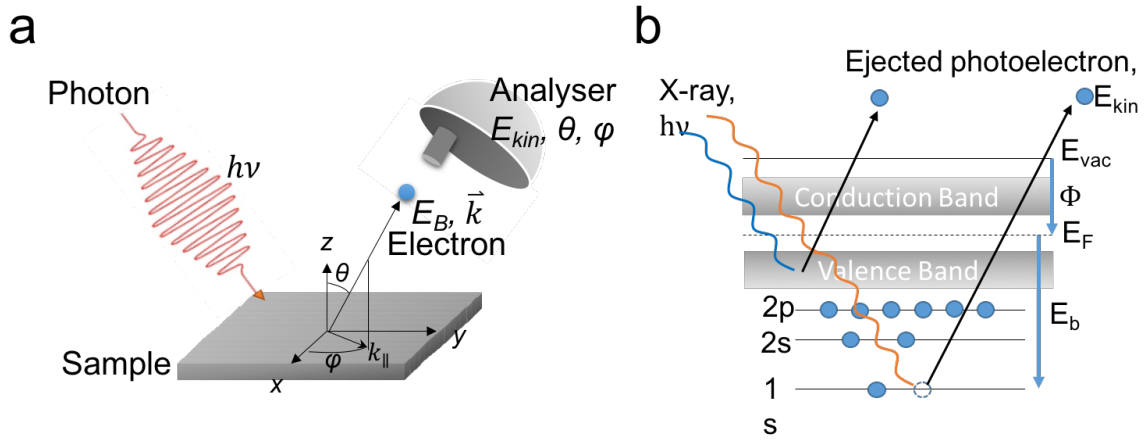

Figure 2.8: (a) Schematic of ARPES. (b) The working principle of valence band and core level measurement. Photoemission process presents with the Fermi level E_F , the vacuum level E_{vac}, the work function of sample Φ, the kinetic energy of photoelectron E_{kin}, and the binding energy in material E_B . When injecting a higher photon energy, the electrons from the core levels can be ejected. By measuring the kinetic energy of these electrons, we can study the core level of the materials in deeper layer. (adapted from [51]).

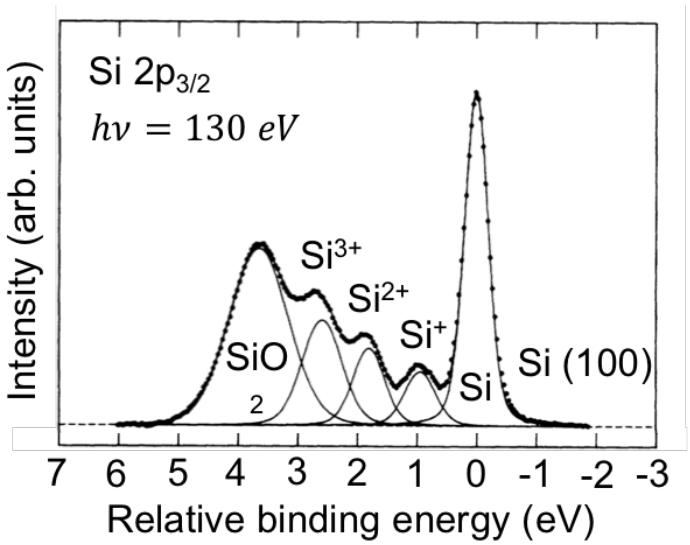

Figure 2.9: The chemical shift from core-level spectra of ultrathin SiO_2 overlayers on Si(100) surfaces [52].

2.3.1.1 Angle resolved photoemission spectroscopy

Equation (2.6) has important consequences. If the kinetic energy of the ejected electrons is measured and knowing the frequency of the incoming photons and the work function of the material, electronic states can be studied. In particular, Kai Siegbahn developed the X-ray Photoelectron Spectroscopy (XPS) to study the core levels and identify different chemical environments [53]. The Ultraviolet Photoelectron Spectroscopy (UPS) appeared later on to study the electronic states involved in the chemical binding (valence band) by David W. Turner [54]. The electronic states of the valence band have a binding energy that changes as a function of the direction and the wave vector $\overrightarrow{k}$. It is therefore necessary to determine the binding energy and the wave vector to fully understand the valence band. We have already seen that E_B can be obtained from E_k (eq. 2.6). In addition, due to the parallel wave vector conservation when the electron crosses the surface, the wave vector can also be determined as:

$$\left|\boldsymbol{k}_{||}\right| = \left|\boldsymbol{K}_{||}\right| = \frac{|P|}{\hbar}\sin\theta = \frac{\sqrt{2mE_k}}{\hbar}\sin\theta, \tag{2.7}$$

where $k_{||}$ is the parallel wave vector in the material, $K_{||}$ is the parallel wave vector in vacuum, P is the linear momentum in vacuum, $\hbar$ is the reduced Planck constant, E_k is the kinetic energy, and with the two different components, k_x and k_y defined as:

$$k_x = \frac{\sqrt{2mE_k}}{\hbar}\sin\theta\cos\varphi, \tag{2.8}$$

and

$$k_y = \frac{\sqrt{2mE_k}}{\hbar}\sin\theta\sin\varphi. \tag{2.9}$$

The perpendicular component of $k_\perp$ is more difficult to determine, since the electrons must overcome an energy barrier to cross the surface, and $k_\perp$ is not conserved, as shown in Fig. 2.10. However, it can be obtained by assuming that the final state E_f of the electron follows a free-electron dispersion (2.10):

$$E_f(k) = \frac{\hbar^2\boldsymbol{k}^2}{2m} - |E_0| = \frac{\hbar^2(\boldsymbol{k}_{||}+\boldsymbol{k}_\perp)^2}{2m} - |E_0|\,, \tag{2.10}$$

where E_0 is the bottom energy level of the valence band. Then, if we insert the expression of $\boldsymbol{k}_{||}$ (2.7) in (2.10), $\boldsymbol{k}_\perp$ can be derived as:

$$|\boldsymbol{k}_\perp| = k_z = \frac{\sqrt{2m(E_k\cos^2\varphi + |E_0| + \Phi)}}{\hbar}. \tag{2.11}$$

This $k_\perp$ determination is particularly relevant when dealing with 3D systems, as it is the

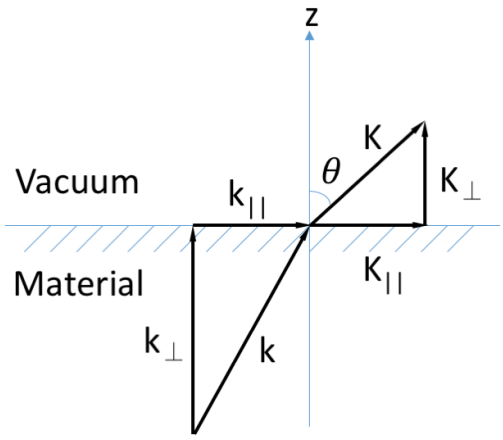

Figure 2.10: Schematic of wave vector conservation when the photoelectron crosses the surface.

case of MAPI because the energy bands depend on $k_\perp$. In PEPI, the band structure does not depend on $k_\perp$ as it is a two dimensional material.

The ARPES experiments presented in this thesis were preformed at CASSIOPEE beamline of SOLEIL synchrotron. CASSIOPEE is a soft X-ray beam line, which is dedicated to high resolution ARPES and spin-resolved photoemission (Fig. 2.11). This beamline has two undulators carry an energy range from 8 too 1500 eV. They are characterized by their high flux and their adjustable polarization, and operated as a source of radiation. Afterwards, to reach the best flux intensity and monochromaticity of the light, the photon energy is further selected by a high-resolution plane grating monochromator together with a variable line spacing and a variable groove depth gratings. After the monochromator, the beamline is divided into two branches to supply the photons for two different end-stations, the high-resolution ARPES end-station and the spin-resolved photoemission end-station. Both end-stations are connected to a molecular beam epitaxy chamber for growing and characterizing the samples. The ARPES end-station is equipped with a Scienta R4000 electron energy analyzer and is equipped with a 4-axis manipulator for the sample.

2.3.1.2 Hard X-ray photoemission spectroscopy

When dealing with buried systems, conventional photoemission does not allow to probe the core levels or the valence band. Conventional photoemission only probes last monolayers of the material, due to the small electron escape depth upon operation with low energy photons. In order to probe the amorphous silicon heterostructure (a-Si:H/ c-Si), we need to use hard X-ray photoemission spectroscopy (HAXPES), the name that describes photoemission performed with high photon energies (of the orders of several keV). In this technique, the analyzed

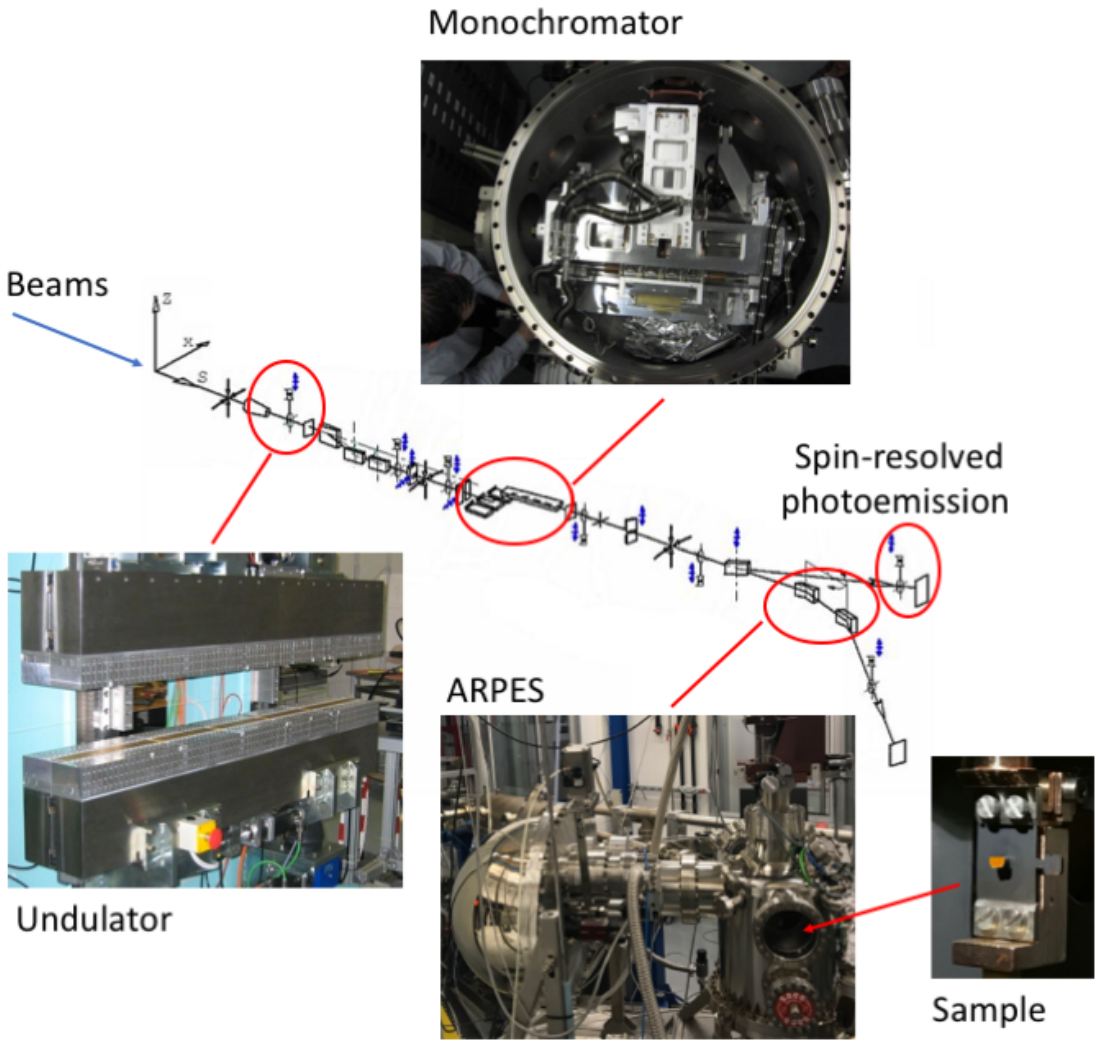

Figure 2.11: At the center, the CASSIOPEE beam line. On the top, photo showing the inside of the monochromator, with a plane mirror above the four available gratings. On the bottom-left, photo of the high photon energy HU60 undulator. On the bottom-middle, photo of the ARPES setup used in the PhD showing the scienta detector and the measuring chamber. On the bottom-right, photo of one of our sample placed inside the measuring chamber.

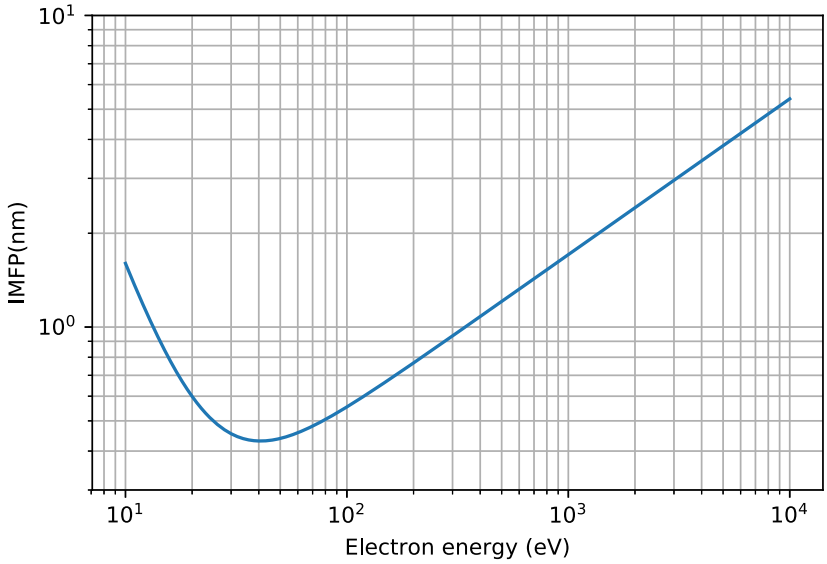

Figure 2.12: Universal curve for the electron inelastic mean free path. [56]

depth increases. Probing depths in photoemission are determined by the inelastic mean free path (IMFP), related to the distance that an electron can travel before suffering an inelastic collision. Electrons lose their energy by exciting plasmons or vibrations [55]. The intensity of photoelectrons after traveling a depth d is attenuated exponentially according to:

$$I(d) = I_0 e^{-\frac{d}{\lambda(E)}}, \tag{2.12}$$

where I_0 is the initial intensity, and $\lambda(E)$ is the IMFP, representing the distance that electrons can travel before the intensity decreases to $1/e$ of the initial value.

IMFP can be presented as a function of the kinetic energy of the electrons:

$$\lambda = \frac{143}{E^2} + 0.054 \cdot \sqrt{E}. \tag{2.13}$$

As shown in Fig. 2.12, IMFP has a minimum around 50 eV and then increases when decreasing or increasing the kinetic energy. This means that by changing the kinetic energy of photoelectrons, i.e. by tuning the photon energy of the photoemission process, we can probe different depths of an heterojunction.

Therefore, to investigate various kinds of layers and interfaces buried at different depths, by varying the incident photon energy, we tune the surface-sensitive technique to a bulk-sensitive measurement [57, 58].

In this thesis, we measured at GALAXIES beamline of SOLEIL synchrotron, with the help of Jean-Pascal Rueff and Denis Ceolin. GALAXIES is a hard x-ray spectroscopy beamline

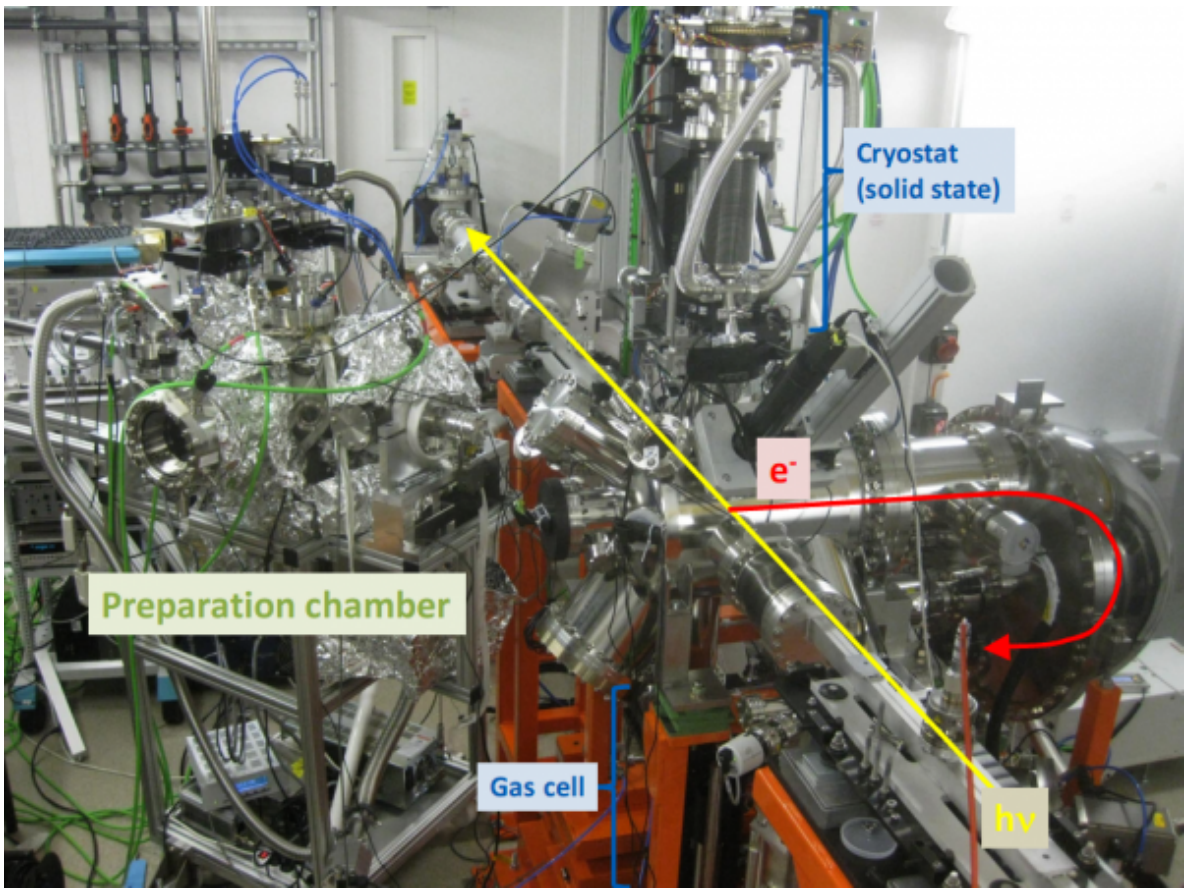

Figure 2.13: The experimental setup of HAXPES at GALAXIES beamline. The HAXPES end-station consists of an analysis chamber equipped with a 4-axes manipulator associated to a cryogenic system (20 K) for solid sample (middle-top) and a cell for measurements on gas phase (middle-bottom), an analyzer (right), and a preparation chamber (left).

dedicated to inelastic x-ray scattering (IXS) and to HAXPES. The beamline is equipped with an in-vacuum U20 undulator delivering photons between 2.3 to 12 keV kinetic energy. The HAXPES end-station is equipped with a high energy/ high resolution electron analyzer (to overcome the rapid decrease in photoionization cross section when increasing the photon energy [59, 60]) with a resolution of 30 meV at 12 keV electron kinetic energy. The experimental setup of HAXPES end-station is shown in Fig. 2.13. The HAXPES end-station consists of an analysis chamber equipped with a 4-axes manipulator associated to a cryogenic system for solid samples allowing to cool down to 20 K and a cell for measuring gas phase samples. The analyzer is placed perpendicularly to the incident beam. A preparation chamber is coupled to the analysis chamber, and allows to prepare and characterize samples. The chamber hosts an ion gun, evaporators and a LEED.

2.3.2 Inverse photoemission spectroscopy

In photoemission, the extraction of electrons by the incoming photons allows to study the occupied states. In order to study the unoccupied states, we need to use Inverse Photoelectron Spectroscopy. Technically, in IPES the reverse of photoemission is done, i.e. the sample is exposed to an electron beam and the emitted photons are collected (electron in - photon out technique) [61]. The efficiency of inverse photoemission is much lower than that of the direct photoemission. The difference of the efficiency is due to the different cross sections of the processes. The ratio r of cross sections is:

$$r \equiv \left(\frac{d\sigma}{d\Omega}\right)_{IPES} \left(\frac{d\sigma}{d\Omega}\right)^{-1}_{PES} = \frac{w^2}{c^2 k_e^2}, \tag{2.14}$$

where ω is the energy of the emitted photon, c is the light velocity, and k_e is the wave vector of the incident electron. Equivalently, it can be represented as:

$$r = \left(\frac{\lambda_e}{\lambda_p}\right)^2, \tag{2.15}$$

where λ_e and λ_p are the electron and photon wavelengths respectively. The inherently low signal level of IPES is because the ratio r is about 10^{-4} - 10^{-5}.

It is therefore necessary to integrate the signal for longer times than in photoemission. Except for this difference, the bands can also be obtained with k-resolution. Thanks to the conservation of the parallel component of the electron wave-vector when it crosses the surface barrier, the unoccupied band structure $E(k_{||})$ can be determined in the entire reciprocal space, making IPE a powerful $k_{||}$-resolved spectroscopy known as KRIPES or ARIPES [62]. The angular resolution is obtained by changing the orientation of the sample with respect the electron beam. IPES technique can be implemented in two different ways. One way consists in varying the incident electron energy, and detecting with a fixed photon energy detector, which is the isochromatic mode. The other implementation consists of detecting different photon energies with a monochromator while keeping the incident electron beam energy constant.

The results from this thesis were obtained with the isochromatic mode of IPES in the team of Jean-marc Themlin in Institut Materiaux Microélectronique Nanosciences de Provence (IM2NP), Marseille, in collaboration also with Younal Ksari and Luca Giovanelli. The working principle of this mode is shown in Fig. 2.14, and the experimental setup and the sample holder are shown in Fig. 2.15. The electron gun emits an electron beam of variable energy towards the sample. The electron gun needs to be placed as close as possible to the target (Fig. 2.15(b)). Hence, the electron gun needs to be small in order not to shadow photons emitted from the sample, but also it must be highly-efficient to get sufficient inverse photoemission signal. The electron gun used in these IPES studies follows the design of Erdman and Zipf [63]. The energies used in our work were between 8 eV and 18 eV. The electron having reached the

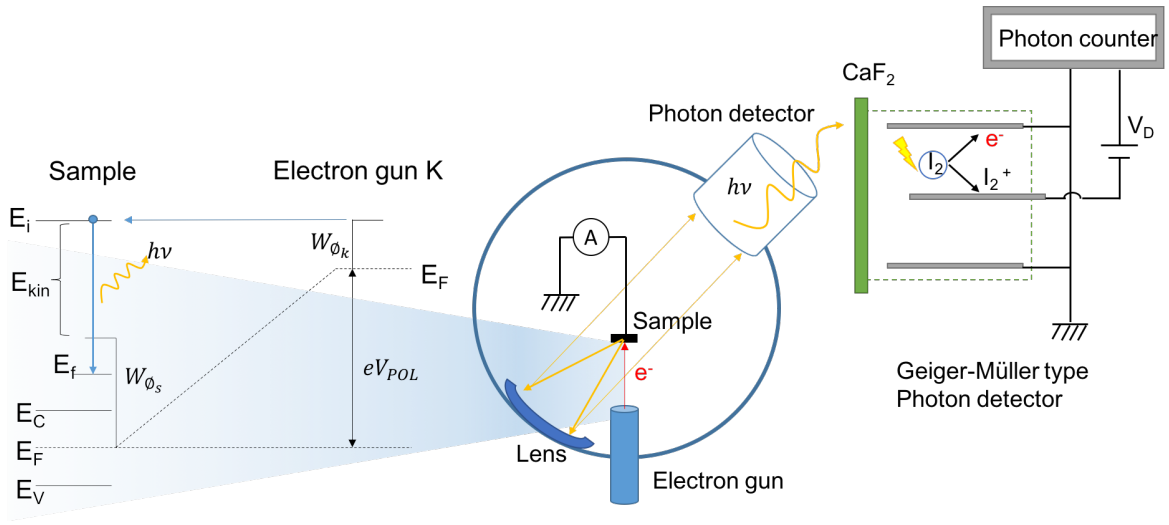

Figure 2.14: The working principle of IPES. (middle) An electron gun emits an electron beam of variable energy (from 8 eV to 18 eV in our case) towards the sample. An elliptical mirror collects the photons. (left) These electrons can be injected in the unoccupied states (initial state, E_i) of the sample, and then, by releasing to a lower energy of unoccupied states (final state, E_f) in the conduction band, a photon with certain energy can be emitted and detected. (right) The photons are detected by a Geiger-Muller detector. Via the photochemical reaction of iodine and the photons with sufficient energy, the photons can be detected

sample is de-excited to a lower energy unoccupied state. In this process, the sample emits a photon with an energy corresponding to the energy difference between the initial state energy (E_i) and the final state energy (E_f) of the electron.

Once photons are emitted from the samples, an elliptical mirror collects them. The sample is placed at one of the focal points of the mirror, towards a bandpass photon detector situated at the other focal point [64]. In addition, the sample should be placed close enough to the electron gun. This minimizes the electron beam dispersion arising from the space charge effect, before it hits the target.

The photon detector of the setup is a Geiger-Muller detector (Fig. 2.14, right panel), adapted by Dose for IPES instruments [65, 66]. It is a cylinder with a CaF_2 window that is transparent for photons below 10.2 eV and works as a low-pass filter. The cylinder is filled with a mixture of iodine gas, with a partial pressure equal to the vapor pressure of several iodine crystals, and helium gas of several millibars. Photons with energies $h\nu > 9.23$ eV allow to trigger a photochemical reaction:

$$I_2 + h\nu \rightarrow I_2^+ + e^-, \tag{2.16}$$

which acts therefore as a high pass filter. Together with the low-pass property of the CaF_2 window, the entire setup works as a bandpass detector for photon energy of 9.70±0.40 eV

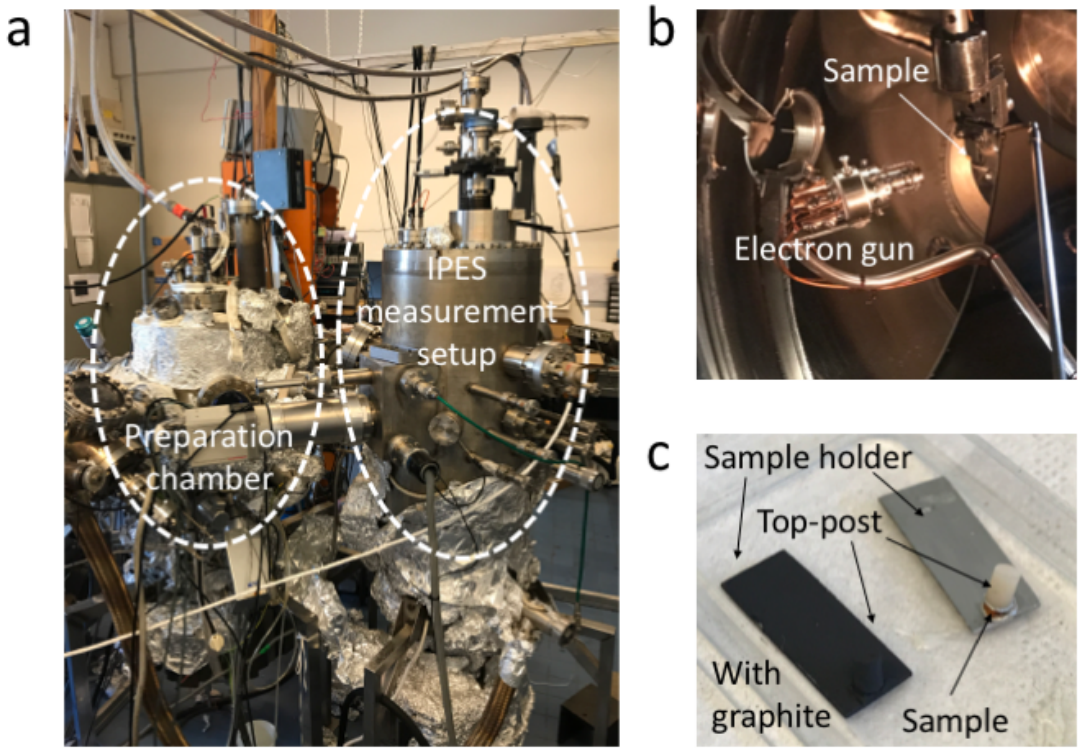

Figure 2.15: (a) The experimental setup of IPES in l'Institut Matériaux Microélectronique Nanosciences de Provence (IM2NP). The left part is the preparation chamber, and the right part is the IPES measurement chamber. (b) Experimental geometry during the measurement, showing how close is the electron gun to the sample. (c) Sample mounting. On the left, sample holder with graphite. On the right, sample holder with a PEPI sample and a top post on top to cleave the sample under UHV.

[67]. In the cylinder axis, there is a stick isolated from the cylinder. When applying a voltage of 300 - 450 V to the electrode stick, the electrons created by the ionization by the photons of the gas mixture inside the cylinder are accelerated towards the axis. These electrons generate a sudden increase of the current, that is detectable after amplification. Photons are detected through this current increase.

2.3.2.1 Technical aspects of the data analysis

To analyze IPES spectra, it is important to figure out the Fermi level position. This is obtained by measuring a metallic surface (a clean tantalum sample for instance). Fig. 2.16 shows how E_F changes in a Ta sample when different emission currents are used. In this work, we used an emission current I_f of 1.77 mA, in order to minimize the sample degradation [64]. We have therefore $E_F = 8.66$ eV as determined by the maximum of the first derivative of the spectral starting edge.

In our analysis, we also need to figure out the cathode work function. Once E_F is known, the work function of the electron gun cathode can be extracted:

$$W_{\phi_k} + eV_{POL} = E_{kin} + W_{\phi_s} = h\nu + (E_f - E_F), \tag{2.17}$$

where the magnitudes are defined in Fig. 2.14. Here, $h\nu = 9.7$ eV and $E_F = eV_{POL} = 8.66$ eV. When E_f approaches E_F, $E_f - E_F = 0$. The work function of W_{ϕ_k} is:

$$W_{\phi_k} = h\nu - eV_{POL} = 9.7 - 8.66 = 1.04(eV). \tag{2.18}$$

Finally, another aspect to be considered is that a strong background is superimposed to IPES spectra. The background is due to the electrons emitted from the cathode that undergo inelastic collisions and lose part of their energy before emitting a photon. These inelastic electrons are measured at lower energies than E_i and generate the background signal [64].

2.3.3 Theoretical band structure determination

In this thesis, the experimental band structure obtained by photoemission or inverse photoemission has been compared to theoretical calculations. An accurate simulation of the experiments needs to determine first the theoretical band structure, and then simulate the photoemission process. The band structure seemed a few decades ago complicated to obtain, as a solid is a many-body system with a huge number of particles, of the order of the Avogadro number. The wave function of the solid holds therefore a large amount of information, and makes exact or analytical calculations impractical or even impossible. In order to describe a solid, many-body theoretical physics relies now on a set of computationally available approximations, specific to the problem at hand. One approximation consists of mapping the

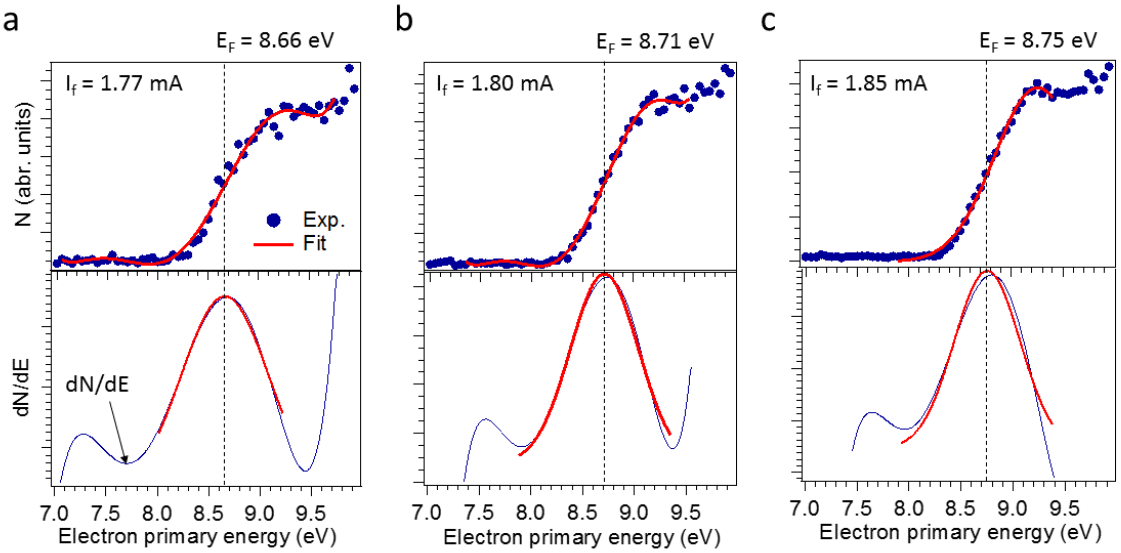

Figure 2.16: E_F position for different emission currents of the electron gun. Measurements were performed on a clean Ta sample.

many-body problem onto a single-body problem via the Density Functional Theory (DFT), which allows to express the physical properties of the ground state in terms of the electronic density. In this thesis, the photoemission calculation will be based on the DFT method, and the details of the photoemission theory will be described in the following.

2.3.3.1 Photoemission spectroscopy theory

About 50 years ago, photoemission theory was an intractable many-body problem [68, 69, 70] to be solved without strong approximations. The first description of the photoemission process considered a one-electron approximation, and decomposed artificially the photoemission process in three steps, i.e. the so called three-step model of photoemission , which was introduced by Berglund and Spicer [71]. Later on, this model was replaced by the one-step model of photoemission. We describe below these two models.

Three-step model In the framework of this model, the photoemission process is decomposed into three independent steps:

(1) Photon excitation of the electrons in the solid from an initial state E_i to a final state E_f

(2) Migration of the photoelectrons toward the sample surface

(3) Crossing the surface barrier by photoelectrons, with conservation of the momentum component parallel to the surface, $k_{||}$.

In the first step, as states belong to the solid, the corresponding wave functions can be expressed by Bloch functions and the momentum $\boldsymbol{k}$ is conserved. In addition, for low photon energies, the momentum of the photon is negligible compared to that of the electron, i.e. the initial and final momentum values of the electron are equal: $\boldsymbol{k_i} = \boldsymbol{k_f}$. In the second step, the interaction between the outgoing electron and the remaining electrons is neglected most of the time, although the photoemission intensity is attenuated due to the propagation to the surface. In the last step, the momentum of the electron inside the material $\boldsymbol{k}$ and its momentum when expelled to the vacuum $\boldsymbol{K}$ are decomposed into parallel and perpendicular components as shown in Fig. 2.10, the component being conserved.

One-step model The three-step model works extremely well, but it is just a phenomenological model. A more precise model, the one-step approach model, was first developed by Pendry [72]. It considers that there is no reason to decompose the photoemission process into three differentiated steps. It therefore combines the three steps into one, in which the electron goes directly from an initial state defined in the material into the final state defined in the vacuum. The aim of the one-step approach model is to describe the three steps as a single quantum-mechanically coherent process including all multiple-scattering events.

The electronic structure of solids can be extracted from photoelectrons, if the sudden approximation is satisfied. As it is necessary that photoelectrons are detected before the state relaxes to another electronic state. In this situation, the energy conservation laws (2.7 and 2.6) allow to obtain information on the initial electronic state.

In the sudden approximation, the one-step approach model is a numerically solvable scheme where the retarded one-electron Green function for the initial state is replaced with the one-particle Green function, determined by DFT. In these conditions, the photoemission intensity at finite temperature is:

$$I(\boldsymbol{k},\omega) = I_0(\boldsymbol{k},\nu,\boldsymbol{A}) f(\omega) A(\boldsymbol{k},\omega), \tag{2.19}$$

where $\boldsymbol{k} = k_{||}$ is the in-plane wavevector, ω is the energy related to Fermi level, $I_0(\boldsymbol{k},\nu,\boldsymbol{A}) \propto \left|M^{\boldsymbol{k}}_{f,i}\right|^2$ is the matrix element associated to the optional transition (which is related to the wavevector of the electrons, the energy and polarization of incident photons [51]), $f(\omega) = (e^{\omega k_B T} + 1)^{-1}$ is the Fermi-Dirac distribution function (which defines the occupancy of the energy levels and is responsible that photoemission only probes occupied states), and $A(k, \boldsymbol{w})$ is the single particle spectral function, which is related to $-\frac{1}{\pi}$ of the imaginary part of Green's function [73]:

$$A(\boldsymbol{k},\omega) = -\frac{1}{\pi} ImG(\boldsymbol{k},\omega). \tag{2.20}$$

By considering the electron self-energy $\sum(\boldsymbol{k},\omega) = \sum'(\boldsymbol{k},\omega) + i\sum''(\boldsymbol{k},\omega)$, the interaction

between electrons and other particles appears explicitly in the Green's function. $\sum'(\boldsymbol{k},\omega)$ and $\sum''(\boldsymbol{k},\omega)$ are the real and imaginary parts of electron self-energy. The real part of the electron self-energy is identified with the physical self-energy, on the other hand, the imaginary part of the electron self-energy is a measure for the lifetime of the electron under the investigation. The Green's function and the single particle spectral function can also be rewritten as:

$$G(\boldsymbol{k},\omega) = \frac{1}{\omega - \varepsilon_{\boldsymbol{k}} - \sum(\boldsymbol{k},\omega)}, \tag{2.21}$$

and

$$A(\boldsymbol{k},\omega) = -\frac{1}{\pi}\frac{\sum''(\boldsymbol{k},\omega)}{[\omega - \varepsilon_{\boldsymbol{k}} - \sum'(\boldsymbol{k},\omega)]^2 + [\sum''(\boldsymbol{k},\omega)]^2}. \tag{2.22}$$

By analyzing the photoemission spectra with the spectral function, the real and imaginary parts of electron self-energy can be extracted to study the many-body interaction in solids. Therefore, the one-step model allows to consider the photoemission process explicitly.

Within this model, self-energy corrections are in both the initial and the final states. In this thesis, we have treated the initial and final states within the Spin-Polarized Relativistic Korringa-Kohn-Rostoker Method (SPR-KKR method) [74, 75], a straightforward method to describe the photoemission from complex layered structures, such as thin films and multilayers [76]. SPRKKR calculations are described in the following subsection.

2.3.3.2 Spin-Polarized Relativistic Korringa-Kohn-Rostoker Method

The Korringa-Kohn-Rostoker (KKR) Method [77, 78] for calculating the electronic structure of arbitrary three-dimensional periodic systems is based on the concepts of the KKR-Green's function that makes use of the Multiple Scattering Theory (MST). This implies that the information on the electronic structure is not expressed in terms of Bloch wave functions and eigenvalues, but on the corresponding Green's function, to describe the multiple scattering.

Multiple scattering theory basis were settled in the end of 17^{th} century, when Huyguens proposed that all points of a light wavefront can be considered as independent sources [79]. The MST became popular in theoretical physics in the middle of the 20^{th} century when Korringa [80], Kohn and Rostoker [81] demonstrated that the MST can be applied to electronic waves in the calculation of electronic bands of materials. Later on, when the Green's function was also associated to the system, the so-called KKR-GF method appeared [82]. In the following decades, the method was developed for both non-relativistic [83, 84, 85, 86] and relativistic cases [87, 88, 89, 90].

The spin-polarized relativistic Korringa-Kohn-Rostoker (SPRKKR) Green's function method is based on the Dirac-Hamiltonian for a spin-polarized system, i.e. it solves the spin density functional theory:

$$\left(-i\hbar c\boldsymbol{\alpha}\cdot\boldsymbol{\nabla}+\beta mc^2+V_{eff}+e\boldsymbol{\alpha}\cdot\boldsymbol{B_{eff}}\right)\psi_i=E_i\psi_i, \tag{2.23}$$

where V_{eff} and B_{eff} are the potentials functions, Ψ_i is energy-dependent four-component spinor functions for energy E_i. To solve this equation, an ansatz of the wave function is made $\psi_\nu=\sum_\Lambda \psi_{\Lambda\nu}$, which can be expressed as a linear combination of the partial waves $\psi_{\Lambda\nu}$. It combines with the relativistic quantum number $\Lambda=(\kappa,\mu)$, where κ and μ are the spin-orbit and magnetic quantum numbers, respectively.

After having solved the set of coupled equations for the wave functions Ψ_i, the corresponding single-site t matrix is obtained by standard matching to the Hankel and Bessel functions as free-electron solutions. With the available single-site t matrix, the next step is to solve the multiple scattering problem. By using the scattering path operator τ, this problem can be solved [77]. In a finite system, the multiple scattering problem can be solved directly by inverting the so called KKR-matrix, $\underline{\underline{\tau}}=[\underline{\underline{t}}^{-1}-\underline{\underline{G_0}}]^{-1}$, with the double underline indicating matrices with respect to the site and the spin-angular (Λ) character. In the end, the retarded site-diagonal Green's function $G(\boldsymbol{r},\boldsymbol{r'},E)$ can be written as [79, 86]:

$$G(\boldsymbol{r},\boldsymbol{r'},E)=\sum_{\Lambda\Lambda'}Z^n_\Lambda(\boldsymbol{r},E)Z^{n'\times}_{\Lambda'}(\boldsymbol{r'},E)$$

$$-\sum_\Lambda[Z^n_\Lambda(\boldsymbol{r},E)J^{n\times}_\Lambda(\boldsymbol{r'},E)\Theta(r'-r)+J^n_\Lambda(\boldsymbol{r},E)Z^{n\times}_\Lambda(\boldsymbol{r'},E)\Theta(r-r')]\delta_{nn'}. \tag{2.24}$$

where $r(r')$ lies in the atomic cell n, which represents cell-centered coordinates, and $\times$ indicates a "left-hand side solution" [91]. With the Green's function above, all electronic properties of interest can be calculated directly.

With SPRKKR method, the one-electron Green's function can be delivered directly and the electronic band structure of arbitrary three-dimensional periodic systems can be calculated. Based on the electronic structure calculated by SPRKKR, many different properties can be investigated, especially for the response functions and other spectroscopic properties that apply with the fully relativistic mode. Therefore, within the one-step model of photoemission, SPRKKR method can calculate ARPES results in a wide range of photon energy. This allows in particular a direct comparison with our experimental results.

SPRKKR offers many advantages compared to other band structure calculation methods because of their representations of the electronic structure corresponds to single-particle Green's function [77], allowing to combine SPRKKR method with the dynamical mean-field theory straightforwardly. With the combination of the dynamical mean-field theory, one can easily deal with the strongly correlated materials. Another important outcome is the possibil-

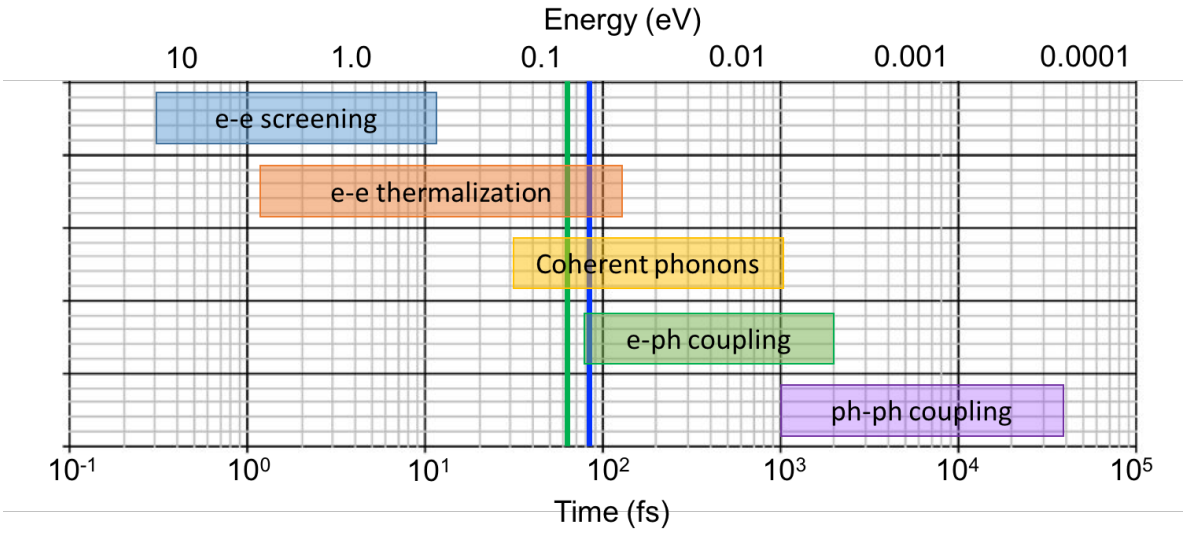

Figure 2.17: Typical timescales (bottom axis) and energy scales (top axis) of coherent phonons, electron-electron (e–e) interaction, electron-phonon (e–ph) interaction and ph–ph interaction in correlated metals. The green and blue line indicate the temporal duration of our pump and probe pulses, respectively. (adapted from [92])

ity of using the Dyson equation. This relates the Green's function of a perturbed system with the Green's function of the corresponding unperturbed reference system. With the Dyson equation, the properties of low dimensional systems, such as semi-infinite 2D-surfaces, nanostructures or embedded 3D- or 2D- systems, can be obtained without using an artificial super cell construction.

2.4 Electron de-excitation dynamics

The efficiency in photovoltaic materials as the ones studied in this thesis depends not only on the static band structure, but also on the electron dynamics following a photoexcitation. Different processes can affect the electrons dynamic, depending on the time scale [51], e.g. electron-electron thermalization, electron-phonon scattering.... All these processes have different characteristic decay times allowing to relax the system back to the equilibrium state [92]. For example, scattering processes due to e–e and e–ph interactions take place in a few femtoseconds and a few picoseconds, as shown in Fig. 2.17. One way to study the de-excitation dynamics, is by the time-resolved two-photon photoemission spectroscopy (Tr-2PPE) [93].

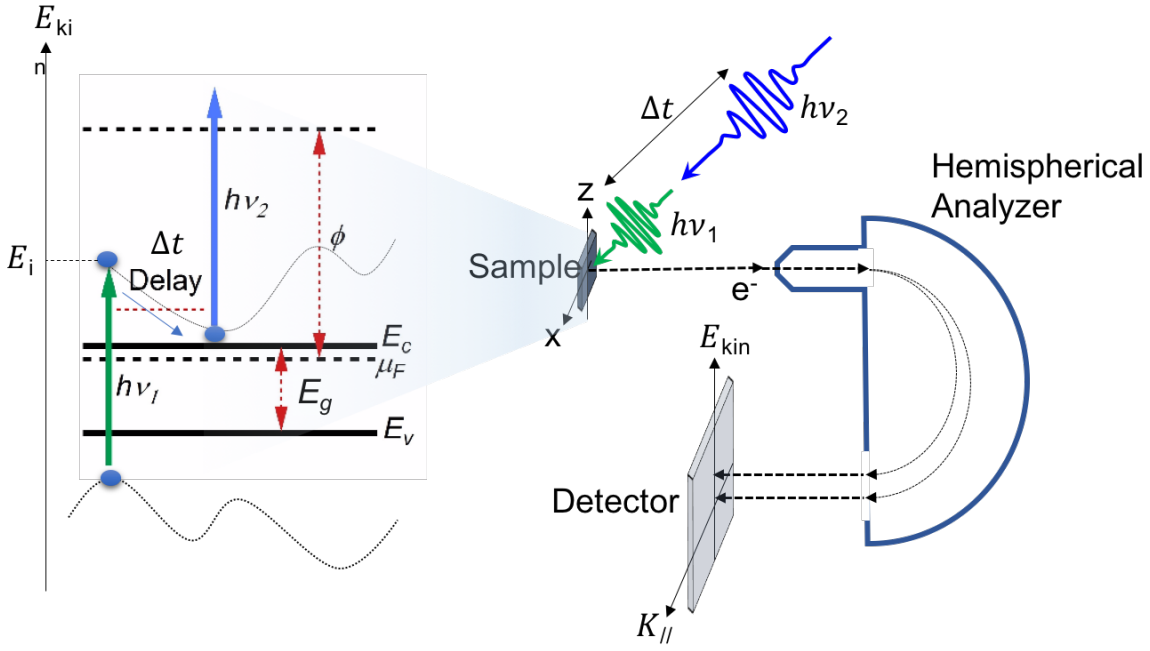

Figure 2.18: Time-resolved 2PPE working principle (left) and experimental scheme (right). $h\nu_1$ is the pump excitation energy and $h\nu_2$ is the probe photon energy.

2.4.1 Two-photon photoemission

Two-photon photoemission spectroscopy (2PPE) allows to investigate unoccupied electronic states located between the Fermi level and the vacuum level of a metal or a semiconductor. A first laser pulse (pump) with photon energy $h\nu_1$ populates the unoccupied state E_i, and a second laser pulse (probe) with photon energy $h\nu_2$ photoemits the electrons, delayed by Δt with respect to the pump (Fig. 2.18). In the usual scheme of 2PPE, $h\nu_1$ and $h\nu_2$ are below the work function, so that no signal arising from direct photoemission can take place. On the contrary, the combination of $h\nu_1$ and $h\nu_2$ is above the material workfunction, photoemission can be induced, providing a snapshot of transient states and their de-excitation dynamics.

The intensity from a given intermediate state as a function of the delay time Δt between the pump and the probe is defined by the lifetime of the intermediate state. The photoemitted electrons are collected by an ARPES spectrometer to map the intensity as a function of kinetic energy and emission angle. By gradually delaying the Δt, the de-excitation dynamics can be characterized from tenths of fs to more than a few hundreds of ps.

The time-resolved 2PPE experiments carried out in this thesis were performed in the FemtoARPES setup, in collaboration with Luca Perfetti and Evangelos Papalazarou. FemtoARPES combines a laser source, the optics for generating UV pulses, and an ARPES setup (Fig. 2.19). The laser is a regenerative Titanium: Sapphire laser system (RegA by Coherent).

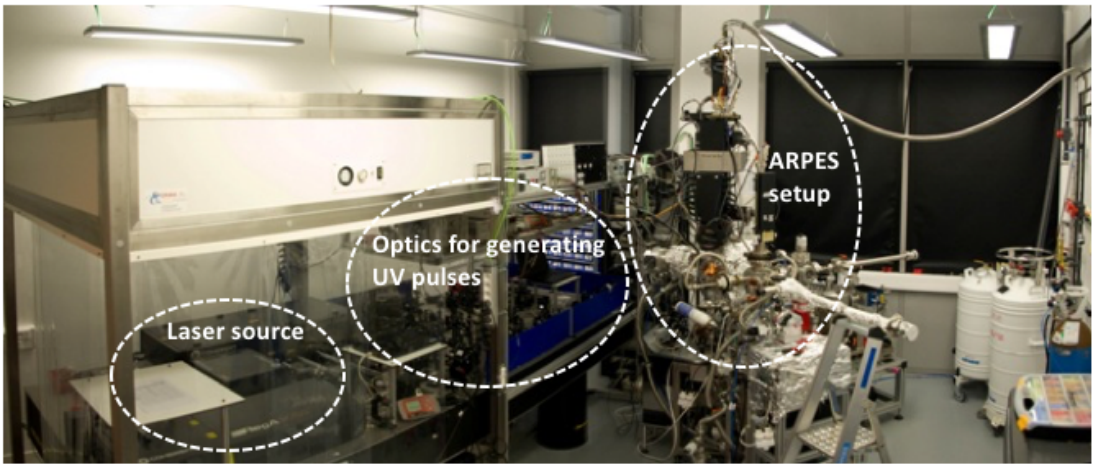

Figure 2.19: FemtoARPES experimental setup showing the laser source (left) the optics for generating UV pulses (middle) and the ARPES setup (right).

The laser has a high repetition rate (250 kHz) and delivers 6 μJ per pulse with 35 fs duration at FWHM. The laser wavelength can be tuned between 780 nm and 820 nm for a safe and stable operation. Since the laser light generated from the Titanium: is only 1.55 eV, which is less than the 4˜5 eV work function of most materials, higher harmonics of the fundamental photon energy are needed to allow a photoemission process. Higher harmonics are produced through nonlinear optical processes in BBO crystals. For this thesis, we developed a particular pumping system combining a pump at 2^{nd} harmonic and a probe at 3^{rd} harmonic. The probe beam path can be controlled with a delay line. The fourth harmonics (FH) with the photon energy of 6.28 eV (197.5 nm) and a fluence of 10^{12} photons/s for the laser system is also reachable.

Part II

Hydrogenated amorphous-silicon

Chapter 3

Structural and electronic modification of amorphous-silicon heterojunction by ion irradiation

3.1 Introduction

Thin-film silicon solar cells are one of the possible solutions to the increasing energy demand. In particular, hydrogenated amorphous silicon (a-Si:H) is of particular interest nowadays. It can be used as an intrinsic absorber layer, sandwiched between doped layers to form PIN junctions, and it can be combined with crystalline silicon wafers in heterojunction solar cells [1]. It has been reported that the efficiency of a-Si:H heterojunction solar cells has reached over 26%, which is close to the theoretical conversion efficiency limit of Si solar cells 29.1% [2].

One of the factors that affect the solar cell efficiency are defects. A better understanding of defects, especially within the interface between the c-Si wafer and a-Si:H could help to increase the open-circuit voltage (V_{oc}), and short-circuit current (J_{sc}) of the heterojunction solar cells, resulting in an increase of their efficiency. Defects affect the efficiency through the additional electronic states that they generate in the band gap. Two kinds of defect states can appear there: mid-gap and bandtail states. Mid-gap states act as highly efficient recombination centers. They arise from dangling bonds, and are problematic for a-Si:H solar cells and other electronic applications. Bandtail states are less detrimental for the efficiency, and their concentration is related to the mid-gap states density. They are a consequence of disordered localized electronic states appearing close to the edges of the conduction and valence bands.

In this study, defects were introduced by ion irradiation. During Ar ion implantation, the Si-H bonds in a-Si:H could be broken and become dangling bonds, which could generate the

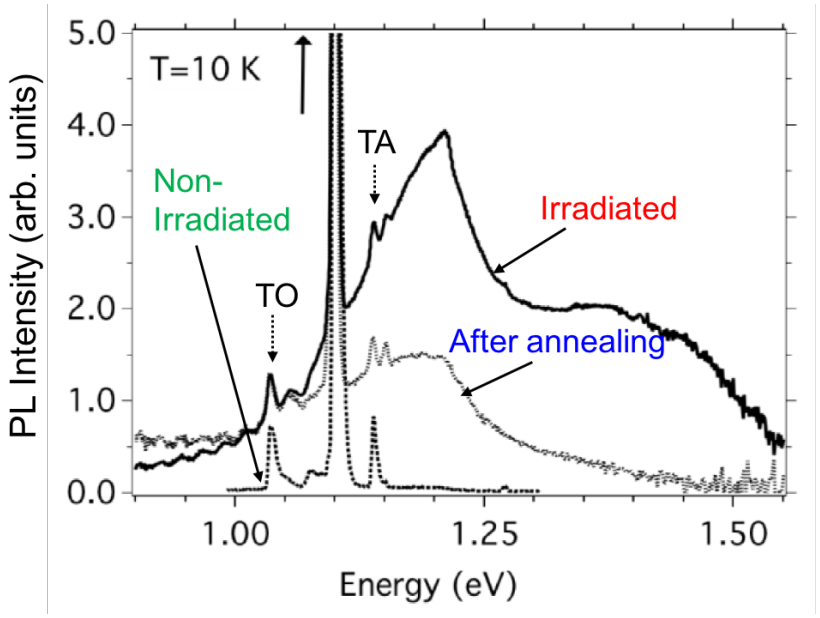

Figure 3.1: Photoluminescence measurements on the non-irradiated, irradiated, and irradiated + annealed samples (adapted from [39]). Here, TA stands for transverse acoustic phonons and TO for transverse optical phonons.

mid-gap defect states. By controlling the fluence of Ar ions and their energy, the depth of the impact region , i.e. the defects location, can be controlled. Therefore, the ion irradiation technique is a convenient way to control defect formation.

A first information from the defects can be obtained from photoluminescence. In particular, this technique has allowed to identify a defect induced state on a-Si:H heterostructure [39]. Fig. 3.1 compares the photoluminescence on a-Si:H heterostructures with different treatments (non-irradiated, irradiated and irradiated and annealed samples). There are mainly two peaks. The most intense peak at 1.1 eV corresponds to the band gap of c-Si (1.1 eV), associated with the photoluminescence from c-Si. The small peaks above and below the peak at 1.1 eV are origin from the transverse acoustic phonons (TA), and the transverse optical phonons (TO). A broader and less intense peak appears around 1.2 eV, an energy smaller than the band gap of amorphous Si (1.7 eV). This broad energy transition around 1.2 eV is detrimental for generating photocurrent since possibility of the recombination at the interface increases [94]. Upon annealing at 300°C, the photoluminescence peak decreases in intensity, probably indicating that defects are being healed. This optical transition indicates the presence of states inside the gap of a-Si:H [24], whose nature is to be identified. In particular, as photoluminescence only identifies optical transitions, the exact location of the states within the gap of a-Si:H needs to be identified, i.e. if they are close to the valence band maximum or to the conduction band minimum.

	3 keV		5 keV		8 keV	
	Si 2p(3/2)	C 1s	Si 2p(3/2)	C 1s	Si 2p(3/2)	C 1s
a-Si:H (L1) (Å)	58.3	63.1	90.4	87.5	135.6	132.9
a-SiC:H (L2) (Å)	62.0	56.4	96.3	93.2	144.7	141.8
Substrate (S) (Å)	56.0	53.2	84.0	81.6	121.7	119.4

Table 3.1: Inelastic Mean Free Path in the different layers for different photon energies determined from SESSA.

To understand these defect states, we have studied their location in the heterojunctions, their number and their position within the band gap. Since these defects are buried, we have studied them by hard x-ray photoemission spectroscopy (HAXPES). Different photon energies allowed us to study the defects in different regions of the a-Si:H heterojunction. We have studied both the different chemical environments of Si atoms, in order to quantify the dangling bonds and the Si-H bonds ratio, as well as the valence band states, to observe directly the defect states at the VBM. These studies will be presented in sections 3.2 and 3.3, respectively.

3.2 Quantification of defect implantation in amorphous silicon heterostructure

High energy photoemission in amorphous Si heterostructures allows to determine the nature of the defects and their relative amounts. This information is contained in the core levels of the chemical species present in the sample. In order to study the different layers of the heterostructure, we need to adapt the inelastic mean free path of the exiting electrons.

IMFPs can be obtained from the database of the Simulation of Electron Spectra for Surface Analysis (SESSA) provided by the National Institute of Standards and Technology (NIST) [95]. The IMFP of electrons in different core level are simulated by taking into account the thickness and atomic density of each layer in our heterojunction sample. the The IMFP of electrons escaping from the heterojunction is shown in Table 3.1 and in Fig. 3.2. As the kinetic energy needed to eject electrons from different core levels are different, the IMFP of the electrons from different core levels also vary. The heterojunction geometry under this study consists of a top layer of 7 nm of a-Si:H (L1 = 7 nm), a bottom layer of 3 nm of a-SiC:H (L2 = 3 nm), and a 280 μm thick substrate of c-Si (S).

Fig. 3.2(a) shows the IMFP simulation of electrons excited from different layers and the depth of our 10 nm thick sample. It can be seen that a photon energy of 3.5 keV allows to

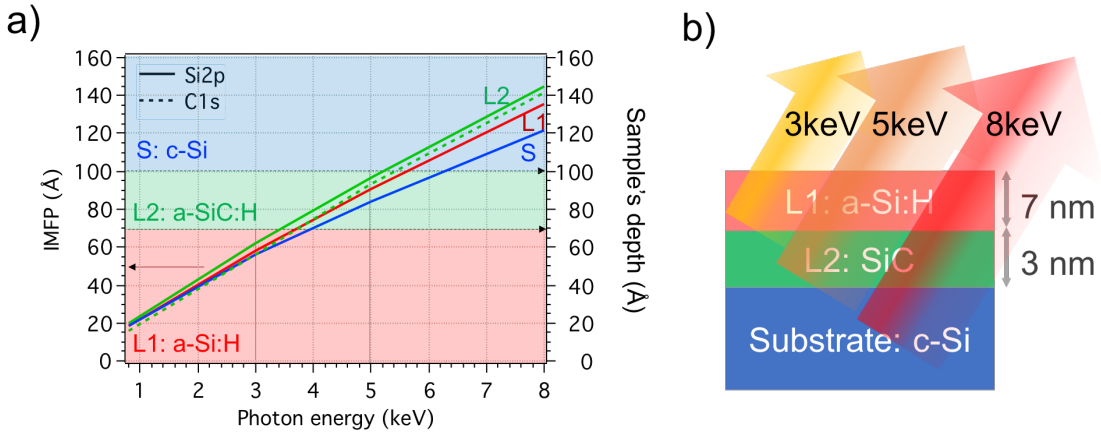

Figure 3.2: (a) Simulation of the Inelastic Mean Free Path of Si2p (solid line) and C1s (dotted line) for different layers (L1: red, L2: green, and S: blue) as a function of photon energy. Background colors represent the depth of each layer in the heterostructure (right axis) (b) The photoexcited electrons can be extracted from different depths of the heterojunction with different photon energies.

excite most of the electrons from a-Si:H (L1, red area). If we choose 3 keV of photon energy, the main signal will be from the a-Si:H layer. The inelastic mean free path starts to reach the a-SiC:H depth for photon energies above 3.5 keV. Below 5.2 keV of photon energy, the signal of the c-Si will be minimal. Thus, if we use 5 keV of photon energy, we avoid to probe significantly the substrate (S, c-Si). If we use 8 keV of photon energy, the main signal will be coming from electrons from substrate. From this simulations, we selected three photon energies (3 keV, 5 keV, and 8 keV) for studying the different layers as shown in Fig. 3.2(b).

3.3 Reactivity increase upon irradiation

In the studied heterostructure, most of the defects will be related to silicon atoms. Core level spectroscopy of the Si 2p as a function of the depth will therefore provide valuable information. Fig. 3.3 shows the Si 2p core level spectra for irradiated and non irradiated samples. The overall line-shape of the Si 2p core level reveals the presence of a peak at 4 eV of relative binding energy with respect the main peak. This peak is characteristic of Si^{4+}, usually appearing when SiO_2 is present on the system. The Si^{4+} component is stronger in the shallower layer, i.e. at the a-Si:H layer. Since the Si^{4+} component increases in the shallower layer (close to the surface) after irradiation, it is evident that the irradiated sample is more reactive towards oxidation, possibly because of the increase in the number of dangling bonds. We will analyze this point in more detail in the next section.

After analyzing the Si 2p, we have observed the general line-shape of C 1s (Fig. 3.4). It can

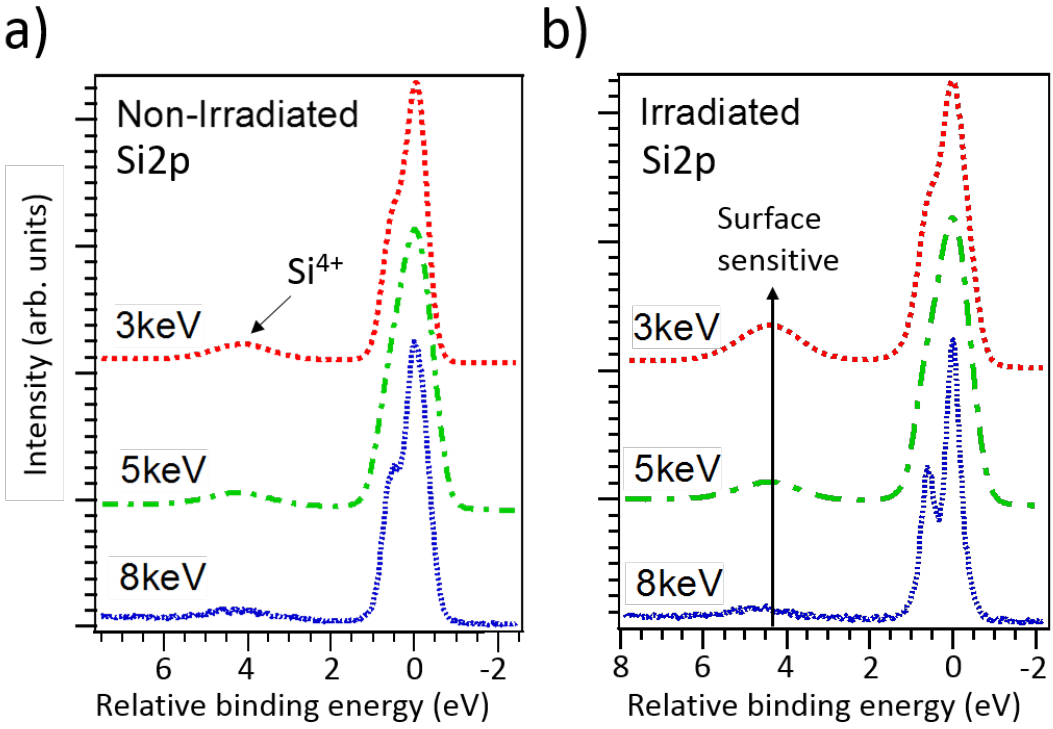

Figure 3.3: Si 2p core level measured under different photon energy for (a) a non-irradiated sample and (b) an irradiated sample. The binding energy is relative to the binding energy of the bulk component (99.4 eV). The increase of Si^{4+} component towards the surface shows its surface sensitive (also surface reactivity) property. On the other hand, the bulk component of Si 2p shows a bulk-like behavior at high photon energy since the feature of the Si 2p splitting becomes more evident due to the presence of a unique major component.

Fitting parameter	Si2p (c-Si)
Spin-orbit splitting	0.6 ± 0.01 eV
Branching ratio	0.51 ± 0.01
Lorentzian width W_L	0.15 ± 0.01 eV
Gaussian width W_G	0.34 ± 0.05 eV

Table 3.2: Fitting parameters of the bulk component of Si 2p.

be observed at naked eye that irradiation enhances a component C1 of -2 eV of relative binding energy. This energy is compatible with C-C, C-H, or SiO_xC_y [96, 97] or a combination of them. This component increase in the a-Si:H layer upon irradiation. Such effect can be explained from a surface diffusion of C atoms of the underlying SiC bulks layer upon irradiation. A minor component C2 at -4.5 eV binding energy, associated to C-O bonds, increases after the irradiation as well, indicating that the sample is more reactive as we saw previously.

3.4 Quantification of defects in the a-Si:H layer

Defects in the a-Si:H layer can be quantified by decomposing the Si 2p core level. Core level spectroscopy is precisely one of the rare techniques that is sensitive to H atoms. This sensitivity is obtained through the chemical shift that the bonding to a H atom induces on another one. We have therefore analyzed the Si 2p core level to identify Si-H bonds. This analysis needs the accurate decomposition of the core level into its components. Comparing all the core levels in Fig. 3.3 shows that the spectra on the irradiated sample measured at 8 keV is likely to be associated mainly to a single spin-orbit splitted component which should be the one of bulk Si, due to the extreme bulk sensitivity of the photon energy here. The first fitting of the Si 2p with a single bulk component B is shown in Fig. 3.5(a). We have thus fitted the bulk component of core level with spin-splitted doublets of Voigt functions to fit this experimental spectra with 0.36 eV Gaussian width and 0.15 eV of Lorentzian width, a spin-orbit splitting of 0.6 eV, and a branching ratio of 0.5 [98]. All the final fitting parameters are shown in Table 3.2 and 3.3. After identifying this main component, there are still some parts remained to be fitted. It is necessary to add the additional minor components, which are related to Si-H bonds, as well as the dangling bonds.

The B component describes roughly the line-shape of the Si 2p core level at 8 keV. However, there are poorly described regions marked in red. We thus added the components associated to the Si bonded with other element and known to present on the surface, i.e. dangling bonds, hydrogenated Si and oxidized silicon. The next component in intensity appears at lower binding energies, i.e. at the right in Fig. 3.5(b). Dangling bonds appear precisely here

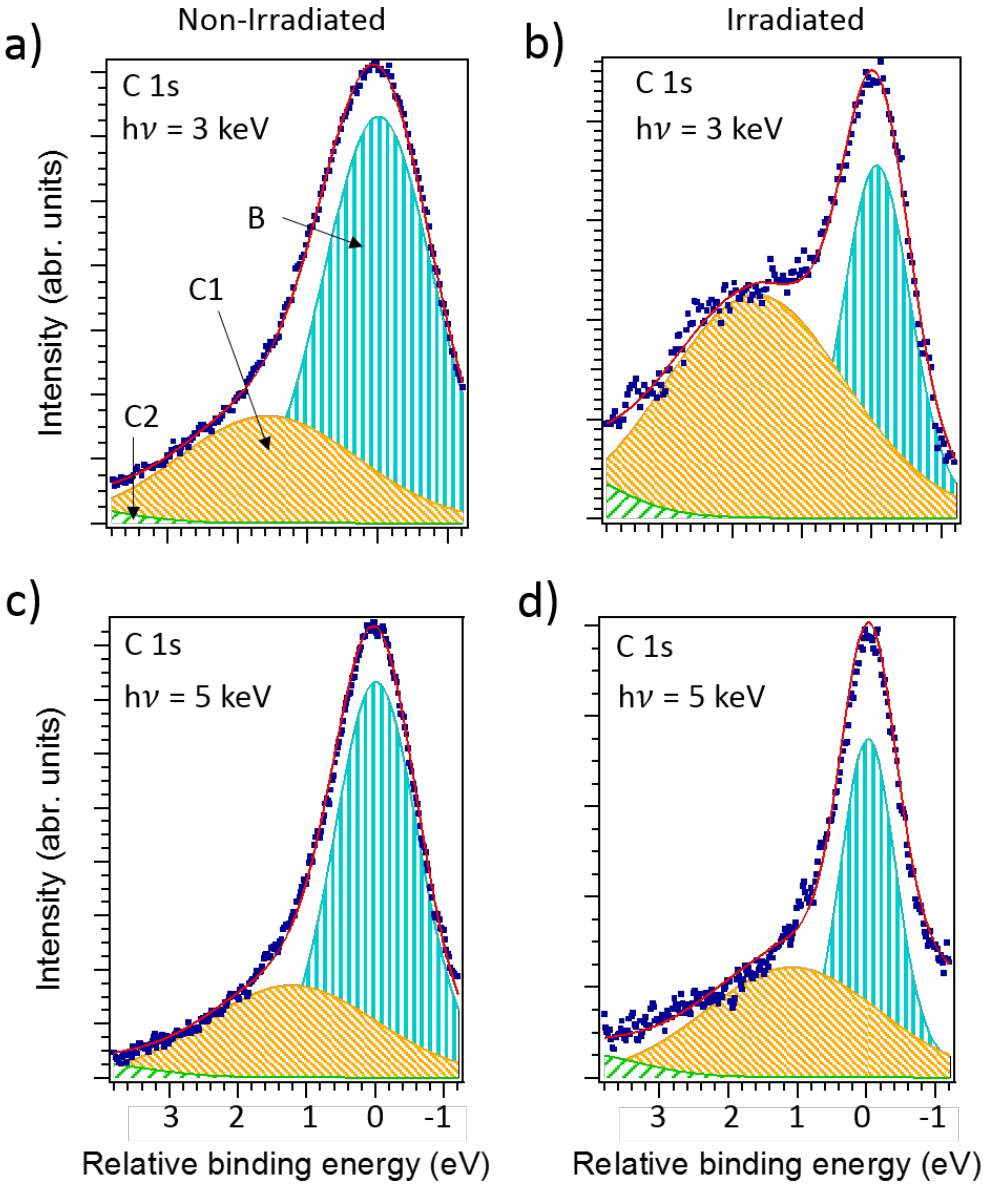

Figure 3.4: C 1s Core level decomposition for irradiated and non-irradiated heterostructures, as a function of the photon energies (3 keV and 5 keV). The binding energy is relative to the binding energy of the bulk component (283.0 eV).

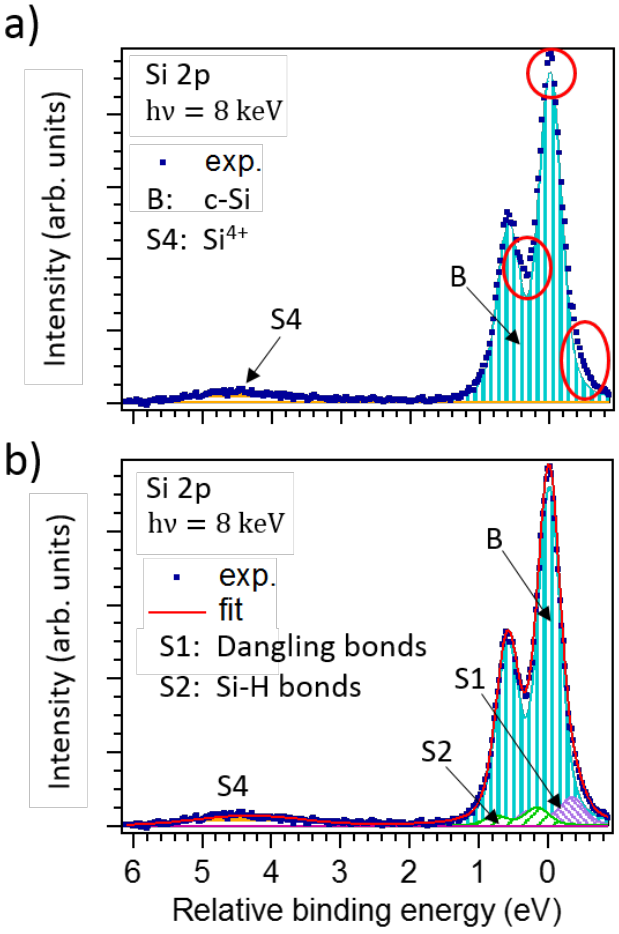

Figure 3.5: (a) Core level fitting of Si 2p from an irradiated sample at 8 keV of photon energy. Dark blue shows the bulk component with the two spin-orbit splitted peaks (Si $2p_{3/2}$ and Si $2p_{1/2}$) appearing at binding energies of 99.4 eV (set as the reference: 0 eV) and 99.9 eV (0.5 eV relatively). The orange component associated to Si^{4+} (SiO_2). Red circles highlight the spectra regions that are not satisfactorily described with a single component. (b) The final core level fitting of Si 2p with two additional components, which are S1, with the $2p_{3/2}$ peak located at ˜ 0.3 eV below of the bulk component, and the S2, with the center of the $2p_{3/2}$ located at 0.2 ˜ 0.4 eV above the bulk component.

Component	Binding energy
Si 2p (eV)	99.4
S1: dangling bond (eV)	99.1
S2: Si-H bond (eV)	99.7
S3: Si-C bond (eV)	100.0
S4: Si^{4+} bond (eV)	103.6

Table 3.3: Absolute binding energy for Si 2p, S1(dangling bond), S2 (Si-H), S3 (Si-C), S4 (Si^{4+}).

[99], so we introduced a component S1 with a chemical shift of around -0.3 eV with respect to the elemental silicon. In order to explain the badly fitted regions at high binding energies, we introduced a component S2 associated to Si-H, whose binding energy is known to appear around 0.2 to 0.4 eV higher than the elemental silicon [99, 100]. With these components plus the S4 component associated to Si^{4+}, the core level at 8 keV is satisfactorily described, as shown in Fig. 3.5(b).

Once the spectra at 8 keV of photon energy properly adjusted, we applied the same decomposition to the other spectra by varying the intensities of the different components. For the spectra at 5 keV, mainly sensitive to the a-SiC:H layer, a new component S3 is necessary, which is precisely associated to the Si-C bonds present in this layer [101]. We have further evidence that this component is associated to the a-Si:C:H layer. Fig. 3.6(a) shows the Si 2p spectra of an sputtered sample measured at 800 eV. This photon energy does not allow to probe the a-SiC:H layer and the S3 component is definitely absent. However, the S3 component appears in the spectra at 3 keV upon irradiation (Fig. 3.6(b)). This could be eventually related to the carbon diffusion toward a-Si:H layer (shallowed layer) during the irradiation process. With these 4 components, all the Si 2p core levels could be satisfactorily fitted. The fitting parameters are shown in Tables 3.2 and 3.4.

The resulting decomposition is shown in Fig. 3.7, in which the core levels are normalized with the total integral of Si 2p core level. Component B, associated to bulk Si^0 atoms, increases at the highest probing photon energy we used (8 keV) as expected. As for the surface sensitive component S1, which is related to dangling bonds, if we compare by visual inspection its intensity, we observe that the amount of dangling bonds in a-Si:H layer increases after irradiation. We can try to estimate the variation in the number of dangling bonds by integrating the area of the different components.

Fig. 3.8 shows the evolution of the ratio of the integral of the dangling bond and Si-H bond components compared to the total integral of Si 2p core level as a function of the photon energy. This figure allows one a more precise analysis of the evolution of dangling

Component	$h\upsilon$ = 3 keV		$h\upsilon$ = 5 keV		$h\upsilon$ = 8 keV	
	Non-irradiated	Irradiated	Non-irradiated	Irradiated	Non-irradiated	Irradiated
S1: dangling bond (eV)	-0.30 ± 0.02	-0.30 ± 0.02	-0.31 ± 0.02	-0.31 ± 0.02	-0.29 ± 0.02	-0.29 ± 0.02
S2: Si-H bond (eV)	0.26 ± 0.02	0.26± 0.02	0.25 ± 0.02	0.26 ± 0.02	0.25 ± 0.02	0.25 ± 0.02
S3: Si-C bond (eV)	-	0.50 ± 0.02	0.50 ± 0.02	0.50 ± 0.02	-	-
S4: Si^{4+} bond (eV)	4.14 ± 0.05	4.16 ± 0.05	4.15 ± 0.05	4.19 ± 0.05	4.16 ± 0.05	4.16 ± 0.05

Table 3.4: Chemical shift for S1(dangling bond), S2 (Si-H), S3 (Si-C), and S4 (Si^{4+}) related to the bulk component B. These are the binding energy shifts fitting to our experimental core levels of Si 2p measured in different conditions. In general, dangling bond has a chemical shift around -0.3 eV, Si-H bond has a energy shift around 0.25 eV, Si-C bond has a chemical shift of 0.5 eV, and Si^{4+} has a chemical shift around 4.15 eV. The intensity of each peaks will be demonstrated in Fig. 3.8 later on.

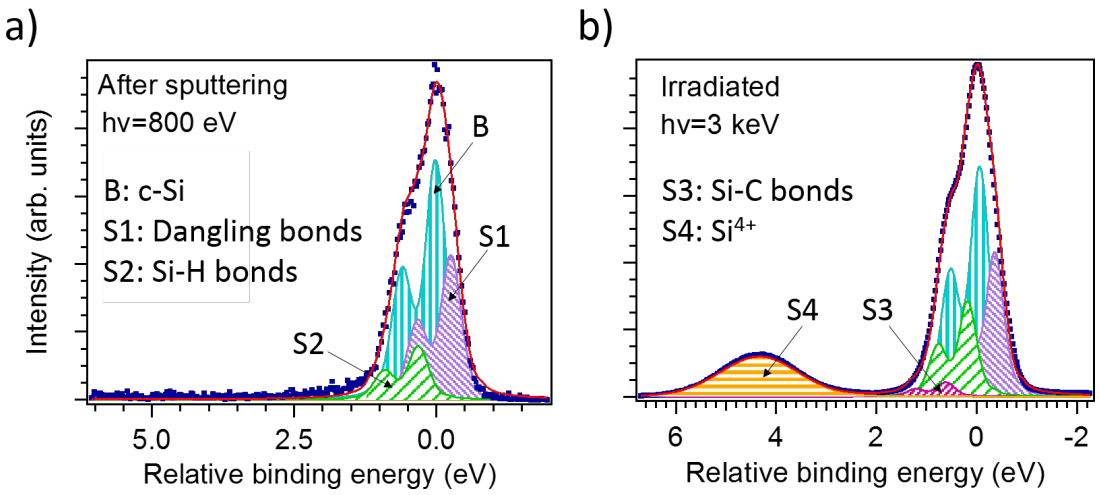

Figure 3.6: Si 2p core levels decomposition for (a) a sputtered heterostructure measured at 800 eV and (b) the Ar-irradiated heterostructure consisting of 7 nm a-Si:H and 3 nm a-SiC:H measured under 3 keV.

bonds versus Si-H bonds. The variation in the number of Si-H bonds can be studied through the component S2. These Si-H bonds are mainly located in the a-Si:H and a-SiC:H layer, as seen from the photon energy dependence of the component. Irradiation reduces the intensity of this component by $4 \pm 1\%$ in the Si 2p core level at both 3 keV and 5 keV. Most of the intensity lost in S2 was transferred to S1 (in the bulk) or S4 (at the surface), i.e. the hydrogenated bonds were broken and became dangling bonds that were bonded to oxygen at the surface. The contamination of SiO_2 has also increased by $7 \pm 1\%$ in the Si 2p core level close to the surface (at 3 keV). In addition, the treatment of irradiation can provide the energy and rearrange the structure of a-Si to become more crystalline as reported in [102]. Thus, the amount of dangling bonds decrease even more, at the same time, the feature of the doublet of c-Si is more obvious upon irradiation at 8 keV.

Finally we comment on the intensity variation of the two other components. Component S3 associated to the Si-C bonds shows that there is the same amount associated to SiC before and after the irradiation in the a-SiC:H and almost no variation when we measure deeper or shallow layers. However, a small intensity of S3 includes the presence of a slight amount of Si-C bonds in the shallow layer (a-Si:H) after the irradiation. This could be related to the diffusion of carbon atoms to the surface upon irradiation.

In conclusion, irradiation breaks some of the existing Si-H bonds, simultaneously increasing the number of dangling bonds in the hydrogenated layers. In the following, we will correlate this observation to the electronic states in the sample.

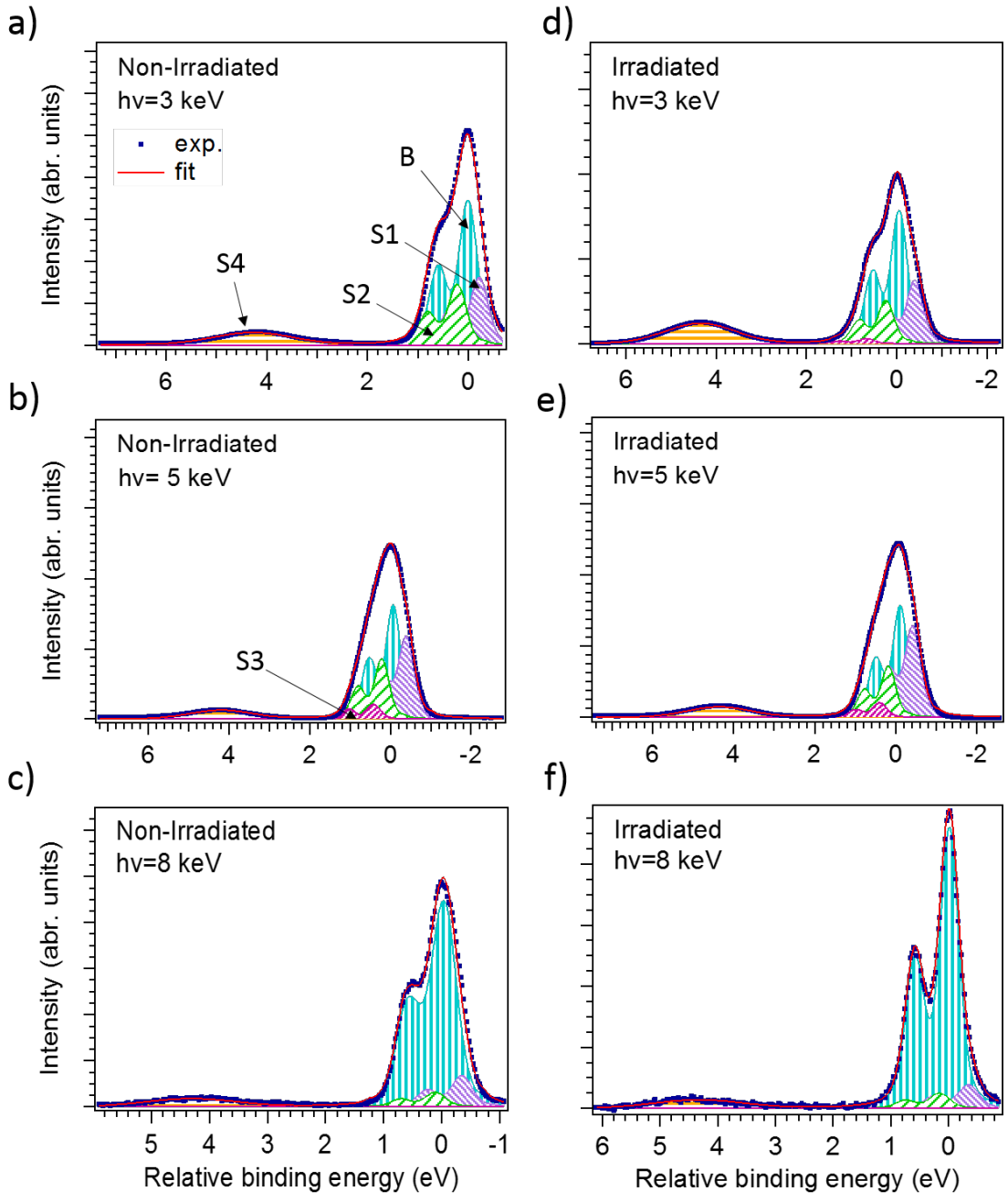

Figure 3.7: Si 2p core level decomposition for the non-irradiated and the irradiated heterostructures measured at photon energies 3 keV, 5 keV and 8 keV. Five components are necessary: a bulk component which is meanly from c-Si (B), a dangling bond component (S1), a Si-H bond component (S2), a Si-C component (S3), and a Si^{4+} component that is associated to SiO_2 (S4).

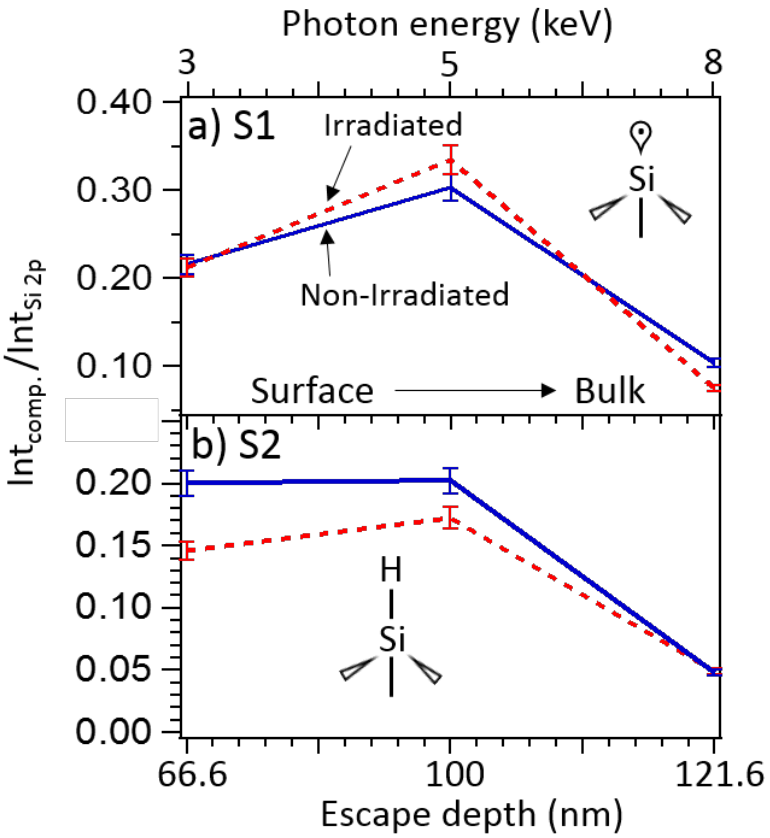

Figure 3.8: Intensity evolution as a function of the photon energy (shown in axis above) and the escape depth (shown in axis below) of (a) S1 component associated to dangling bonds and (b) S2 component associated to Si-H bonds.

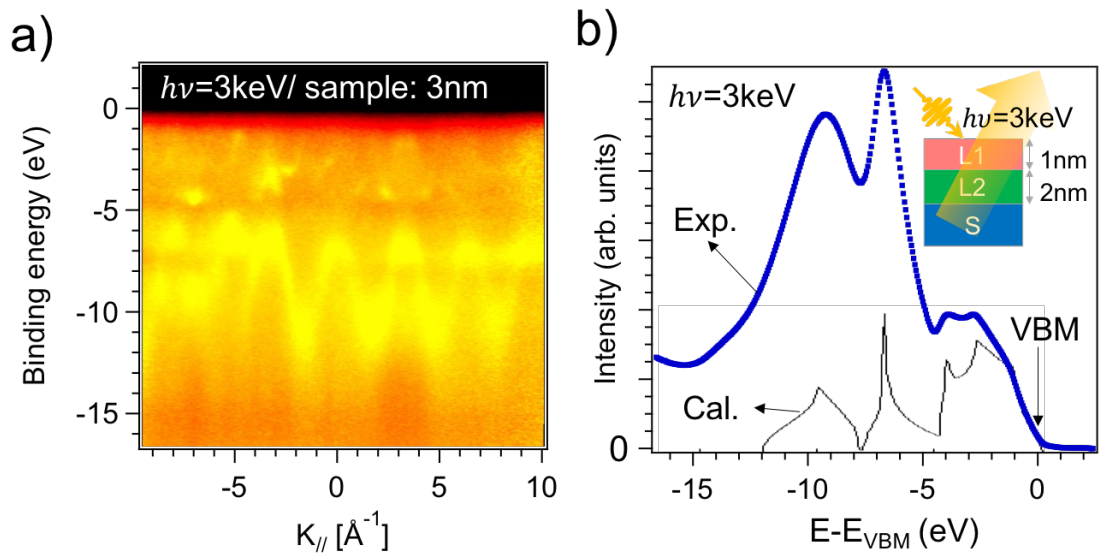

Figure 3.9: Electronic structure of 3 nm a-Si:H/ c-Si heterojunction sample (1 nm of a-Si:H and 2 nm of a-SiC:H) measured at 3 keV (a) valence band normalized to the density of states and (b) density of states.

3.5 Energy levels induced by defects in the band structure

The increasing number of dangling bonds has an influence on the electronic states, as we will see in the following. We have therefore studied the valence band of a-Si:H/ c-Si heterostructures. Fig. 3.9 shows the valence band from a 3nm thick a-Si:H heterojunction sample (1 nm a-Si:H + 2 nm SiC) on a c-Si substrate, as shown in the insert of Fig. 3.9(b). With the normalization of the raw data to the density of states, that contributes significantly due to the high photon energy photoemission [103], the band structure can be clearly observed. The experimental and the calculated DOS are plotted together in Fig. 3.9(b). Their comparison allows to identify the major spectral features in the experimental spectrum, i.e. the peaks around -8 eV and -10 eV, which correspond to the states with s+p and s character of c-Si. The density of states allows also to identify the valence band maximum (VBM), which will be our energy reference in the following.

We will now focus on the realistic case of heterojunctions for photovoltaic applications. Fig. 3.10 shows the integrated valence band, that emulates the DOS, from a 10 nm a-Si:H deposited on a c-Si substrate (8 nm of a-Si:H and 2 nm of SiC, see the insert in Fig. 3.10) for two different photon energies. If the spectra for irradiated and non-irradiated heterostructures are compared by normalizing them to have the same intensity for the minimum parts in the DOS of the valence band, it can be appreciated that the spectral weight near the maximum of the valence band of the irradiated heterostructures is always greater than in the non-irradiated

ones. This intensity is associated to the dangling bonds. By estimating the difference in integral of the pink region, we obtain the increase of the defect states upon irradiation. It corresponds to an increase of around $29 \pm 5\%$ at 3 keV and around $23 \pm 5\%$ at 5 keV. The large error bar is due to the normalization process to compare the spectra. The quantification of the electronic levels associated to the defect states agrees quite well with our previous quantification of the defect variation from core level spectra, which is about 25% of decrease of the Si-H bonds.

These gap states are located inside the gap, as they are above the valence band maximum by 0.3 eV (Fig. 3.10). Our photoemission study allows to identify some states above the maximum of the valence band, which are not enough to explain the 1.2 eV optical transition observed in photoluminescence (Fig. 3.1) [39]. We thus suspect the presence of defect states 0.2 eV below the conduction band minimum. These states allow therefore to explain the previous photoluminescence studies on those heterostructures that showed a transition of 1.2 eV within the 1.7 eV gap of a-Si:H [24].

3.6 Conclusions

In this chapter, we have studied the effects of defects introduced by Ar irradiation in a-Si:H/ c-Si heterojunctions, in order to improve the efficiency of heterojunction solar cells. We have studied the system by HAXPES, to analyze both the structure by core level spectroscopy and the electronic properties by valence band spectroscopy. From core level spectroscopy, we found out that after irradiation, the amount of Si-H bonds decreases the Si-H bonds decrease by $20 \pm 5\%$ in a-Si:H layer upon irradiation and become dangling bonds that some were bonded to oxygen at the surface.

From the valence band study, we observed the defect states after irradiation. These states are mainly associated to the dangling bonds in the a-Si:H layer. These defect states increase about $25 \pm 8\%$. The intensity of the additional states agrees quite well with the increase amount of dangling bonds according to the core levels after the irradiation.

The resulting energy diagram picture is shown in Fig. 3.11. Our photoemission study allows to identify some states above the maximum of the valence band, which are not enough to explain the 1.2 eV optical transition observed in photoluminescence. We thus suspect the presence of defect states 0.2 eV below the conduction band minimum. This picture allows to explain the photoluminescence results. The study of these states near the conduction band minimum by inverse photoemission as well as to study annealed heterostructures where the states are healed are perspectives of this study.

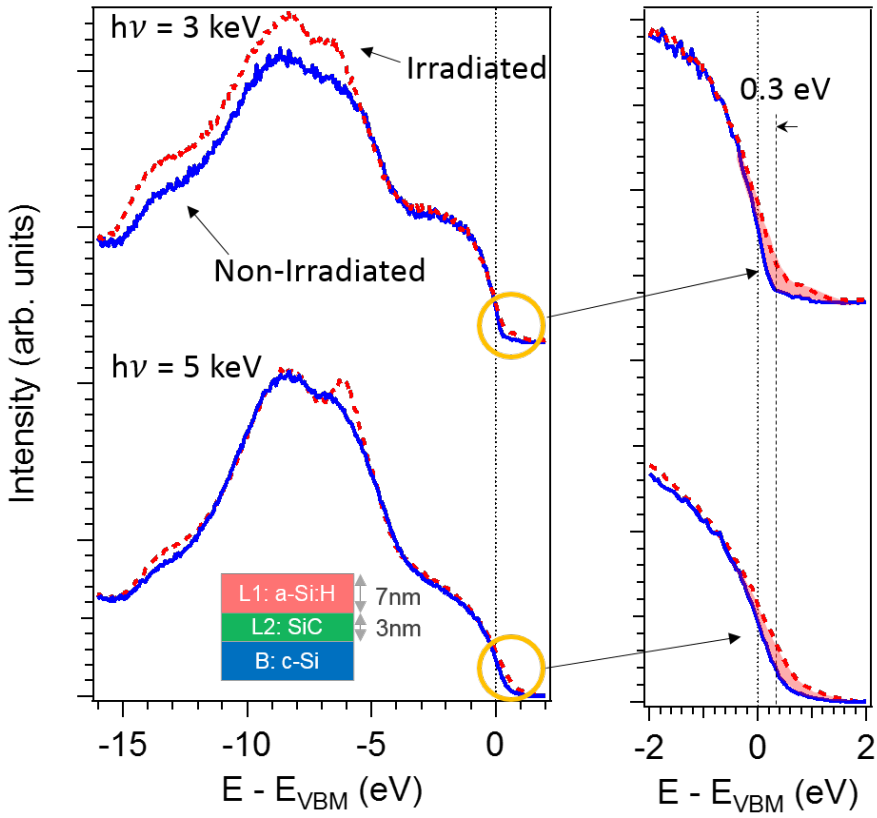

Figure 3.10: Comparison the experimental DOS between irradiated (red curve) and non-irradiated (blue curve) heterostructures on the 10nm a-Si:H heterojunction sample (see the insert). The left panel shows the whole valence band, and the right panel shows the zoom close to the VBM. The defect states, located at 0.3 eV above valence band maximum are filled in pink.

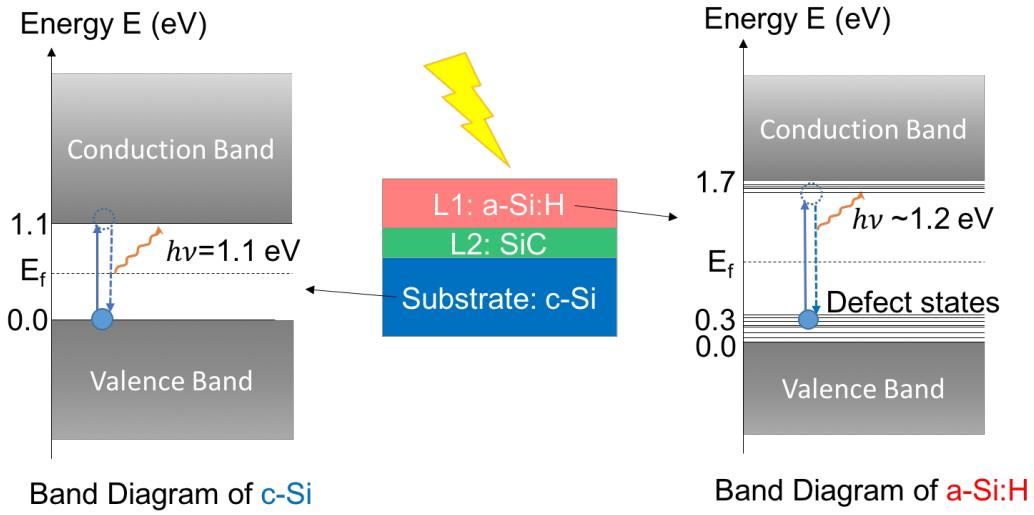

Figure 3.11: The mechanism of the photoluminescence presented by band diagrams of c-Si and a-Si:H represented with the defect states.

Part III

Hybrid organic/ inorganic perovskites

Chapter 4

Valence and conduction bands of $(C_6H_5C_2H_4NH_3)_2PbI_4$

4.1 Introduction

Two dimensional (2D) hybrid perovskites, traditionally used for optoelectronic devices [9, 10, 11], have recently attracted attention for solar cells because of their enhanced moisture and photo-stability compared to 3D perovskites [12].

In addition to the stability issue, they have also fundamental properties useful for the solar cell operation. In general, 2D layered perovskites have larger band gaps than 3D perovskites. For instance, the most common 2D perovskite, i.e. $(C_6H_5C_2H_4NH_3)_2PbI_4$, phenylethylammonium lead iodine (PEPI) has a band gap about 2.6 eV while the 3D prototype MAPI has 1.6 eV. As a result, an electronic quantum confinement are expected in 2D perovskite. Therefore, a mixture of 2D-3D perovskites structure is studied to prevent this electronic barrier, and at the same time, increases the stability of the solar cells [104, 105]. From the previous optimizations of the 2D-3D perovskite solar cells, the efficiencies of these solar cells have grown quickly from 4.73% in 2014 [106] to 12.52% in 2016 [107]. Although these figures are smaller than in 3D solar cells, the higher stability of 2D-3D perovskite solar cells is a key factor for a potential success in commercial applications.

4.1.1 Spin-orbit coupling impact on the electronic band structure

Light absorption is strongly dependent on the detailed band structure of the materials and on the amplitude of the band gap. As we saw in Fig. 1.12, the band structure with and without spin orbit coupling for 4F-PEPI ($(pFC_8H_{12}N^+)_2(PbI_4{}^{2-})$) changes strongly. The spin-orbit coupling (SOC) has an extraordinary impact on the band gap amplitude, since it affects strongly the bottom of the conduction band. This importance of the SOC is a

general feature of hybrid perovskites due to the presence of heavy atoms as lead, with strong relativistic effects. The determination of the gap by density functional theory is tricky since it underestimates the gap. The lack of the experimental electronic bands is thus a drawback to further understand this material and optimize the efficiency in solar cells.

In this chapter, we will study the 2D perovskite PEPI. We will present the first experimental k-resolved valence and conduction band structure by angle-resolved photoemission spectroscopy (ARPES) and inverse photoemission spectroscopy (IPES). These experimental data have been compared to fully relativistic calculations using the SPR-KKR code.

4.2 Experimental band structure determination and simulations

As these spectroscopies are surface sensitive techniques, we need to illuminate an ideal surface representative of the bulk. Once this is achieved, we studied experimentally the valence and the conduction bands. Both experiments were then simulated.

The bands in two-dimensional systems as PEPI disperse with $k_{//}$, namely k_x and k_y, as shown in Fig. 4.1(a). Measurements with a two dimensional detector make vertical slices of this three-dimensional matrix. A vertical slice allows to obtain the whole band structure. These constant energy cuts at different energies can also be obtained. In order to measure the whole electronic structure, both photoemission (PES) and inversion photoemission (IPES) have been used (Fig. 4.1(b)).

4.2.1 Surface cleaning

Solar cells usually use thin films. We thus started our studies on thin films of PEPI, shown in a scanning electron microscopy image in Fig. 4.2(a). The usual method to clean such a sample for photoemission measurements is to anneal the sample to remove surface contamination. In order to determine the annealing temperature that cleans the sample, we annealed progressively the sample while doing Auger electron spectroscopy (Fig. 4.2(b)). Before annealing, the spectra shows strong peaks of carbon and oxygen. No lead peak is visible because it is hidden by the contamination. Annealing at 100 °C allows to observe a tiny peak of lead. However, oxygen, which is not an element present in PEPI, is still very high. Upon increasing the annealing temperature to 150°C, the lead peaks decreases. Annealing above 400°C cleans the sample, as the oxygen peak disappears, but so does lead. The sample cannot therefore be cleaned without destroying it.

An alternative way to obtain clean samples consists of cleaving a bulk crystal (Fig. 4.3(a)) under ultra-high vacuum. Cleaving can be done by hitting a top-post (Fig. 4.3(b)) glued to the sample. Cleaving is easy due to the two dimensional nature of the sample, especially if

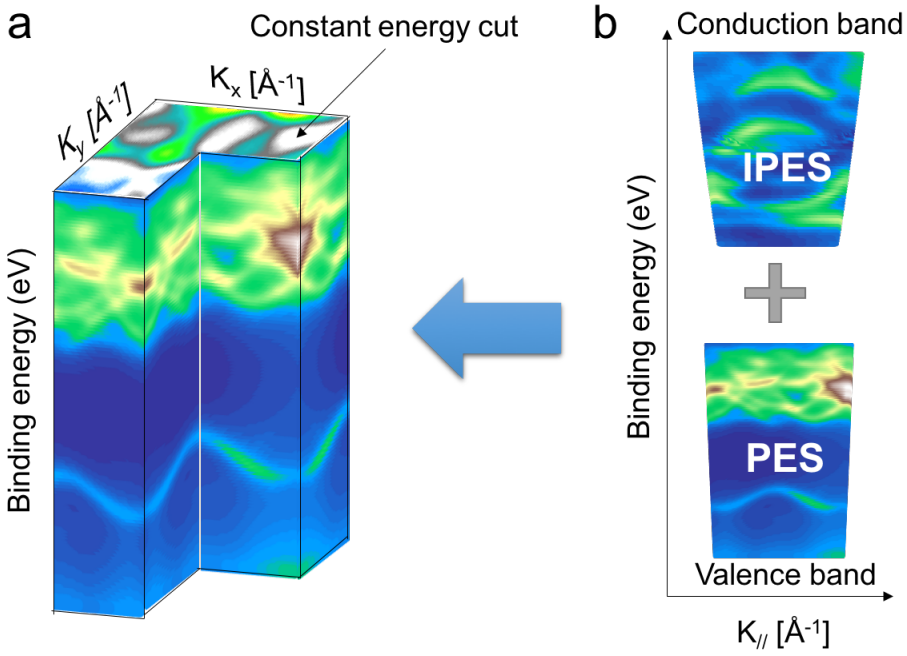

Figure 4.1: (a) A schematic of the whole simulated band structure. Vertical slices provide the dispersion vs $k_{||}$. Horizontal slices provide constant energy cuts. (b) IPES and PES experimental techniques allow to obtain both conduction and valence bands.

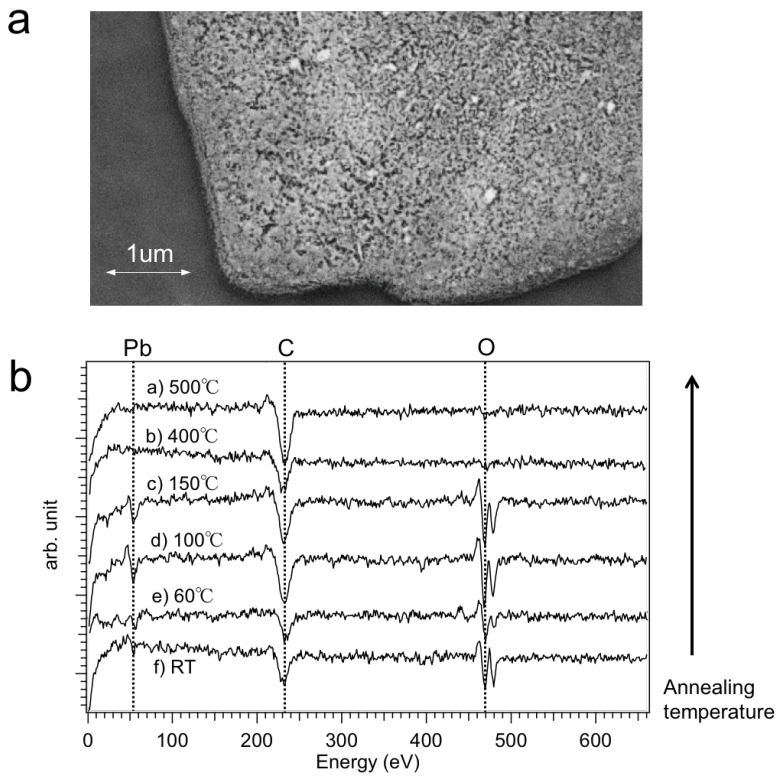

Figure 4.2: (a) Scanning electron microscope image of a thin film of 4F-PEPI. (b) Auger spectra of 4F-PEPI thin films after annealing at different temperatures.

the sample is a single crystal with all the molecular planes aligned in a macroscopic region. A nice rectangle shape of PEPI seen by naked eye also shows the high quality of our single crystal. Besides this evident crystallographic check, we performed X-ray diffraction to verify the crystallinity of the samples, because the experimental band structure determination requires single crystals. Otherwise, only the density of states is obtained due to averaging on randomly oriented crystallites. In our work, we used single crystals of millimetric size (Fig. 4.3(a)). We performed X-ray diffraction to check the crystallinity. Fig. 4.4(a) shows the (h0l) plane at room temperature. The absence of rings surrounding the Bragg reflections demonstrate the absence of polycrystals in our samples. The structural refinement has also allowed to compare with other preparations in the literature and to obtain the detailed atomic structure as an input for theoretical calculations. The refined structure is shown in Fig. 4.4(b).

After cleaving the sample, we obtained a large-range photoemission spectrum at a photon energy of 130 eV, which allows to observe different the core levels of the main elements in the sample as well as the valence band (Fig. 4.5(a)). In a second step, we checked the radiation damage at 130 eV. The blue solid curve in Fig. 4.5(a) shows the spectrum after 18 hours of irradiation. Comparing these two spectra, after the irradiation, the spectrum in blue becomes

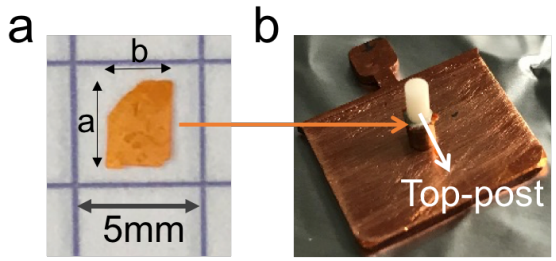

Figure 4.3: (a) A single crystal of PEPI, with a size of about 2.5 mm by 3 mm. (b) Sample mounted on a sample holder with a top post attached, which is used to cleave the sample in ultra-high vacuum.

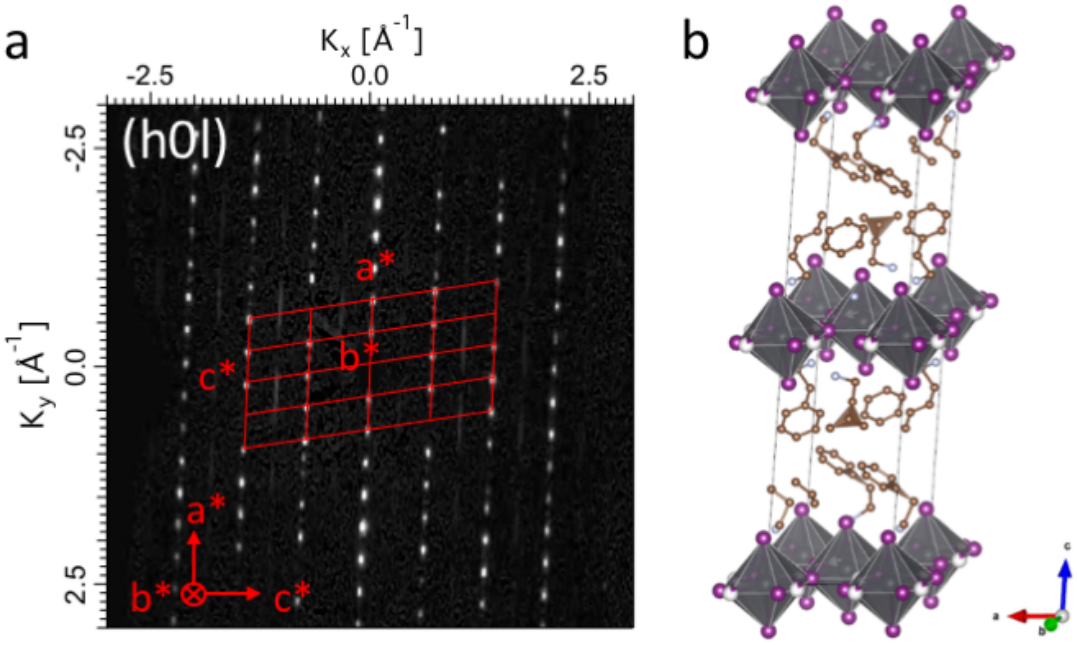

Figure 4.4: (a) (h0l) plane of the reciprocal space of PEPI measured at room temperature by X-ray diffraction, indicating the projection of the reciprocal unit cells (in red). (b) Refined structure.

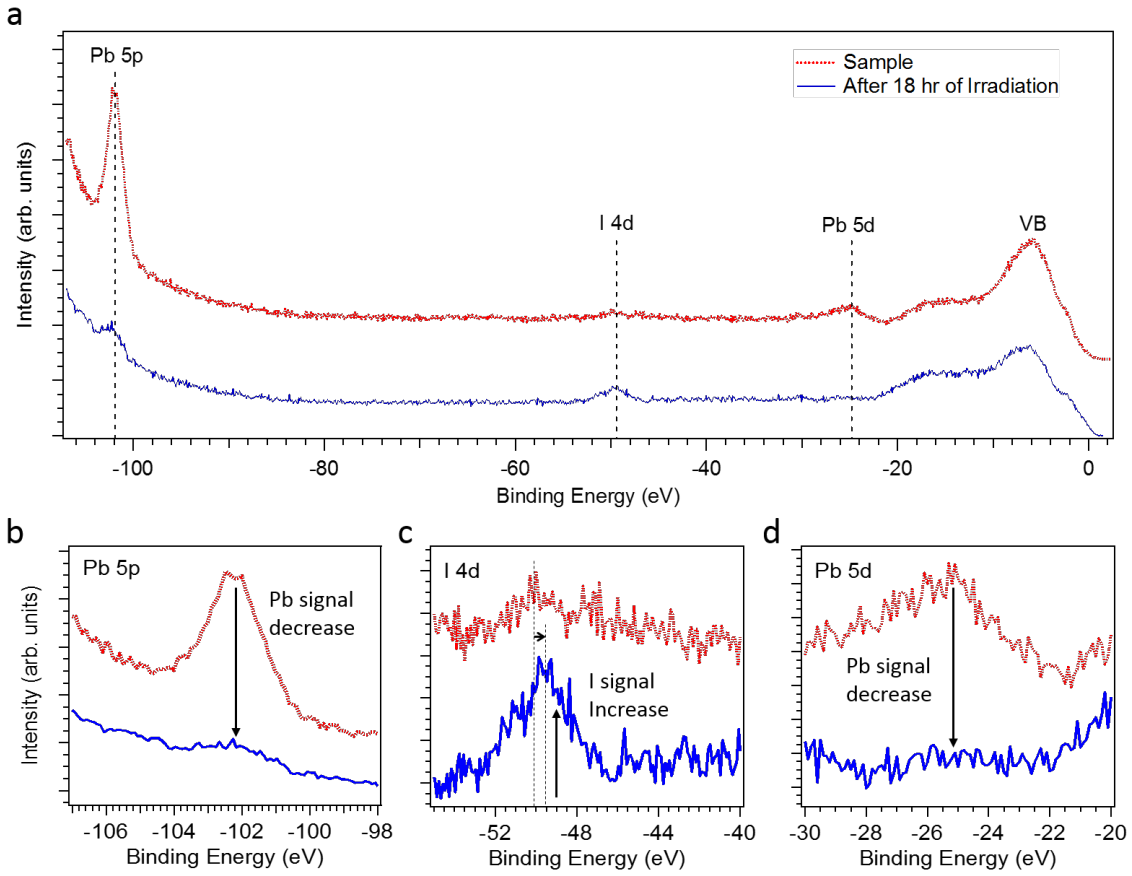

Figure 4.5: (a) Spectrum of photoemission on PEPI before and after irradiation during 18 hours under 130 eV photons. Core levels of (b) Pb 5p, (c) I 4d, and (d) Pb 5d.

featureless, which could be due to the degradation of the sample. The intensity of Pb and I peaks is better appreciated in the dedicated panels below (Fig. 4.5(b) - (d)). It can be observed that the Pb signal almost disappears upon irradiation, while the peak of I increases, possibly because of PEPI degradation into PbI_2. After this irradiation test, we reduced considerably the beam resolution from 10 meV to 5 meV in order to minimize the effects of radiation damage. We have figured out a better condition to perform the experiments is obtained by reducing the intensity of the beam (from 500 mA of uniform beam to 16 mA of 1 package beam) and shorten the duration of our measurement. Further experiments will be shown in section 4.2.4.

4.2.2 Impact of the organic molecule in the electronic structure

In order to better understand the system, we will compare our experiments to photoemission simulations with the SPRKKR method. Due to the large number of atoms in the unit

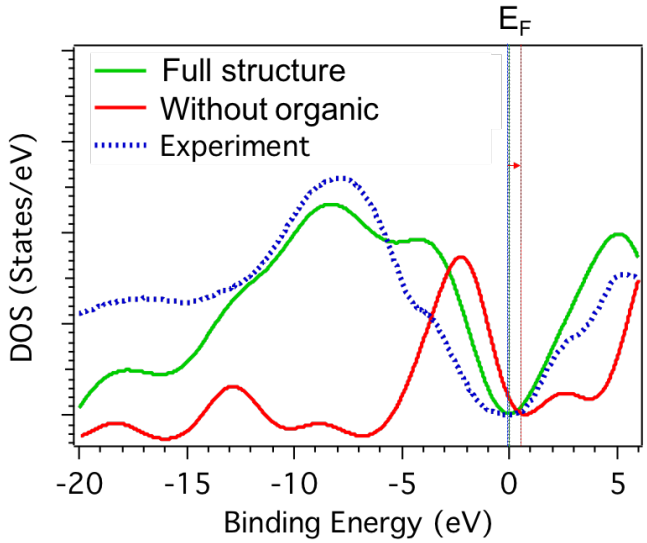

Figure 4.6: Density of states (DOS) of PEPI. Blue-dotted line shows the experimental DOS, green-solid line shows the calculations including the full structure, and the red-solid line shows the calculations without the organic molecules. Calculations here include a Gaussian broadening to compare to the experimental data.

cell, the calculations are beyond current computation resources. Since molecular states do not contribute to dispersive features, we will perform SPRKKR calculations without taking phenylethylammonium $(C_6H_5C_2H_4NH_3)_2$ into account, i.e. just with the inorganic part PbI_4. Before doing this approximation for the photoemission simulations, we checked its accuracy by comparing our simplified SPRKKR calculations using full calculations with Wien2k by Jan Minar and Saleem Khan from University of West Bohemia at Plzeň in Czech Republic.

The experimental and the computed density of states (DOS) for valence and conduction bands are shown in Fig. 4.6. Organic molecules displace the Fermi level towards positive binding energies and add carbon and nitrogen states between -4 and -12 eV. From the comparison of experimental and theoretical DOS, theoretically, it can be observed that, in the case without taking organic part into account, the energies should be slightly shifted (around 0.5 eV) above the Fermi level and slightly normalized each of their binding energy to compare to the experiment.

More details can be found in the calculated band structure. Fig. 4.7(a) shows the bands from the whole structure in red and the part from the inorganic PbI_4 in blue. Most of the dispersion in red are overlapping by the slightly renormalized ($\pm$0.5 eV) blue band structures. The differences between the blue and red bands are shown in Fig. 4.7(b), i.e. the organic states. It shows that organic molecules induce many non-dispersing states in the system. The dispersion is thus mainly arising from the inorganic part (Fig. 4.7(a) blue bands). Therefore, if we exclude the organic structure to simulate the photoemission data by SPRKKR, no impact

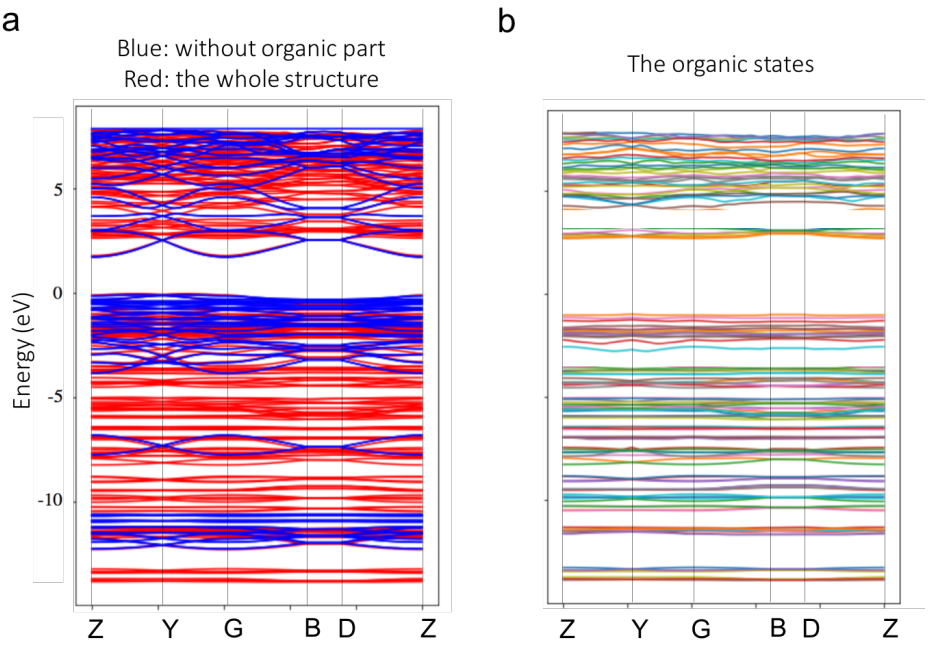

Figure 4.7: Theoretical band structure of PEPI, by including a (a) full structure (red) and the structure without organic molecules (blue). (b) The difference of the states in between red and blue calculations, i.e. the organic states. Calculations were performed with Wien2k.

is expected in the dispersing features. We will just need to be aware of the shift in binding energy that we observed in the DOS analysis and some slightly different renormalization of the binding energies for some bands. It can be observed that there is no dispersion along the BD high symmetry direction, which corresponds to the stacking axis of the two-dimensional layers. The dispersion absence indicates the two dimensional behavior of PEPI [36].

4.2.3 Impact of the spin-orbit coupling in the electronic structure

The spin character of the bands has an impact on solar cell efficiency in two ways. First, the SOC splitting will modify the gap amplitude if it takes place at the VBM and/or CBM. Second, spin polarized bands may impact the electron de-excitation, promoting longer lifetime as it has been evoked for hybrid perovskites [108]. We will therefore evaluate the impact of SOC by SPRKKR calculations.

Fig. 4.8 shows the DOS calculated by SPRKKR with and without applying SOC. Both cases have the same overall shape although with different intensities and some energy shifts in the features. The most important difference is the band gap size. Without SOC the band gap is larger due to the slightly shifted states at VBM and CBM. For more details, we need to compare with the k-resolved band structure, shown in Fig. 4.9. In the valence band, some of the bands appear slightly shifted in binding energy (less than 0.2 eV). The difference in the

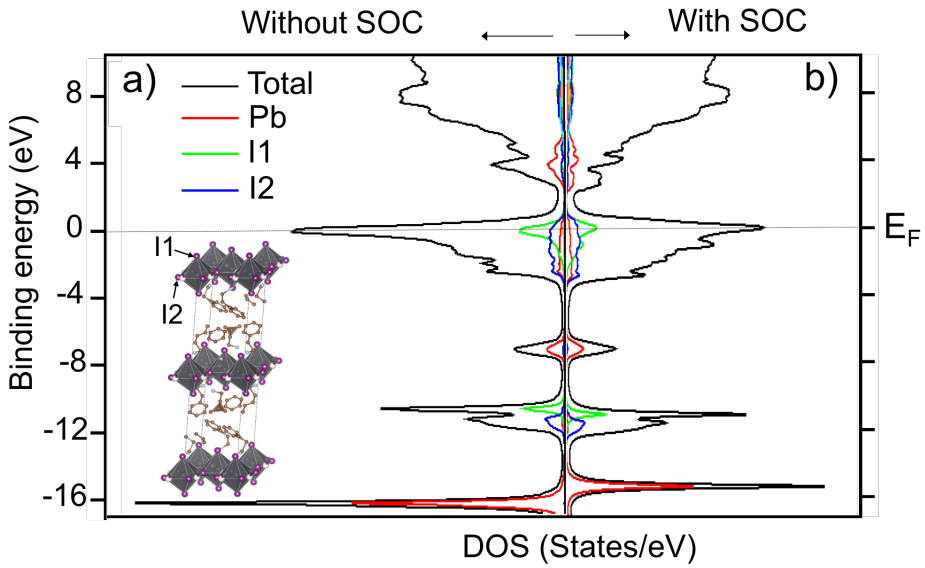

Figure 4.8: DOS of PEPI using (a) scalar relativistic (without SOC) and (b) fully relativistic (with SOC).

dispersions are however tiny. On the contrary, in the conduction band, the band structures shift 0.6 eV towards higher binding energies. The band gap is therefore very different in the two calculations, 1.55 eV and 2.2 eV, with and without the SOC, respectively. These calculations give the trend of the band gap variation when including SOC, even if the precise value is not accurate in SPRKKR calculations (due to the absence of the organic molecules as discussed in Fig. 4.6).

4.2.4 Experimental and calculated valence band

We have performed measurements of the valence band in several Brillouin zones. The sample was initially pre-oriented on the sample holder by a proper alignment of the macroscopic facets of the crystal. In a second step, we performed a precise orientation by looking at the constant energy cut close to the valence band maximum (Fig. 4.10).

The constant energy cut allows to determine the spectrum periodicity. The periodicity between the high intensity spots is 0.7 $Å^{-1}$ which is associated to the lattice parameter a (8.984 Å). This allows to correlate the macroscopic orientation of the crystal in Fig. 4.3(a) within the crystallographic directions. Therefore, the BZ corresponds to the red doted lines. We can now compare to the theoretical constant energy cut.

Once the sample is precisely oriented, we can obtain the dispersion along all the high symmetry directions. The valence band along ΓYΓ is shown in Fig. 4.11(a). There are some dispersive features hidden by the broadness of the spectral features associated to the

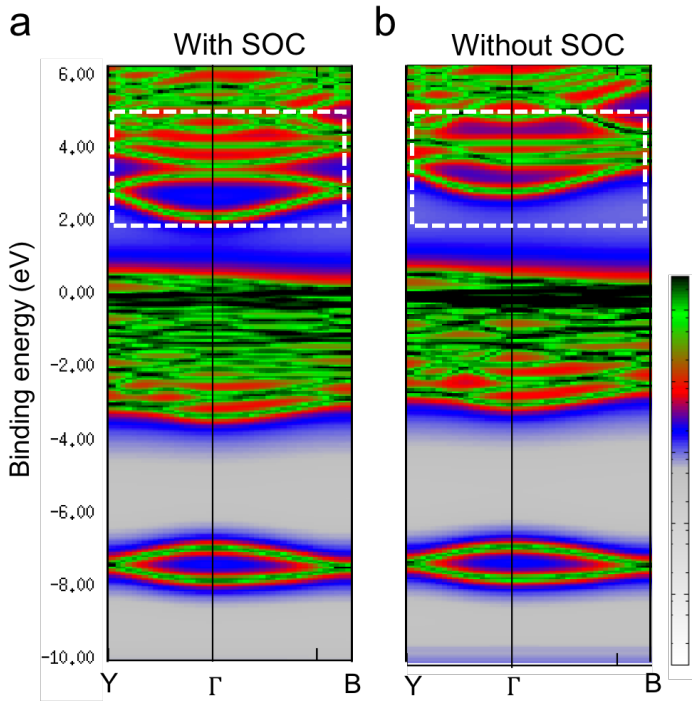

Figure 4.9: Theoretical band structure calculation of PEPI without organic molecules using SPRKKR code (a) with and (b) without SOC. The biggest differences are highlighted by the white rectangle.

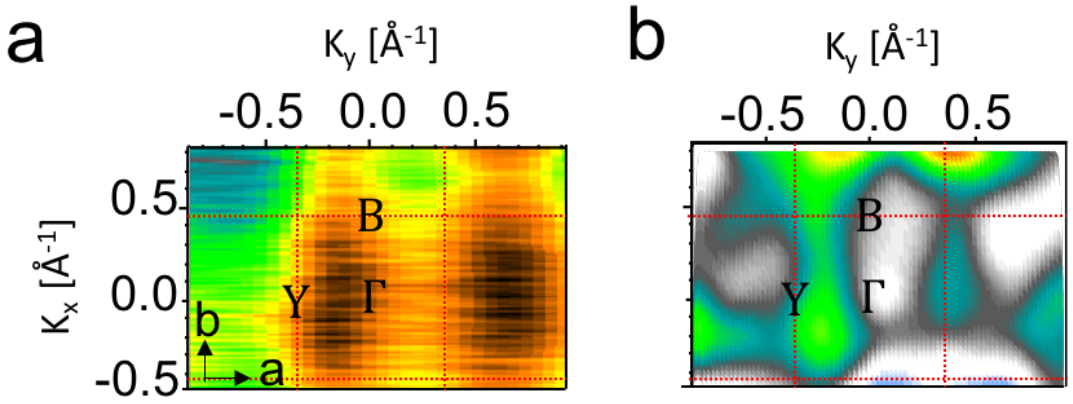

Figure 4.10: (a) Constant energy cut of the valence band of PEPI at -0.5 eV below the maximum of the binding energy (VBM). (b) The calculated spectrum, the energy is of -0.5 eV below the VBM. The Brillouin zone of PEPI is shown as red doted rectangles.

organic molecules. For instance, there is a broad band located between -5 eV and -10 eV, also shown in the angle-integrated spectrum (Fig. 4.11(a), right). A 2D curvature analysis, which is based on the concept of curvature and improves the reliability and sharpness of the spectral features over the second derivative method, of the photoemission intensity [109] (Fig. 4.11(b)) allows to observe some dispersive features between -3 eV and -7eV, which correspond to some theoretical bands (Fig. 4.11(f)). Another treatment to see dispersing features consists in normalizing by the "angle-integrated spectrum". In this way, we will minimize the contribution of dispersiveless features, as the molecular states, that are not included in our calculations. Such a normalization is shown in Fig. 4.11(c). After the normalization and the 2D curvature, dispersions close to the maximum of the valence band become clear (Fig. 4.11(d)). When compared to the theoretical calculations (Fig. 4.11(f)), the intensities show a nice agreement after normalizing with DOS, and applying curvature analysis. The overall flatter bands in our experiment indicate a possible renormalization of the bands.

4.2.5 Experimental and calculated conduction band

We can proceed in a similar way to analyze the conduction band measured by the IPES along the ΓBΓ direction (Fig. 4.12(a)). The dispersions are not explicit in the raw data. However, the normalization by the DOS and the 2D curvature analysis allow to obtain the dispersive features in Fig. 4.12(b). The theoretical band structure without organic molecules and considering SOC is superimposed. We reach a reasonable agreement with the theoretical calculation of IPES (Fig. 4.12(c)), although a strong energy shift seems to happen owing to the absence of the molecules in the simulation of IPES. The spectrum in Fig. 4.12(c) is shown after the shifting about 1 eV towards the Fermi level. Beside this energy shift, the biggest band dispersion appeared in the conduction band minimum (around 1.5 eV to 3 eV) is reproduced well in the simulation. In addition, the intensities present around 5 eV and 7.3 eV in our experiment data also agree nicely with the intensities values obtained in the simulation.

4.3 Conclusions

In this work, we have experimentally determined the valence band and the conduction band by ARPES and IPES measurements. By comparing to our theoretical calculations, we observe some agreement for the spectral features, although, in the valence band, the dispersions appear flatter in the experiment than on the calculations, indicating a higher effective mass in the real system. On the contrary, band dispersions for the conduction band are in good agreement, including the effective mass.

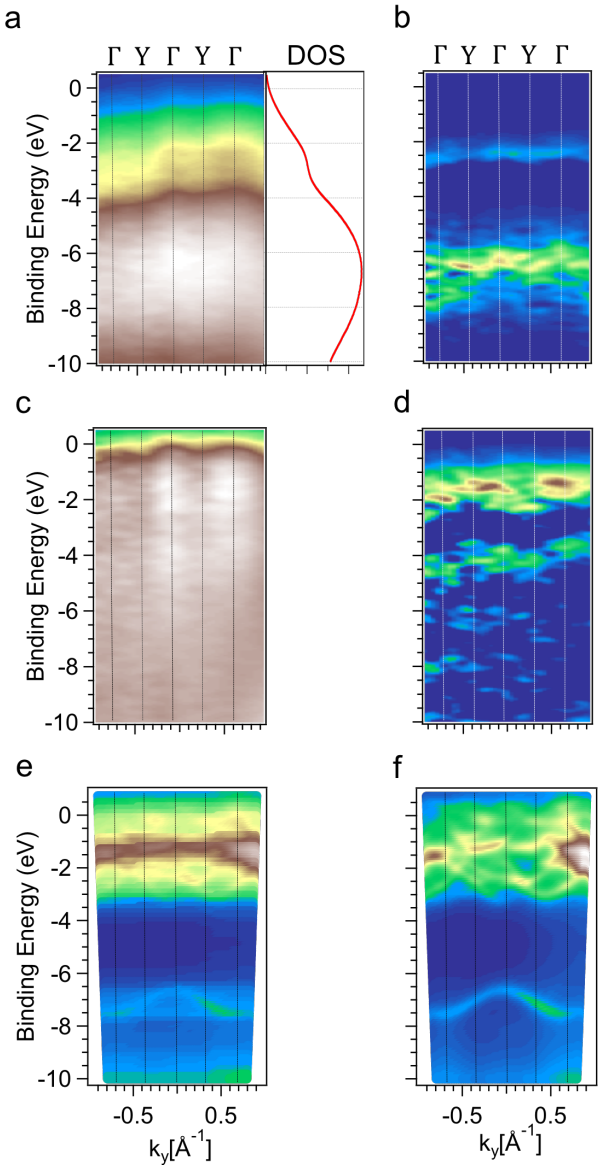

Figure 4.11: ΓYΓ valence band dispersion of PEPI. (a) Raw ARPES data, along with its integration in angle, simulating a density of states, and (b) 2D curvature analysis. (c) ARPES data normalized to the density of states to get rid of the non-dispersing states from organic molecules, and (d) 2D curvature analysis to it. (e) Theoretical simulation of ARPES data, including SOC in a structure without organic molecules, with its angle-integrated spectrum artificially added. (f) Theoretical simulation of ARPES data, in a structure without organic molecules and without adding the density of states.

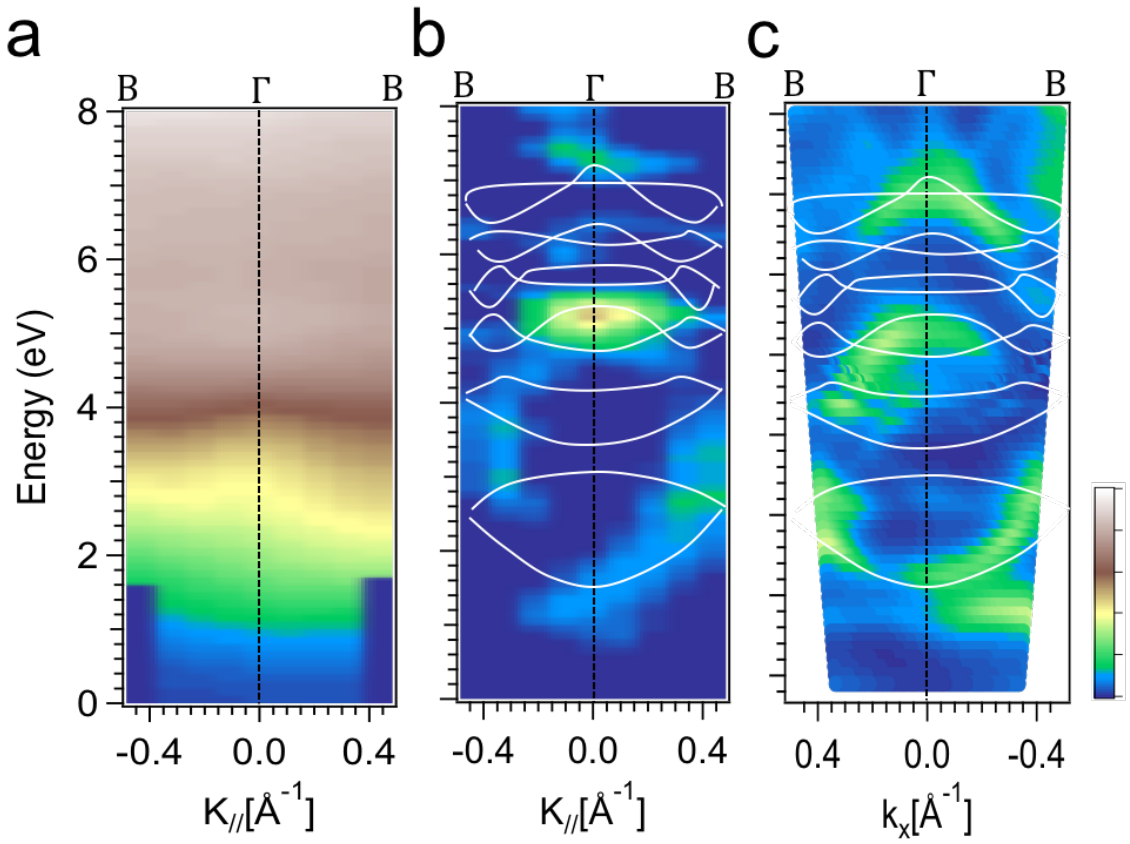

Figure 4.12: Conduction band of PEPI along ΓBΓ. (a) Raw IPES data. (b) IPES data normalized to the angle-integrated spectrum and with a 2D curvature analysis. The calculated ground-state bands superimposed. (c) Simulated IPES spectra including SOC in a structure without organic molecules (with SOC). The calculated ground-state bands are superimposed.

Chapter 5

Band structure and electronic relaxation of $CH_3NH_3PbI_3$

5.1 Introduction

Hybrid organic-inorganic perovskites have attracted considerable attention as an active layer for planar heterojunction solar cells owing to their strong light absorption along with the low cost fabrication process in solution[3, 4, 5]. The efficiency of these solar cells has increased dramatically. The three-dimensional perovskite methylammonium lead iodide ($CH_3NH_3PbI_3$, $MAPbI_3$, or MAPI), has in particular reached an efficiency exceeding 22% [6]. In addition to this, hybrid perovskites exhibit high carrier mobility, and excellent carrier diffusion lengths exceeding 1 μm [7, 8]. Due to these unique properties, once the stability issue in hybrid perovskites is solved, they could become competitive to silicon based solar cells.

Another key issue to improve the efficiency of any photovoltaic material is a thorough understanding of the electronic properties and electronic relaxation dynamics. However, hybrid organic-inorganic perovskites have been studied without an experimental determination of the band structure. The precise details of the band structure are extremely important to understand solar light absorption, as well as the charge carrier transport to the electrodes.

Theoretical calculations provide a first estimate of the band structure [110, 111, 112, 113, 114, 115, 36, 116, 117, 118, 119]. However, there is a considerable dispersion in the calculated parameters, as it can be observed for instance in the effective mass, m^* [113, 116, 120, 121], which controls the band flatness, the electronic localization, and the mobility inside the material. Among the calculations for m^* shown in Fig. 1.13 (section 1.3.2), the values for the same phase of the same compound can vary by a factor of two. An experimental determination is therefore necessary, which will result in a more precise modeling of the electronic structure and a better fundamental understanding of the system. A number of angle-integrated photoemission experiments have been performed [111, 122, 123, 124]. These

experiments provide useful information about the density of states, although much more information is contained in the band structure, which has not been measured yet.

In this chapter, we present the experimental determination of the valence band dispersion by angle-resolved photoemission spectroscopy. We will determine experimentally the effective mass, compare the experiment to photoemission simulations using the SPRKKR method and focus on the electronic transition taking place slightly above RT, i.e. in the operation range of solar cells.

After analyzing the band structure, we will study the early relaxation of the system after being excited by a photon. We will perform this study by two-photon photoemission spectroscopy in the femtosecond time scale. We will in particular analyze the carrier diffusion and the influence of defects on the charge carrier recombination and therefore on the efficiency.

5.2 Band structure determination and simulations

We have adopted for MAPI the same procedure that we used for determining the band structure of PEPI. The situation for MAPI is more complicated, since we are now dealing with a 3D system. We will therefore analyze first the $k_\perp$ dispersion of the band structure and the in-plane orientation of the Brillouin zone, that are necessary for the accurate measurement of the band structure and the comparison to the calculations. Finally, we will extract some conclusions concerning the periodicity of the photoemission spectral weight and the effective masses.

5.2.1 Three-dimensional band dispersion and cubic periodicity of the spectral weight

Being MAPI a three-dimensional (3D) system, we must take care when determining its electronic structure. Since the bands disperse with $k_\perp$, i.e. with the photon energy, as we have shown in Eq. 2.11 (section 2.3.1), it is first necessary to identify the photon energy $h\nu$ that allows to measure as a function of $k_{||}$ close to a high symmetry plane.

Thanks to synchrotron radiation, which provides a wide range of photon energies, 3D systems can be measured properly. Fig. 5.1 shows the band structure measured at several photon energies. It is observed the evolution of the electronic states when varying the photon energy (see arrows highlighting the change). Such an evolution corresponds to the electronic states dispersing with k perpendicular to the surface, as expected for a 3D material.

From a series of band dispersions as a function of the photon energy as those in Fig. 5.1, we can obtain constant energy cuts of the electronic structure as a function of k_x and k_y. Fig. 5.2(a) shows a constant energy cut of this data set, in which k_y corresponds to the dispersion perpendicular to the surface and k_x corresponds to a direction parallel to it. As the sample

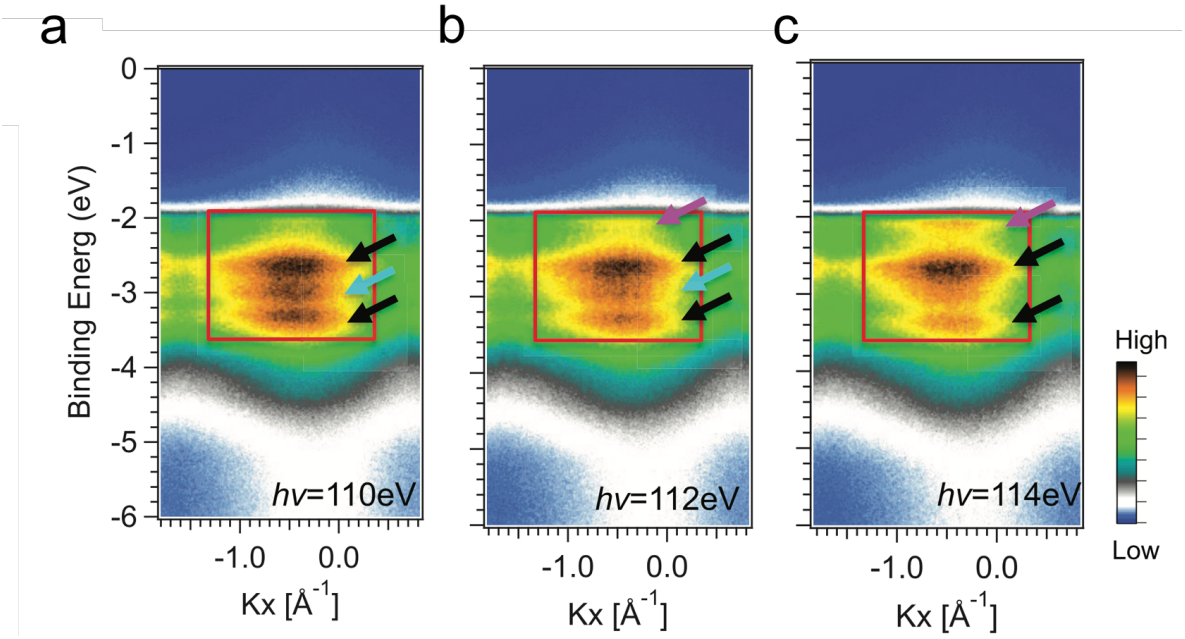

Figure 5.1: Electronic dispersion as a function of the photon energy. Photoemission measurements along a direction containing the normal emission for photon energies of (a) 110 eV, (b) 112 eV and (c) 114 eV. Arrows highlight the evolution of the electronic states. Such an evolution corresponds to electronic states dispersing with k perpendicular to the surface, as expected for a 3D material.

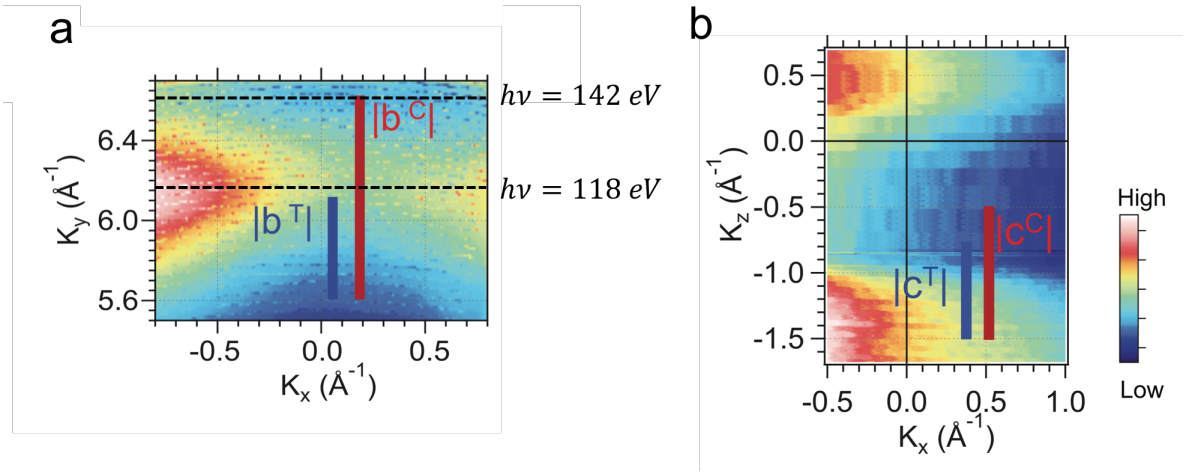

Figure 5.2: Constant energy cuts of the electronic structure measured (a) out-of-plane (2340 meV below the VBM for photon energies 74 eV < hv < 200 eV) and (b) in-plane (VBM at hv = 130 eV). The size of the lattice vectors for the cubic (red, C) and tetragonal structures (blue, T) are indicated. The spectral weight seems to follow the cubic periodicity.

is not properly oriented in the in-plane direction, we still do not know if we measure through a high symmetry direction. However, the electronic states k_y must exhibit the periodicity of Brillouin zones. The detection range is longer than 1.0 $Å^{-1}$, which is the biggest relevant Q vector in this system, related to a single PbI_6 octahedron (red line in Fig. 5.2(a)). We can therefore identify the high symmetry planes as the mirror planes, which correspond to photon energies of 118 eV and 142 eV at the maximum and minimum intensities along the k_y direction.

It is puzzling at first sight to observe that the apparent periodicity of the spectral weight does not correspond to the tetragonal phase, as expected for the working temperature (170 K). The periodicity seems to correspond to the red b^c-vector (around 1 $Å^{-1}$) instead of the blue one, meaning that the spectral weight follows the cubic periodicity in k-space. In order to check that the b axis in not contained in the plane, we have measured the electronic structure parallel to the surface (i.e. k_x and k_y) (Fig. 5.2(b)). Once again, the lattice parameter c of the tetragonal unit cell is too small to reproduce the spectral weight. The cubic lattice vector agrees better. After our analysis of in- and out-of-plane dispersions, we conclude that both parallel and perpendicular spectral features agree with the cubic periodicity despite the system being in principle in the low temperature tetragonal phase.

After the puzzling result about the periodicity of the spectral weight, we performed X-ray diffraction to check the atomic structure and try to understand the observed periodicity. Fig. 5.3(a) and (b) show the (h 0 l) and (0 k l) planes in reciprocal space at 200 K. The absence of rings around the Bragg reflection show the absence of polycrystals. The structure is found

Crystal system	Tetragonal
Space group	I4/mcm
a (Å)	8.80210(10)
b (Å)	12.6777(8)
c (Å)	8.80210(10)
α (°)	90
β (°)	90
γ (°)	90
Volume (Å^3)	982.23(6)
Z	8
Reflections collected	1831
Indexed reflections	1583
R-factor	0.0302

Table 5.1: Atomic structure of MAPI at 200 K.

Atomic positions	X	Y	Z
Pb	0	0	0
I1	0	0.25	0
I2	-0.29873(4)	0.007644	0.20128(4)
N	0.0778(13)	0.2857(12)	0.4222(13)

Table 5.2: Atomic positions of MAPI at 200 K shown in reduced units.

to be tetragonal with lattice parameters a = 8.80 Å, b = 12.68 Å and c = 8.80 Å, shown in Table. 5.1, in agreement with the expectations [112, 125]. We have furthermore refined the atomic positions, necessary for our theoretical calculations. Table 5.1 also shows the R-factor obtained in our refinement, which quantifies the agreement between the crystallographic model and the experimental X-ray diffraction data, i.e. how well the refined structure predicts the observed data. In general, just about 9.5% out of 500,000+ crystals can reach an R-factor lower than 0.03. Our refinement has reached a very satisfactory value of 0.0302. The final atomic positions as well as other structural parameters are shown in Fig. 5.3(c) and (d) and Tables 5.2 and 5.3.

The diffraction results indicates that the atomic structure at 170 K corresponds to a tetragonal phase as expected. However, the photoemission spectral weight seems to exhibit a cubic periodicity. Even if the spectral weight does not necessarily exhibit the symmetry of

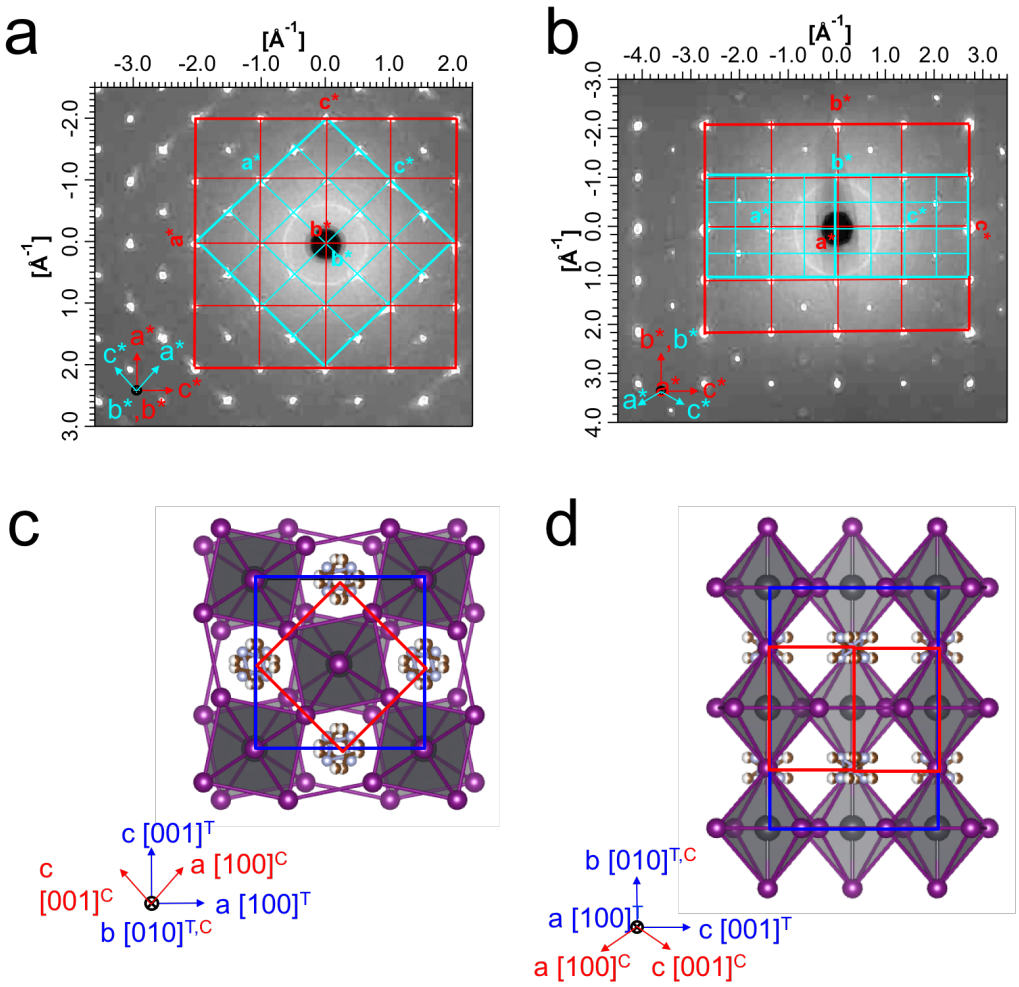

Figure 5.3: X-ray diffraction measurements of MAPI in the tetragonal phase in the (a) (h 0 l) and (b) (0 k l) planes at 200 K. The projected reciprocal unit cells for the tetragonal periodicity (in blue) and cubic periodicity (in red) are indicated with a space group of I4/mcm. The refined structure are projected on (c) the ac plane and (d) on the bc plane. In the tetragonal structure, a distortion of the octahedra lattice promotes a larger unit cell (in blue) with respect to the cubic one (in red). The crystallographic directions are indicated by the tetragonal (T) and cubic (C) lattice vectors.

Name	U_{11}	U_{22}	U_{33}	U_{12}	U_{13}	U_{23}
Pb	0.02090(5)	0.02015(6)	0.02090(5)	0	0	0
I1	0.0518(2)	0.01475(10)	0.0518(2)	0	0	0
I2	0.03769(12)	0.0520(2)	0.03769(12)	0.00627(18)	0.02276(12)	0.00627(18)
N	0.042(4)	0.054(6)	0.042(4)	0	0	0

Table 5.3: Thermal parameters of MAPI at 200 K. Thermal parameters, i.e. atomic displacement parameters, represent the temperature dependent vibration of different atoms within the crystalline lattice.

the system, and only the bands do, the situation deserves further study. We have therefore determined the experimental band dispersion along the high symmetry directions and compared to simulations to better understand the system periodicities. This will be discussed in more detail in section 5.2.2 and 5.2.3.

5.2.2 Orientation of the Brillouin zone in 3D system

In the previous section, we observed that the photon energy of 142 eV corresponds to the minimum intensity in k_y, that should correspond to the ΓXM plane of the cubic Brillouin zone. Fig. 5.4(a) shows the Brillouin zone of a cubic system with a highlighted ΓXM plane, where the band structure has been determined. Fig. 5.4(b) is a 3D scheme of our theoretical band dispersion in this plane. The theoretical band structure shows the maximum of the valence band at M point, although it is rather faint. Γ is the next maximum, much more stronger. At a slightly deeper binding energies, the bands start to disperse towards X. Experimentally, the highest intensity allows to identify Γ, as shown in Fig. 5.4(c). By increasing the binding energy by 300 meV, intensity starts to develop towards X points as observed in Fig. 5.4(d). Finally, the deepest states, which correspond to I 5p and Pb 6s, give rise to intensity at Γ point as shown in Fig. 5.4(f). In this way, the orientation of the Brillouin zone and the high symmetry points are identified.

If we compare now to our calculations (Fig. 5.4(g) to (j)), we see an overall good agreement in all the sequence of the constant energy cuts. Starting from the valence band maximum, the spectral weight appears between Γ and M. Slightly below the valence band maximum, the spectral weight exhibits a triangular shape appearing both in the experiment and the calculations. At higher binding energies, a squared-shape intensity larger than a cubic Brillouin zone appears, that it is again satisfactorily reproduced by calculations. This intensity then enhances between Γ and X, a maximum of intensity observed in the experiment. These constant energy cuts also indicate that the spectral weight follows more a cubic Brillouin zone than the tetragonal one, which is smaller than the Brillouin zones indicated in Fig. 5.4. It can

also be appreciated the strong effect of matrix elements, since the different Brillouin zones look often inequivalent.

5.2.3 k-resolved electronic band structure dispersion

The experimental and theoretical cuts are not obtained exactly at the same energies, which may indicate an eventual renormalization of the energy scale. A fast indication of the eventual renormalization of the band structure can be obtained by analyzing the density of states. Fig. 5.5 presents an experimental simulation of the density of states by integrating in angle the angle-resolved image. This "experimental DOS" is compared to the theoretical calculation from [118]. The experimental states can now be identified with the help of the calculations. The states between the valence band maximum and -3.5 eV correspond to the antibonding in-plane σ bonds between I 5p and Pb 6s. The peaks appearing at higher binding energies (-6.6 eV and -8.5 eV) are related to the dispersiveless states of organic cations and some Pb 6s states. An overall renormalization factor of 0.875 on the theoretical calculation is needed to compare to the experiment. This normalization factor allows to understand how the difference in the binding energies between the experiment and simulated constant energy cuts of Fig. 5.4. Such a renormalization should be even more evident from the band dispersion along the high symmetry directions (Fig. 5.7).

Before analyzing our experimental band dispersion, the simulated photoemission spectrum have been obtained (Fig.5.6). The calculations confirm the cubic symmetry of the spectral weight when introducing the tetragonal structure. In the ground state, the band structure of tetragonal MAPI (shown in Fig.5.6(a)), has the valence band maximum at Γ, and the a-vector between Γ points is 0.714 $Å^{-1}$. Therefore, in the simulated ARPES data of tetragonal MAPI (shown in Fig.5.6(b)), we should see the intensities at k_x = -1.428, -0.714, 0, 0.714, 1.428 $Å^{-1}$ (i.e. at each of the Γ points of the tetragonal Brillouin zones). However, the intensity maximum just appears at k_x = -0.714 and 0.714 $Å^{-1}$ corresponding to a cubic symmetry. The reason for this symmetry of the spectral weight will be discussed in the next section.

To determine the experimental band structure, we obtain the results from cuts of the whole set of constant energy cuts and its simulation (Fig. 5.7(a) and (f)). The ΓMΓ corresponds to cut A and ΓXΓ to cut B. The raw photoemission data is shown in Fig. 5.7(b) and (g). The simulated ARPES spectra are shown in Fig. 5.7(e) and (j), respectively. The straightforward comparison is not obvious, because of the broad experimental features. After broadening the simulated spectra and superimposing its DOS, we obtain the simulated spectra 5.7(c) and (h). We now reproduce the asymmetric spectral weight distribution. To better appreciate dispersions, a second derivative treatment has then been performed on the experimental data, as shown in Fig. 5.7(d) and (i). The minimum of the dispersion is at the bottom of the valence band (around -3.4 eV at Γ point) and the maximum of the dispersion around -0.8 eV at Γ can

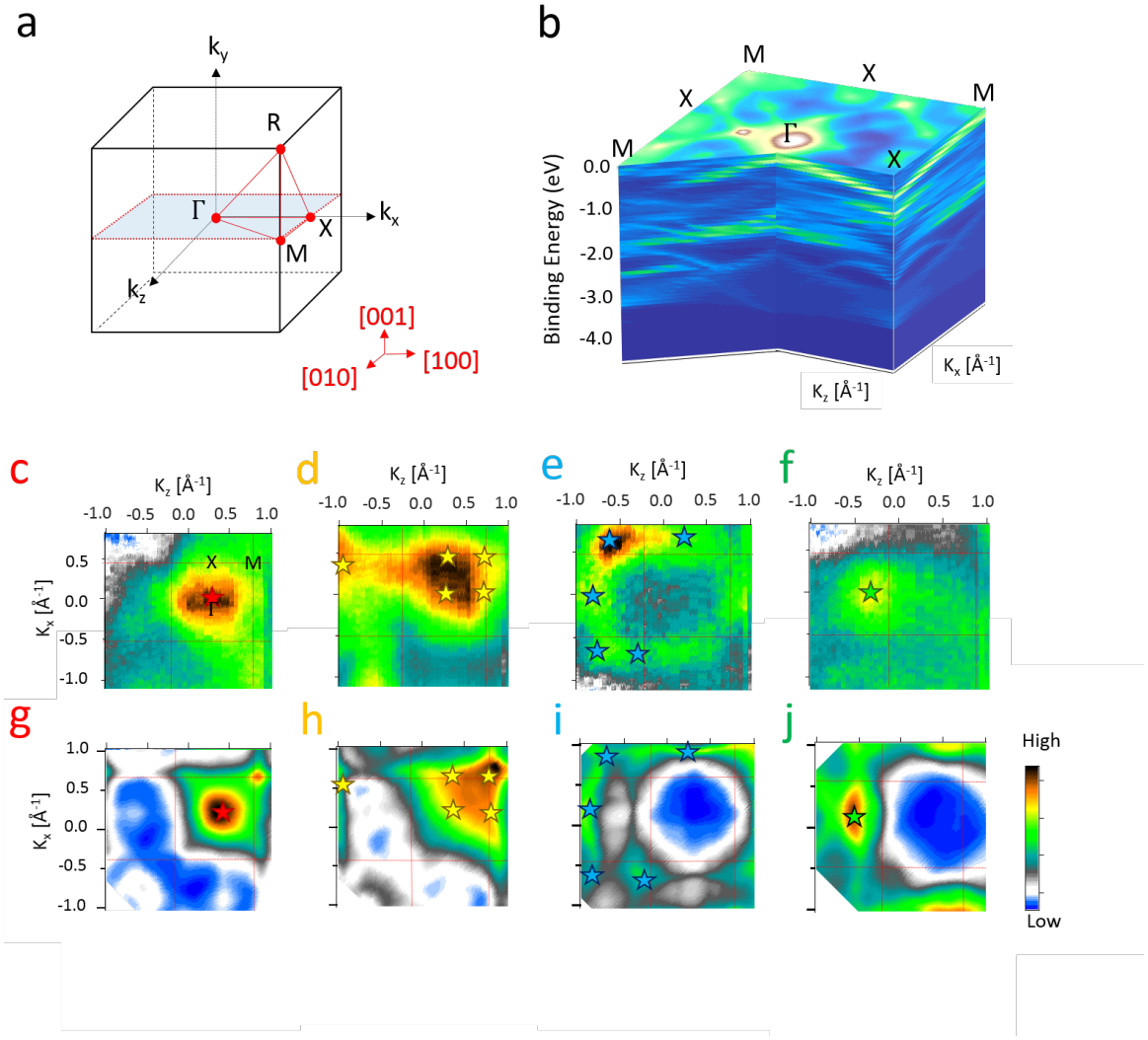

Figure 5.4: Constant energy cuts of the electronic structure of MAPI. (a) Cubic Brillouin zone. The highlighted red plane corresponds to the constant energy cuts studied later. (b) Sketch of the main expected bands in the ΓXM plane. Constant energy cut of the electronic structure in the ΓXM plane at a binding energy corresponding to (c) 100 meV, (d) 300 meV, (e) 2500 meV and (f) 2900 meV below the valence band maximum. Corresponding constant energy cuts calculated using the SPRKKR code shown for energies of (g) VBM, (h) 500 meV, (i) 2800 meV, and (j) 3400 meV below the valence band maximum. Cubic Brillouin zones are shown as red squares. The indicated stars are a guide for the comparison between theory and experiment.

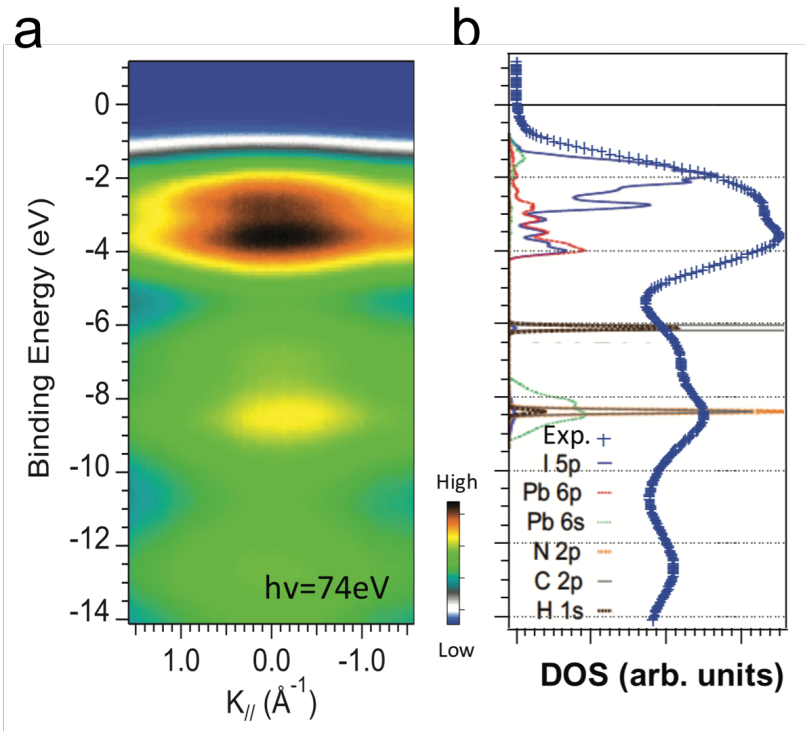

Figure 5.5: Electronic structure of MAPI hybrid perovskite with k-resolution. (a)Spectrum at normal emission in a wide binding energy range. (b) Integrated valence band in (a) compared to theoretical calculations [118].

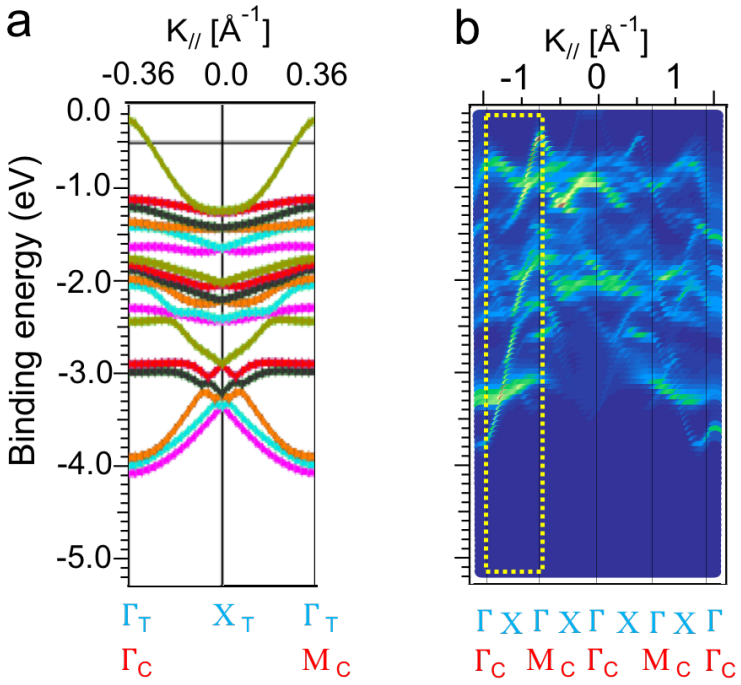

Figure 5.6: (a) Band structure of MAPI in the tetragonal phase performed with Wien2k by Jan Minar and Saleem Khan (University of West Bohemia, Czech Republic). (b) ARPES simulation of tetragonal MAPI. The spectral weight seems to follow the cubic periodicity.

now be observed (dotted rectangles). A direct comparison between these spectral features in the experiment and in the calculation, shows that bands become flatter in the experiment.

A detailed measurement close to the Fermi level should allow to better appreciate the flatter experimental bands. Fig. 5.8 shows a zoom of the electronic structure along the high symmetry direction. Raw data show the small dispersion of the valence band maximum. The second derivative is performed for better observing the dispersion, which shows a nice agreement to the simulated band structure in (c) and (f) as highlighted in red.

The electron effective mass of the topmost band indicated in Fig. 5.8(e) pointed with a yellow arrow can then be determined. At the maximum, the band structure can be locally approximated as:

$$E(k) = E_0 + \frac{\hbar^2 k^2}{2m^*}, \tag{5.1}$$

where $E(k)$ is the energy of an electron at wavevector k in that band, E_0 is the energy offset of the band, and m^* is the effective mass. Therefore, by fitting the experimental data, we obtain m^*/m_e equal to 0.214, which is 25% more than previous theoretical calculations [37, 113, 116]. Again, as in PEPI, the experimental mass is larger than in calculations, meaning that electrons are more localized and the electron hopping is more difficult.

5.2.4 Periodicity of the spectral weight

The structure of our crystal at 200K is tetragonal as expected and indicated by our X-ray diffraction experiments. How can then be explained the cubic symmetry of the spectral weight in photoemission? A cubic symmetry may be related to the high temperature phase (above 330K) of MAPI, where the sides of all the octahedra are perfectly aligned (Fig. 5.9). It is indeed not the case as we demonstrated by X-ray diffraction. Moreover, a dynamical cubic phase will consist of oscillating octahedra around a cubic average position. Instantaneously, the system will be in a tetragonal phase, while on average, it will correspond to a cubic phase with very anisotropic vibrational ellipsoids. Again, this situation is not observed by X-ray diffraction (Fig. 5.3).

The experimental band measurements and the theoretical band calculations show a cubic symmetry of the spectral weight, despite the system being in a tetragonal phase. As in the photoemission experiment at 170 K, the sample temperature is well below the cubic-tetragonal transition, structural reminiscences of the cubic phase can be neglected. A possible explanation of the different periodicities observed in photoemission and in X-ray diffraction might be in the depths explored by the two techniques. X-ray diffraction is a bulk sensitive technique and photoemission is a surface sensitive technique. However, surface reconstructions usually give rise to unit cells larger than the bulk, so the small lattice parameter of cubic structure can not be due to surface reconstructions [126, 127].

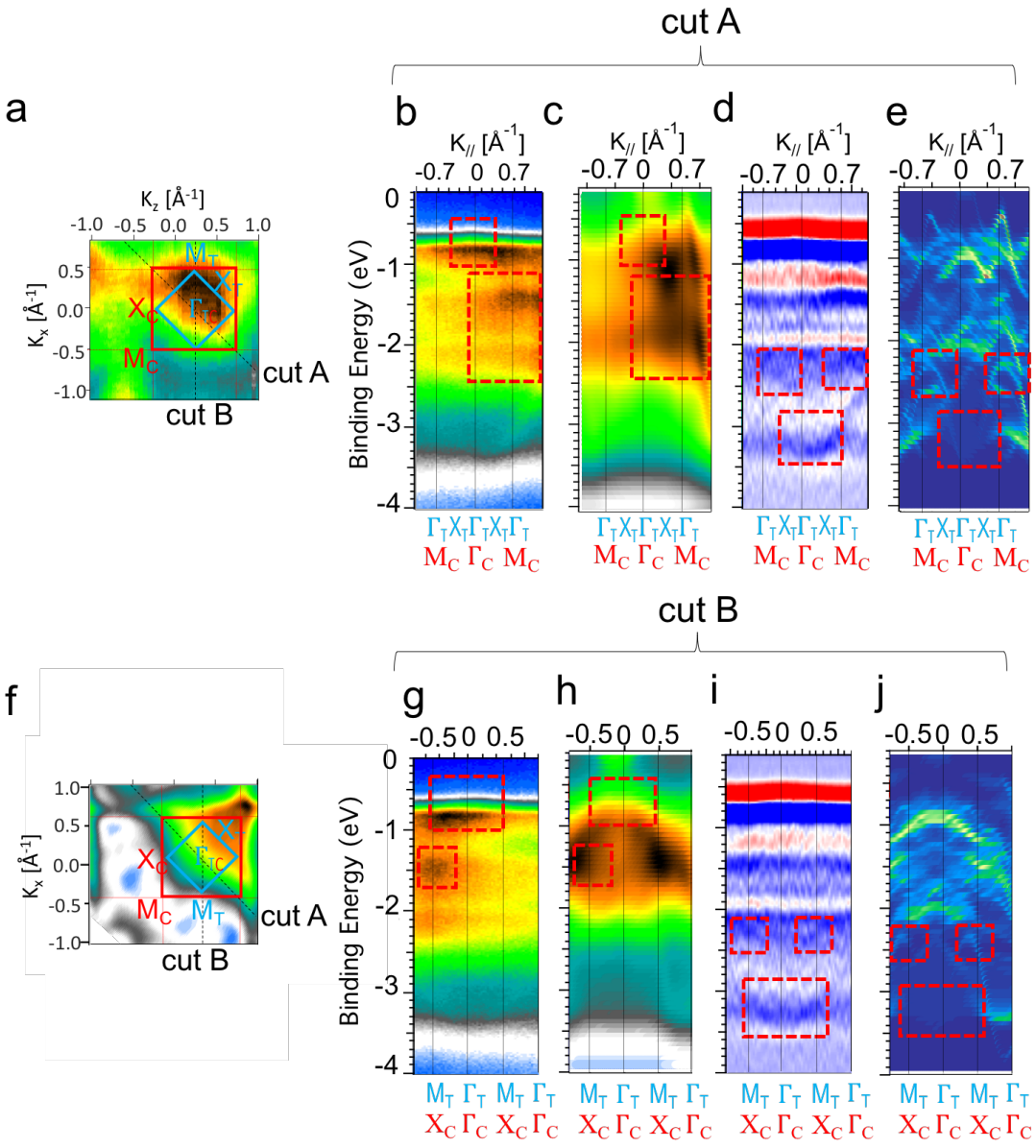

Figure 5.7: Electronic structure with k-resolution of MAPI measured at photon energy of 142 eV. (a) Constant energy cut at 300 meV below the valence band maximum. The cubic Brillouin zone (red rectangle) and the tetragonal Brillouin zone (blue rectangle) are shown together with the cuts along the high symmetry directions. (b) Photoemission along the MΓM direction of the cubic phase. (c) Simulated ARPES spectra of (b) (bands broadened by a factor of 14 with the density of states superimposed). (d) Second derivative of the raw data in (b). (e) Simulated ARPES spectra along MΓM of the cubic phase. (f) Calculated constant energy cut at 300 meV below the valence band maximum. (g) Photoemission measurement along ΓXΓ direction of the cubic phase (cut B). (h) Simulated ARPES spectra and (i) second derivative of the raw data in (g). (j) Simulated ARPES spectra along XΓX direction of the cubic phase. The high symmetry points of the tetragonal and the cubic Brillouin zones are indicated. The dotted rectangles indicate the agreements of the dispersions between the experiments and calculations.

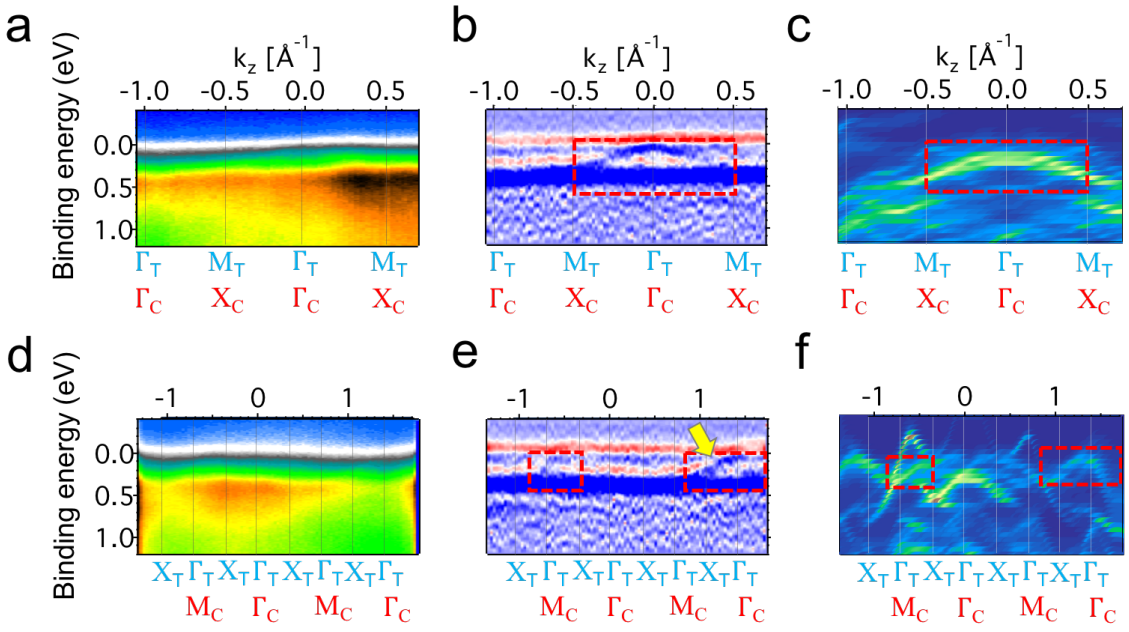

Figure 5.8: Electronic structure with k-resolution of MAPI measured close to the Fermi level. (a) Photoemission measurement along ΓXΓ direction of the cubic phase (cut B in Fig. 5.7). (b) Second derivative of the raw data in (a). (c) Simulated ARPES spectra along ΓXΓ of the cubic phase. (d) Photoemission measurement along MΓM direction of the cubic phase (cut A in Fig. 5.7). (e) Second derivative of the raw data in (d). (f) Simulated ARPES spectra along MΓM of the cubic phase.

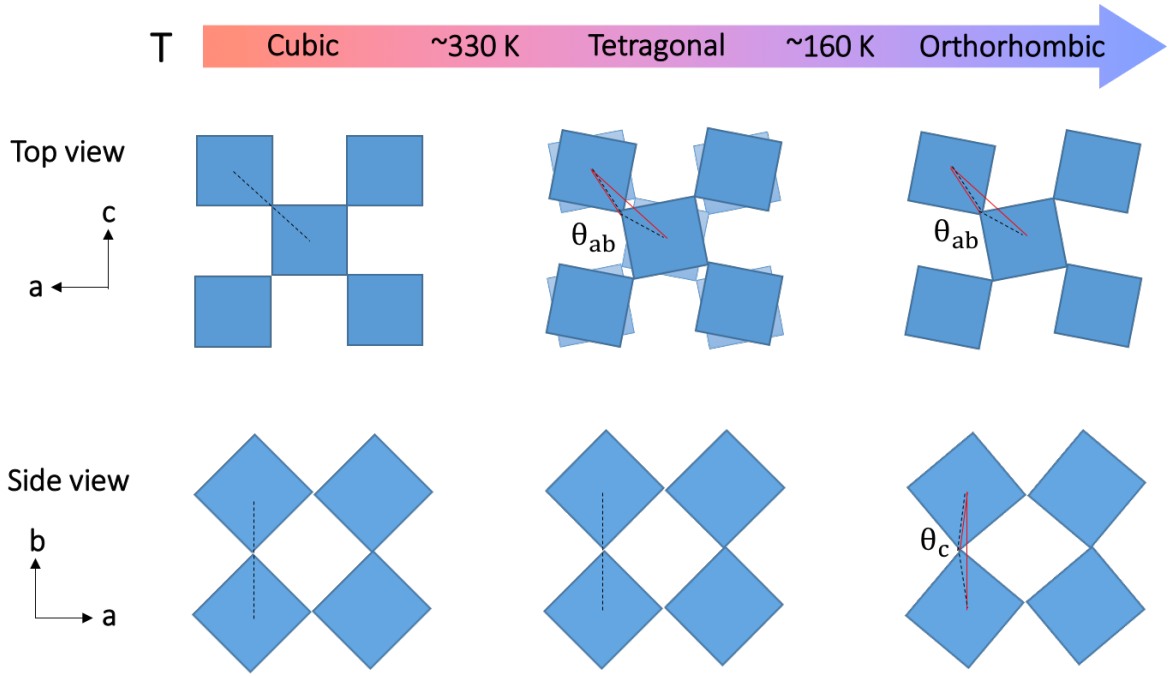

Figure 5.9: Phase transition of MAPI as a function of temperature shown in top views and side views. θ_{ab} (=154±4) is the distortion angle in-plane and θ_c (=164±4) is the distortion angle out-of-plane. At high temperature (above 330 K), MAPI is in the cubic with a space group Pm-3m. When the temperature decreases below around 330 K, the octahedra in-plane starts to distort and the structure transmits to tetragonal phase with a space group of I4/mcm. If the temperature decreases below 160 K, the out-of-plane octahedra starts to distort again and the structure becomes orthorhombic with a space group P4/mcm.

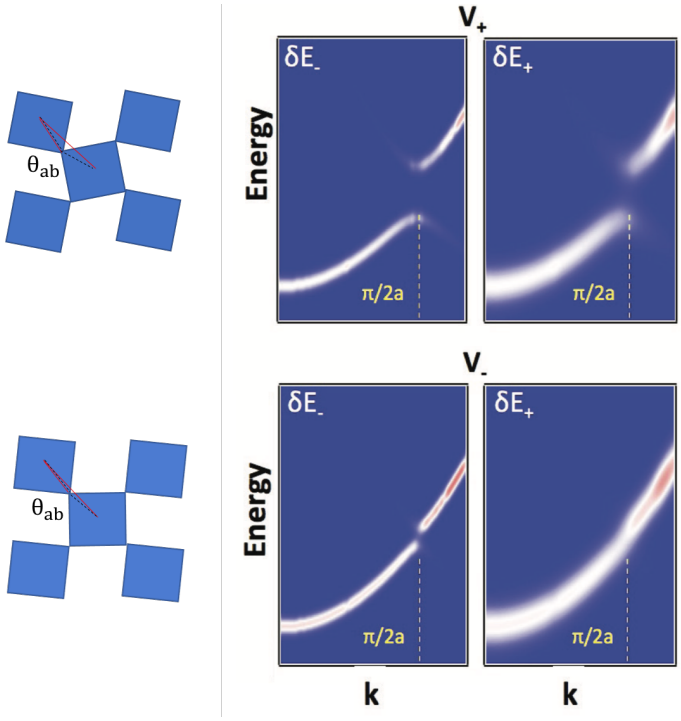

Figure 5.10: Simulation of the photoemission spectral weight in a one-electron model [128, 129, 130]. Weak (V_-) and strong (V_+) superperiodic potentials are considered, emulating the effect of the tetragonal distorsion. For these potentials, two bands are represented with low and high spectral widths (δE_- and δE_+ respectively). When bands are broad and the superperiodic potential is small, gap and band foldings may not be appreciated.

We must therefore consider that the system is in a tetragonal phase, so there should be a band gap opening and band foldings at the tetragonal Brillouin zone edges. By applying different tetragonal potentials, i.e. different distortion angles between the octahedra, the amplitude of the gap and the spectral weight in the folded band could change. Fig. 5.10 shows the effect of introducing a weak (strong) tetragonal potential V_- (V_+). Two different spectral widths are considered, a small δE_- and a larger δE_+. The effect of the potential is doubling the lattice parameter from a to $2a$ equivalently to the cubic-tetragonal distortion. This simulation suggests that even if a tetragonal potential is applied, if the folded spectral weight is small because the potential strength is not high and the bands are broad, the spectral weight follows a cubic symmetry. It is probably the case in our system, where the spectral features are very broad.

5.3 Electronic relaxation dynamics

Once the static band structure was understood, we studied the electronic relaxation dynamics by two-photon photoemission. The pump and the probe laser pulses are generated from a fundamental laser beam of energy $h\nu_0 = 1.55$ eV. The pump laser is performed with the second harmonic of the fundamental beam at $h\nu_1 = 3.15$ eV, and the probe laser uses the third harmonic at $h\nu_2 = 4.7$ eV [131]. Within a variable delay time, the probe pulse ejects the excited electrons above the vacuum level and allows to follow the relaxation dynamics. The sample has been photoexcited at 130 K by 20 μJ/cm^2 pump pulses with a temporal resolution of 50 fs. The pulse leaded to an excited electron-hole density of 8×10^{18} cm^{-3}, according to the reported absorption coefficient [132].

5.3.1 Ultrafast cooling of hot electrons

Fig. 5.11(a) shows the result of probing the initially photoexcited system with different delay times. The color scale is a map of the photoelectron intensity as a function of kinetic energy and delay time. The electronic dynamics can be directly observed from the evolution of the photoelectron intensity. The conduction band minimum is defined as the nominal kinetic energy, $E_c = h\nu_2 - \phi + E_g - \mu_F + E_v = 0.45$ eV, where $\phi = 4.3$ eV is the work function of the analyzer (as shown in Fig. 2.18).

The evolution of the different energy states in the conduction band can be seen in Fig. 5.11(b) for some selected delay times. At the maximum overlap between pump and probe (at zero delay), three peaks are observed. The first peak locates approximately at the bottom of the conduction band, a second peak is found at $E' = E_c + 0.35$ eV, and a third peak at $E'' = E_c + 0.9$ eV. These peaks can be identified by looking in the band structure for the allowed optical transitions in MAPI (Fig. 5.12). Photoexcited electrons are generated from a pump beams at $h\nu_2 = 3.15$ eV, which induces optical transitions to the conduction band mainly at these energies, E_c, E' and E''. Within the first picosecond, the excited electronic distribution varies strongly. Peaks of E' and E'' energies strongly decrease since the electrons thermalize the excess energy towards the bottom of the conduction band via electron-electron scattering and phonon emission within the first hundreds of femtoseconds. No carrier multiplication should take place here since the photon energy of the pump laser is lower than twice the band gap. The spectra acquired at higher delay times, between 1 ps and 10 ps, present a shoulder at an excess energy around 0.2 eV, previously observed only in the tetragonal phase and that has been ascribed to an unconventional kind of polaronic dressing [133, 134]. It is currently under investigation and requires additional measurements to be confirmed.

Quantitative information about the relaxation can be obtained from the evolution of the total kinetic energy of the electrons. This information is contained in the photoemission

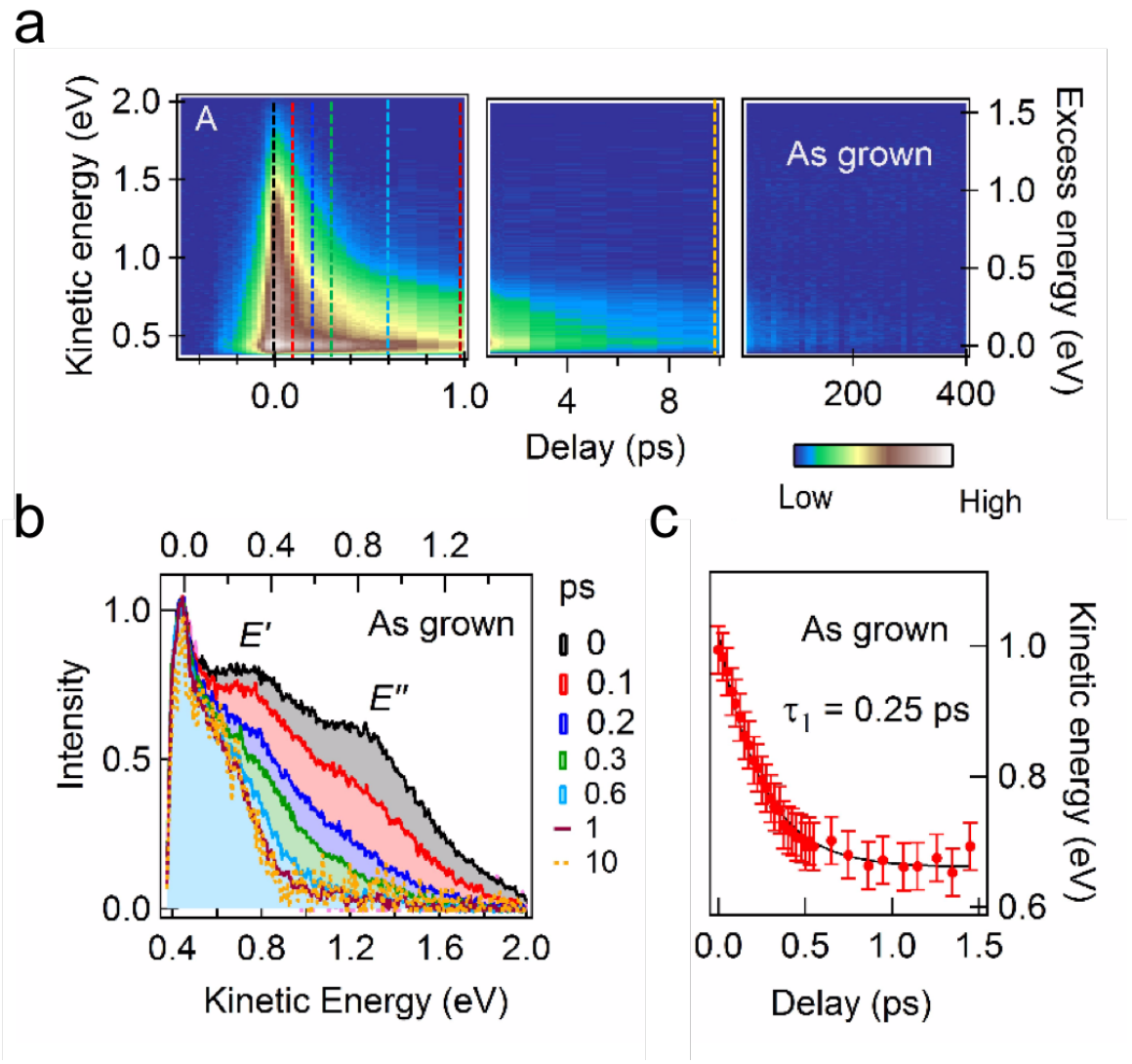

Figure 5.11: (a) Photoelectron intensity map in the as-grown sample as a function of kinetic energy and pump-probe delay. (b) Energy distribution curves acquired at different values of the pump-probe delay and normalized to their maximum value. (c) Evolution of the average kinetic energy as a function of time. The solid line is an exponential fit with time constant $\tau_1 = 0.25$ ps.

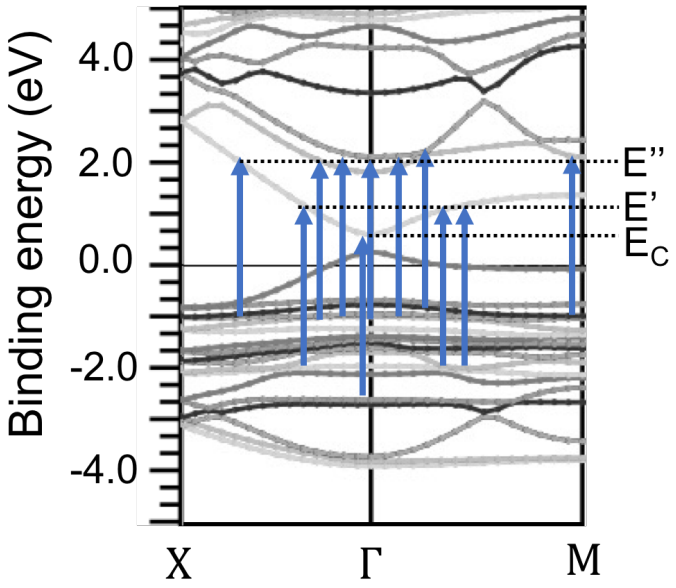

Figure 5.12: Band structure of $MAPbI_3$ calculated from Wien2k by by Jan Minar and Saleem Khan (University of West Bohemia, Czech Republic). The blue arrows stand for direct transitions induced by photons with $h\nu_1 = 3.15$ eV.

intensity as a function of time according to:

$$\langle E \rangle_t = \frac{\int I(E,t) E dE}{\int I(E,t) dE}, \tag{5.2}$$

where E is the kinetic energy, t is the pump-probe delay time, and $I(E,t)$ is the photoelectron intensity. Fig. 5.11(c) shows the average kinetic energy as a function of time $\langle E \rangle_t$ along with an exponential fit to the decay. The time constant $\tau_1 = 0.25$ ps agrees well with the values for MAPI thin films [134]. The hot electrons reach the quasiequilibrium after around three times of the time constant τ_1 (0.75 ps). This relaxation time is faster than in inorganic semiconductors [135], possibly due to the coupling of the excited carriers to the internal vibrations of the organic cations. The stretching modes of C-H and N-H bonds holding quantum energy of 370 - 400 meV could indeed absorb the excess energy of photoexcited electrons [136]. Another reason for this fast relaxation time is because excitons could be sizably coupled to an organic mode with a quantum energy around 40 meV in the optical sidebands of two-dimensional hybrid perovskites [137].

5.3.2 Diffusion in the as-grown sample

After determining the short-term electronic dynamics, we analyzed the long-term electronic dynamics. The instantaneous electronic concentration at the surface of the sample is:

$$\int I(E,t)dE. \tag{5.3}$$

The photoemission intensity decreases because electrons are diffusing from the surface into the bulk (Fig. 5.13(a)). By modeling the Brownian motion of the electron into the bulk, and taking into account an optical penetration depth of $\alpha^{-1} = 50$ nm [132], the electronic concentration at a distance x from the surface and a pump-probe delay t is [138]:

$$n(x,t) \propto \frac{1}{2} exp\left(-\frac{x^2}{4Dt}\right) w\left(\alpha\sqrt{Dt} - \frac{x}{2\sqrt{Dt}}\right) + \frac{1}{2} exp\left(-\frac{x^2}{4Dt}\right) w\left(\alpha\sqrt{Dt} + \frac{x}{2\sqrt{Dt}}\right), \tag{5.4}$$

where D is the electron diffusion constant at 130 K and $w(z) = exp(z^2)[1 - erf(z)]$. The mobility μ is limited by electron-phonon scattering [139] scaling as $T^{-\frac{3}{2}}$. Therefore, by referring to the suggested value of D [28] combined with the Einstein relation, we have:

$$D = \mu k_b T \propto T^{-\frac{1}{2}}, \tag{5.5}$$

and the electron diffusion constant at $T = 130$ K can be estimated. The resulting value, $D = 3$ cm^2/s, can be applied back into the electronic density (Eq. 5.4).

Fig. 5.13(b) shows the modelization of the electronic density $n(x,t)$ as a function of the depth x for selected values of the delay time t. The electrons diffuse into the bulk gradually from 10 to 100 picosecond. With this model, we fit the experimental results in Fig. 5.13(a), by calculating the electronic density $n(x,t)$ in a temporal window from 0.05 ps to 400 ps. In the first picosecond, the decay is much more faster than the diffusion, because of the rapid variation of the photoemission cross section during to the thermalization process [134], which therefore does not allow to apply Eq. 5.3. After 3 ps of the delay time, we can apply the Eq.5.3 and we observe that decay follows a diffusion behavior.

5.3.3 Electronic localization in annealed samples

After studying the drift and diffusion of the electrons in as-grown single crystals of MAPI, we have studied the impact of the defects in the relaxation dynamics. One common degradation source is annealing, so we have studied the relaxation dynamics in differently annealed samples. Samples were annealed in air at 100°C and 200°C for 30 minutes and compared to the non-annealed sample in Fig. 5.14. The photoelectron intensity map shows that the non-annealed and the 100°C annealed sample show a similar behavior at the short time scale, below 1 ps. However, both annealed samples show a remnant intensity lasting longer than 300 ps. It seems that a trap state close to the bottom of the conduction band exists in them, trapping electrons for longer times.

Photoluminescence provides evidence from these trap states (Fig. 5.15(a)). When in-

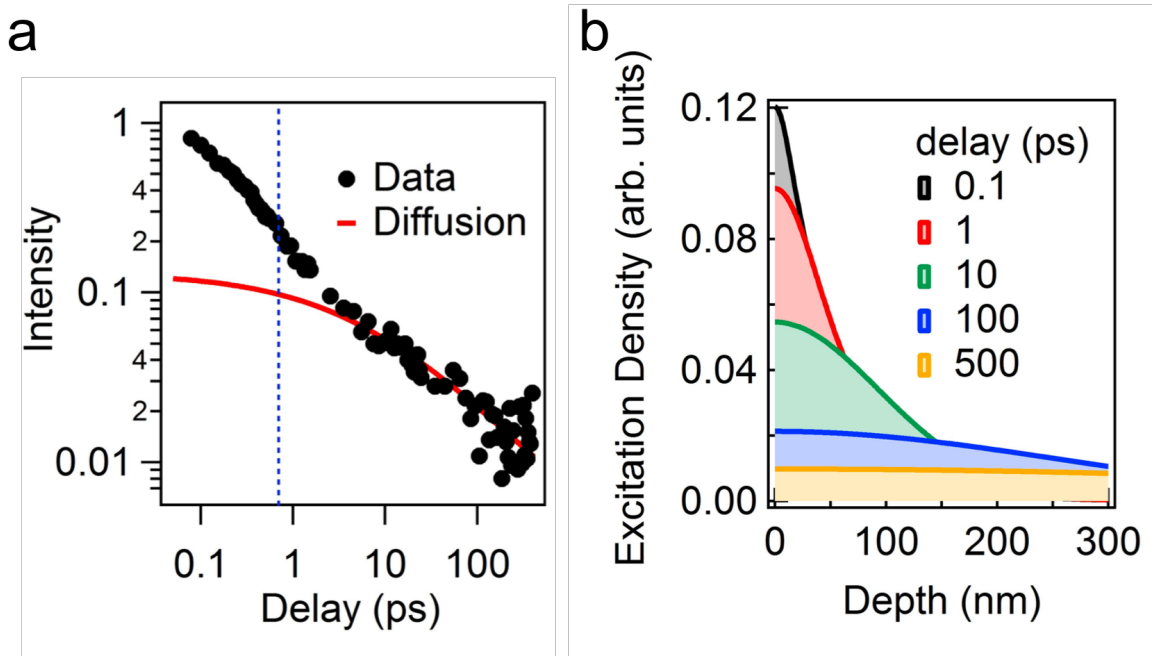

Figure 5.13: (a) The integrated intensity of the 2PPE signal (black marks) as a function of time is compared with the diffusion model (red line). The dotted blue line at $t = 3\tau_1$ indicates the delay time when electrons have fully thermalized. (b) The density profile of photoexcited electrons is calculated by the diffusion model of Eq. (5.4) for selected delay times.

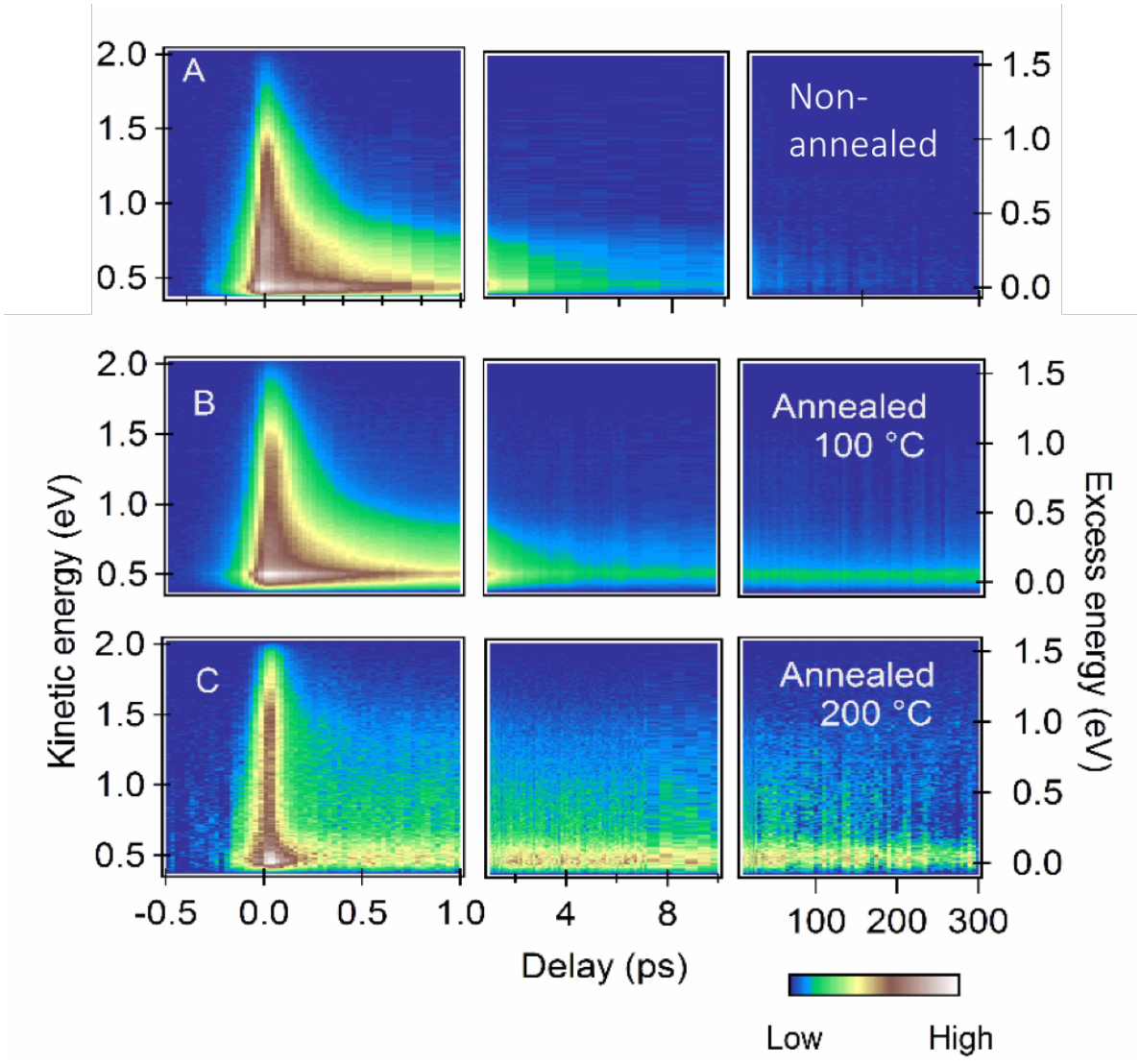

Figure 5.14: Photoelectron intensity map of (a) a non-annealed sample, and samples annealed at (b) 100°C, and (c) 200°C, as a function of kinetic energy and pump-probe delay.

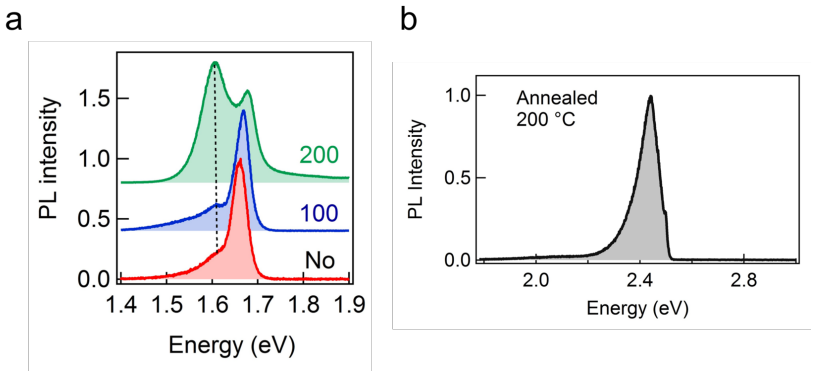

Figure 5.15: (a) Photoluminescence spectra acquired from non-annealed, annealed at 100°C, and annealed at 200°C samples. The dashed line shows the development of trapped states upon annealing. (b) Photoluminescence emitted in the visible spectral range from the sample annealed at 200°C and measured at 10 K. The peak located at 2.45 eV arises from carrier recombination in PbI_2 inclusions.

creasing the annealing temperature, an additional peak in the photoluminescence spectrum arises around 60 meV below the band-gap value. The state originating this transition is the responsible for the partial localization of the electrons. This localization gives rise to the long-term temporal evolution shown in Fig. 5.16. The effect of electron trapping can be observed by deviations from the $1/\sqrt{t}$ decay at long times in the annealed samples. For the sample annealed at 100°C, the localization starts to take place in a few picoseconds, while for the 200°C annealed sample, the localization starts as soon as the electrons cool down, in less than a picosecond. The relaxation time correlates with the defect density, so the fast localization in 200°C annealed sample indicates an high density of defects. The atomic origin of these defects can be related to the compositional disorder of degraded samples [140]. For annealing above 150°C, a partial conversion of MAPI into PbI_2 is known to take place [141]. It is probably the case for the 200°C annealed sample, since low-temperature photoluminescence measurements show a PbI_2 peak (Fig. 5.15(b)).

5.4 Conclusions

We have studied the electronic properties of MAPI by electron spectroscopies that we have correlated to the atomic structure. We have succeeded in measuring the band structure of MAPI. The resulting effective mass m^* is 0.21 m_e, which is 25% higher than previous calculations for the system [113, 37]. We also observe that the spectral weight follows a cubic periodicity even when the sample is in the tetragonal phase. The reason is that the band folding induced by the tetragonal potential cannot be appreciated due to the very broad experimental bands. Hence, the operation of the solar cells across the cubic-tetragonal

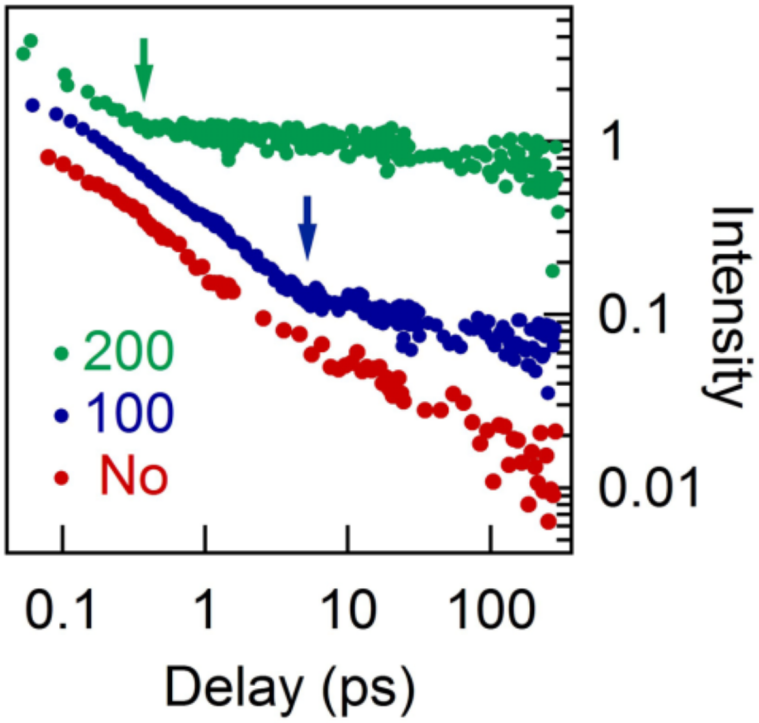

Figure 5.16: Temporal evolution of the integrated 2PPE signal in the non-annealed and annealed samples. The arrows indicate the characteristic time scale when electronic trapping takes place.

transition will not be affected in a drastic way. All these results are satisfactorily reproduced by theoretical calculation of ARPES. The large spectral width also relaxes the absorption conditions for photons, with a probable impact on the efficiency of perovskite cells.

We have also performed directly visualization the electronic cooling at subpicosecond delay times. Photoexcited carriers thermalize in this short time scale due to the coupling to organic cation vibrations. In the long-term timescale, the electron dynamics is ruled by diffusion. Finally, we have also analyzed the influence of common structural defects, those induced by annealing, which may arise in aged solar cells. After annealing, photoexcited electrons are localized during more than 300 picoseconds by shallow traps.

Chapter 6

Conclusions and perspectives

In this thesis, we have studied photovoltaic materials focusing on their electronic states, their relaxation dynamics and relating them to their atomic structure. We have studied the active materials in the best-performance modules in the market (c-Si/a-Si:H heterojunction solar cells) and in one of the emerging solar cell technologies (hybrid organic-inorganic perovskite, both with 2D and 3D materials).

In amorphous silicon heterostructures (a-Si:H/c-Si), we have analyzed the impact of defects on the electronic properties by core level and valence band studies. The main results and perspectives are as follows:

- We have quantified the number of defects in the a-Si:H layer upon irradiation. By analyzing the Si 2p core level decomposition, we observe that under irradiation, the Si-H bonds decrease by $20 \pm 5\%$ in a-Si:H layer and become dangling bonds that some were bonded to oxygen at the surface. Irradiation therefore breaks the Si-H bonds and creates new dangling bonds.

- We have identified the electronic states associated to these dangling bonds induced by irradiation. Photoemission from the valence band has allowed us to identify the defect states at 0.3 eV above the VBM. A transition from the minimum of the conduction band to these states is 1.4 eV which is larger than the previously observed photoluminescence peak (1.2 eV). Therefore, we suspect the presence of defect states 0.2 eV below the conduction band minimum.

- A first perspective is therefore to try to identify the defect states near the conduction band minimum by inverse photoemission.

- A second perspective is to see how the system reacts towards annealing, when defect states are healed.

In the two-dimensional perovskite PEPI, we have studied the valence and conduction bands, theoretically and experimentally. Our results are listed below:

- We have managed to experimentally determine the valence and the conduction bands by angle resolved photoemission and inverse photoemission. To the best of our knowledge, this is the first determination of the electronic structure on such single crystals. This determination has required a preliminary study for measuring the samples under ultra high vacuum, as needed for electron spectroscopies.

- We have compared the experimental bands to our simulations of the spectral function. The overall agreement is satisfactory. We reproduce the main spectral features in a constant energy cut of the electronic structure through the valence band maximum. We also observe the asymmetry of the spectral weight intensity along $k_{||}$.

- We have observed flatter experimental dispersions of the valence band than the theoretical ones, indicating higher effective masses in the real system. This reflects that electrons become more localized and hopping is more difficult.

- We have studied the spin-orbit split bands that are more evident in the conduction band. Here, the bands do not seem to be strongly renormalized as in the valence band. The experimental spin-orbit split bands agree therefore with those of the calculations.

In the three-dimensional perovskite MAPI, we have studied its electronic states and their relaxation dynamics, and related both to the atomic structure. Our main results are:

- As in PEPI, we have performed the first k-resolved measurements of the electronic structure on single crystals.

- We have identified very broad spectral features in the experimental bands. This broadness relaxes the conditions for the optical transitions and should have an impact on the optical absorption and on the solar cell efficiencies.

- We have reproduced our measurements with photoemission simulations. We satisfactorily reproduce the different constant energy cuts of the electronic structure. Band dispersions are also qualitatively reproduced.

- Both in the experiments and in the calculations we see that the spectral weight follows a cubic periodicity while the system is structurally in the tetragonal phase, as determined by X-ray diffraction. This apparent contradiction in the observed periodicities can be explained by the bands broadness, that hide the band folding due to the tetragonal distortion.

- From the band structure, we have determined the effective mass of the topmost band. The resulting effective mass m^* is 0.21 m_e, which is 25% higher than previous calculations for the system, reflecting a higher electronic localization as previously observed in PEPI.

- We have measured the cooling of the excited electrons. In a subpicosecond time scale, the thermalization of photoexcited carriers is done through the coupling with the vibrations of organic cations. At longer timescales (hundreds of picoseconds), the electron diffusion controls the dynamics.

- We have also studied the dynamics as a function of the defect content. We have introduced defects by annealing the samples at different temperatures, a process that can simulate aged solar cells. Here, photoexcited electrons are localized by shallow trap states for times longer than 300 picoseconds.

- The first perspective of all our work on perovskites is to determine experimentally the conduction band of MAPI by inverse photoemission as we did for PEPI.

- A second perspective is to determine the nature, density, and mobility of charge carriers. We have started to do preliminary Hall effect measurements with this goal. Setting good contacts and measuring these highly resistive samples are challenges to overcome.

- A third perspective is to correlate the electronic relaxation dynamics with the structural dynamics. In particular, the electronic band structure is modified by the cation orientation. To correlate the electronic properties and the structure, we have performed preliminary time-resolved X-ray diffraction experiments to see how the organic cation reorientates after optical excitation.

Bibliography

[1] Stefaan De Wolf, Antoine Descoeudres, Zachary C Holman, and Christophe Ballif. High-efficiency silicon heterojunction solar cells: A review. *green*, 2(1):7–24, 2012.

[2] Kunta Yoshikawa, Hayato Kawasaki, Wataru Yoshida, Toru Irie, Katsunori Konishi, Kunihiro Nakano, Toshihiko Uto, Daisuke Adachi, Masanori Kanematsu, Hisashi Uzu, et al. Silicon heterojunction solar cell with interdigitated back contacts for a photoconversion efficiency over 26%. *Nature Energy*, 2:17032, 2017.

[3] Julian Burschka, Norman Pellet, Soo-Jin Moon, Robin Humphry-Baker, Peng Gao, Mohammad K Nazeeruddin, and Michael Grätzel. Sequential deposition as a route to high-performance perovskite-sensitized solar cells. *Nature*, 499(7458):316, 2013.

[4] Nam Joong Jeon, Jun Hong Noh, Young Chan Kim, Woon Seok Yang, Seungchan Ryu, and Sang Il Seok. Solvent engineering for high-performance inorganic–organic hybrid perovskite solar cells. *Nature materials*, 13(9):897, 2014.

[5] Michael M Lee, Joël Teuscher, Tsutomu Miyasaka, Takurou N Murakami, and Henry J Snaith. Efficient hybrid solar cells based on meso-superstructured organometal halide perovskites. *Science*, page 1228604, 2012.

[6] Shida Yang, Weifei Fu, Zhongqiang Zhang, Hongzheng Chen, and Chang-Zhi Li. Recent advances in perovskite solar cells: efficiency, stability and lead-free perovskite. *Journal of Materials Chemistry A*, 5(23):11462–11482, 2017.

[7] Samuel D Stranks, Giles E Eperon, Giulia Grancini, Christopher Menelaou, Marcelo JP Alcocer, Tomas Leijtens, Laura M Herz, Annamaria Petrozza, and Henry J Snaith. Electron-hole diffusion lengths exceeding 1 micrometer in an organometal trihalide perovskite absorber. *Science*, 342(6156):341–344, 2013.

[8] Guichuan Xing, Nripan Mathews, Shuangyong Sun, Swee Sien Lim, Yeng Ming Lam, Michael Grätzel, Subodh Mhaisalkar, and Tze Chien Sum. Long-range balanced electron-and hole-transport lengths in organic-inorganic ch3nh3pbi3. *Science*, 342(6156):344–347, 2013.

[9] CR Kagan, DB Mitzi, and CD Dimitrakopoulos. Organic-inorganic hybrid materials as semiconducting channels in thin-film field-effect transistors. *Science*, 286(5441):945–947, 1999.

[10] Konstantinos Chondroudis and David B Mitzi. Electroluminescence from an organic-inorganic perovskite incorporating a quaterthiophene dye within lead halide perovskite layers. *Chemistry of materials*, 11(11):3028–3030, 1999.

[11] Toshiaki Hattori, Takahiro Taira, Masanao Era, Tetsuo Tsutsui, and Shugu Saito. Highly efficient electroluminescence from a heterostructure device combined with emissive layered-perovskite and an electron-transporting organic compound. *Chemical physics letters*, 254(1-2):103–108, 1996.

[12] Li Na Quan, Mingjian Yuan, Riccardo Comin, Oleksandr Voznyy, Eric M Beauregard, Sjoerd Hoogland, Andrei Buin, Ahmad R Kirmani, Kui Zhao, Aram Amassian, et al. Ligand-stabilized reduced-dimensionality perovskites. *Journal of the American Chemical Society*, 138(8):2649–2655, 2016.

[13] Min-I Lee, Ana Barragán, Maya N Nair, Vincent LR Jacques, David Le Bolloc'h, Pierre Fertey, Khaoula Jemli, Ferdinand Lédée, Gaëlle Trippé-Allard, Emmanuelle Deleporte, et al. First determination of the valence band dispersion of ch3nh3pbi3 hybrid organic–inorganic perovskite. *Journal of Physics D: Applied Physics*, 50(26):26LT02, 2017.

[14] Zhesheng Chen, Min-i Lee, Zailan Zhang, Hiba Diab, Damien Garrot, Ferdinand Lédée, Pierre Fertey, Evangelos Papalazarou, Marino Marsi, Carlito Ponseca, et al. Time-resolved photoemission spectroscopy of electronic cooling and localization in ch 3 nh 3 pbi 3 crystals. *Physical Review Materials*, 1(4):045402, 2017.

[15] William Shockley and Hans J Queisser. Detailed balance limit of efficiency of p-n junction solar cells. *Journal of applied physics*, 32(3):510–519, 1961.

[16] Albert Polman, Mark Knight, Erik C Garnett, Bruno Ehrler, and Wim C Sinke. Photovoltaic materials: Present efficiencies and future challenges. *Science*, 352(6283):aad4424, 2016.

[17] Octavi E Semonin, Joseph M Luther, and Matthew C Beard. Quantum dots for next-generation photovoltaics. *Materials today*, 15(11):508–515, 2012.

[18] Woon Seok Yang, Jun Hong Noh, Nam Joong Jeon, Young Chan Kim, Seungchan Ryu, Jangwon Seo, and Sang Il Seok. High-performance photovoltaic perovskite layers fabricated through intramolecular exchange. *Science*, 348(6240):1234–1237, 2015.

[19] Martin A Green, Yoshihiro Hishikawa, Wilhelm Warta, Ewan D Dunlop, Dean H Levi, Jochen Hohl-Ebinger, and Anita WH Ho-Baillie. Solar cell efficiency tables (version 50). *Progress in Photovoltaics: Research and Applications*, 25(7):668–676, 2017.

[20] Makoto Tanaka, Mikio Taguchi, Takao Matsuyama, Toru Sawada, Shinya Tsuda, Shoichi Nakano, Hiroshi Hanafusa, and Yukinori Kuwano. Development of new a-si/c-si heterojunction solar cells: Acj-hit (artificially constructed junction-heterojunction with intrinsic thin-layer). *Japanese Journal of Applied Physics*, 31(11R):3518, 1992.

[21] Stefan Dauwe, Jan Schmidt, and Rudolf Hezel. Very low surface recombination velocities on p-and n-type silicon wafers passivated with hydrogenated amorphous silicon films. In *Photovoltaic Specialists Conference, 2002. Conference Record of the Twenty-Ninth IEEE*, pages 1246–1249. IEEE, 2002.

[22] Martin A Green. Solar cells: operating principles, technology, and system applications. 1982.

[23] Iván Santos, Marco Cazzaniga, Giovanni Onida, and Luciano Colombo. Atomistic study of the structural and electronic properties of a-si: H/c-si interfaces. *Journal of Physics: Condensed Matter*, 26(9):095001, 2014.

[24] R.A. Street. *Hydrogenated Amorphous Silicon*. Cambridge Solid State Science Series. Cambridge University Press, 2005.

[25] AM Salau. Fundamental absorption edge in pbi2: Ki alloys. *Solar Energy Materials*, 2(3):327–332, 1980.

[26] Akihiro Kojima, Kenjiro Teshima, Yasuo Shirai, and Tsutomu Miyasaka. Organometal halide perovskites as visible-light sensitizers for photovoltaic cells. *Journal of the American Chemical Society*, 131(17):6050–6051, 2009.

[27] Brian O'regan and Michael Grätzel. A low-cost, high-efficiency solar cell based on dye-sensitized colloidal tio2 films. *nature*, 353(6346):737, 1991.

[28] Qingfeng Dong, Yanjun Fang, Yuchuan Shao, Padhraic Mulligan, Jie Qiu, Lei Cao, and Jinsong Huang. Electron-hole diffusion lengths¿ 175 μm in solution-grown ch3nh3pbi3 single crystals. *Science*, 347(6225):967–970, 2015.

[29] Sarah M Vorpahl, Samuel D Stranks, Hirokazu Nagaoka, Giles E Eperon, Mark E Ziffer, Henry J Snaith, David S Ginger, et al. Impact of microstructure on local carrier lifetime in perovskite solar cells. *Science*, page aaa5333, 2015.

[30] Christian Wehrenfennig, Giles E Eperon, Michael B Johnston, Henry J Snaith, and Laura M Herz. High charge carrier mobilities and lifetimes in organolead trihalide perovskites. *Advanced materials*, 26(10):1584–1589, 2014.

[31] Hui-Seon Kim, Chang-Ryul Lee, Jeong-Hyeok Im, Ki-Beom Lee, Thomas Moehl, Arianna Marchioro, Soo-Jin Moon, Robin Humphry-Baker, Jun-Ho Yum, Jacques E Moser, et al. Lead iodide perovskite sensitized all-solid-state submicron thin film mesoscopic solar cell with efficiency exceeding 9%. *Scientific reports*, 2:591, 2012.

[32] Jeong-Hyeok Im, Chang-Ryul Lee, Jin-Wook Lee, Sang-Won Park, and Nam-Gyu Park. 6.5% efficient perovskite quantum-dot-sensitized solar cell. *Nanoscale*, 3(10):4088–4093, 2011.

[33] Hyung Do Kim, Hideo Ohkita, Hiroaki Benten, and Shinzaburo Ito. Photovoltaic performance of perovskite solar cells with different grain sizes. *Advanced materials*, 28(5):917–922, 2016.

[34] Michael Saliba, Taisuke Matsui, Konrad Domanski, Ji-Youn Seo, Amita Ummadisingu, Shaik M Zakeeruddin, Juan-Pablo Correa-Baena, Wolfgang R Tress, Antonio Abate, Anders Hagfeldt, et al. Incorporation of rubidium cations into perovskite solar cells improves photovoltaic performance. *Science*, 354(6309):206–209, 2016.

[35] Giles E Eperon, Samuel D Stranks, Christopher Menelaou, Michael B Johnston, Laura M Herz, and Henry J Snaith. Formamidinium lead trihalide: a broadly tunable perovskite for efficient planar heterojunction solar cells. *Energy & Environmental Science*, 7(3):982–988, 2014.

[36] Jacky Even, Laurent Pedesseau, M-A Dupertuis, J-M Jancu, and Claudine Katan. Electronic model for self-assembled hybrid organic/perovskite semiconductors: Reverse band edge electronic states ordering and spin-orbit coupling. *Physical Review B*, 86(20):205301, 2012.

[37] Sigismund Teunis Alexander George Melissen, Frédéric Labat, Philippe Sautet, and Tangui Le Bahers. Electronic properties of pbx 3 ch 3 nh 3 (x= cl, br, i) compounds for photovoltaic and photocatalytic applications. *Physical Chemistry Chemical Physics*, 17(3):2199–2209, 2015.

[38] Martin Labrune. *Silicon surface passivation and epitaxial growth on c-Si by low temperature plasma processes for high efficiency solar cells*. PhD thesis, Ecole Polytechnique, 2011.

[39] Alice Defresne. *Amélioration de la passivation de cellules solaires de silicium à hétérojonction grâce à l'implantation ionique et aux recuits thermiques*. PhD thesis, Université Paris-Saclay, 2016.

[40] Pere Roca i Cabarrocas, JB Chévrier, J Huc, A Lloret, JY Parey, and JPM Schmitt. A fully automated hot-wall multiplasma-monochamber reactor for thin film deposition. *Journal of Vacuum Science & Technology A: Vacuum, Surfaces, and Films*, 9(4):2331–2341, 1991.

[41] JPM Schmitt. Fundamental mechanisms in silane plasma decompositions and amorphous silicon deposition. *Journal of Non-Crystalline Solids*, 59:649–657, 1983.

[42] E Yablonovitch, DL Allara, CC Chang, T Gmitter, and TB Bright. Unusually low surface-recombination velocity on silicon and germanium surfaces. *Physical review letters*, 57(2):249, 1986.

[43] Karim Ouaras. *Mécanismes de formation et dynamique du transport des poussières de carbone et de tungstène dans un plasma micro-onde magnétisé et non-magnétisé*. PhD thesis, Université Paris 13, 2016.

[44] Ferdinand Lédée, Gaëlle Trippé-Allard, Hiba Diab, Pierre Audebert, Damien Garrot, Jean-Sébastien Lauret, and Emmanuelle Deleporte. Fast growth of monocrystalline thin films of 2d layered hybrid perovskite. *CrystEngComm*, 19(19):2598–2602, 2017.

[45] Dong Shi, Valerio Adinolfi, Riccardo Comin, Mingjian Yuan, Erkki Alarousu, Andrei Buin, Yin Chen, Sjoerd Hoogland, Alexander Rothenberger, Khabiboulakh Katsiev, et al. Low trap-state density and long carrier diffusion in organolead trihalide perovskite single crystals. *Science*, 347(6221):519–522, 2015.

[46] Václav Petříček, Michal Dušek, and Lukáš Palatinus. Crystallographic computing system jana2006: general features. *Zeitschrift für Kristallographie-Crystalline Materials*, 229(5):345–352, 2014.

[47] George M Sheldrick. Crystal structure refinement with shelxl. *Acta Crystallographica Section C: Structural Chemistry*, 71(1):3–8, 2015.

[48] ME Becquerel. Mémoire sur les effets électriques produits sous l'influence des rayons solaires. *Comptes rendus hebdomadaires des séances de l'Académie des Sciences*, 9:561–567, 1839.

[49] Albert Einstein. Über einen die erzeugung und verwandlung des lichtes betreffenden heuristischen gesichtspunkt. *Annalen der physik*, 322(6):132–148, 1905.

[50] Antonio Tejeda and Daniel Malterre. *Photoémission dans les solides*. EDP Sciences, 2016.

[51] Andrea Damascelli, Zahid Hussain, and Zhi-Xun Shen. Angle-resolved photoemission studies of the cuprate superconductors. *Reviews of modern physics*, 75(2):473, 2003.

[52] FJ Himpsel, FR McFeely, A Taleb-Ibrahimi, JA Yarmoff, and G Hollinger. Microscopic structure of the sio 2/si interface. *Physical review B*, 38(9):6084, 1988.

[53] K Siegbahn. Electron spectroscopy for atoms, molecules and condensed matter. Nobel Lectures, 1981.

[54] D Wo Turner and MI Al Jobory. Determination of ionization potentials by photoelectron energy measurement. *The Journal of Chemical Physics*, 37(12):3007–3008, 1962.

[55] Ray F Egerton. *Electron energy-loss spectroscopy in the electron microscope*. Springer Science & Business Media, 2011.

[56] M Pl Seah and WA Dench. Quantitative electron spectroscopy of surfaces: A standard data base for electron inelastic mean free paths in solids. *Surface and interface analysis*, 1(1):2–11, 1979.

[57] K Hirose, H Nohira, K Azuma, and T Hattori. Photoelectron spectroscopy studies of sio2/si interfaces. *Progress in Surface Science*, 82(1):3–54, 2007.

[58] J Rubio-Zuazo and GR Castro. Non-destructive compositional depth profile analysis by hard x-ray photoelectron spectroscopy. 100(1):012042, 2008.

[59] James H Scofield. Theoretical photoionization cross sections from 1 to 1500 kev. Technical report, California Univ., Livermore. Lawrence Livermore Lab., 1973.

[60] JJ Yeh and I Lindau. Atomic subshell photoionization cross sections and asymmetry parameters: 1â©œ zâ©œ 103. *Atomic data and nuclear data tables*, 32(1):1–155, 1985.

[61] JB Pendry. Theory of inverse photoemission. *Journal of Physics C: Solid State Physics*, 14(9):1381, 1981.

[62] Neville V Smith. Inverse photoemission. *Reports on Progress in Physics*, 51(9):1227, 1988.

[63] Peter W Erdman and Edward C Zipf. Low-voltage, high-current electron gun. *Review of Scientific Instruments*, 53(2):225–227, 1982.

[64] Yu-Pu Lin. *Functionalization of two-dimensional nanomaterials based on graphene*. PhD thesis, Aix Marseille Université, 2014.

[65] Volker Dose. Momentum-resolved inverse photoemission. *Surface Science Reports*, 5(8):337–378, 1985.

[66] Franz-Josef Himpsel. Inverse photoemission from semiconductors. *Surface Science Reports*, 12(1):3–48, 1990.

[67] I Schäfer, M Schlüter, and M Skibowski. Conduction-band structure of graphite studied by combined angle-resolved inverse photoemission and target current spectroscopy. *Physical Review B*, 35(14):7663, 1987.

[68] I Adawi. Theory of the surface photoelectric effect for one and two photons. *Physical Review*, 134(3A):A788, 1964.

[69] GD Mahan. Theory of photoemission in simple metals. *Physical Review B*, 2(11):4334, 1970.

[70] WL Schaich and NW Ashcroft. Theory of photoemission. *Solid State Communications*, 8(23):1959–1963, 1970.

[71] Carl Neil Berglund and William Edward Spicer. Photoemission studies of copper and silver: theory. *Physical Review*, 136(4A):A1030, 1964.

[72] JB Pendry. Theory of photoemission. *Surface Science*, 57(2):679–705, 1976.

[73] Eleftherios N Economou. *Green's functions in quantum physics*, volume 3. Springer, 1983.

[74] Kyozaburo Kambe. Theory of low-energy electron diffraction. *Zeitschrift für Naturforschung A*, 22(3):322–330, 1967.

[75] JM MacLaren, S Crampin, DD Vvedensky, and JB Pendry. Layer korringa-kohn-rostoker technique for surface and interface electronic properties. *Physical Review B*, 40(18):12164, 1989.

[76] Jan Minar. 13 theoretical description of arpes: The one-step model. *DMFT at 25: Infinite Dimensions: Lecture Notes of the Autumn School on Correlated Electrons 2014*, 4, 2014.

[77] Hubert Ebert, Diemo Koedderitzsch, and Jan Minar. Calculating condensed matter properties using the kkr-green's function method—recent developments and applications. *Reports on Progress in Physics*, 74(9):096501, 2011.

[78] H Ebert et al. The munich spr-kkr package, version 7.7, h. ebert et al, 2017.

[79] Antonios Gonis and William H Butler. *Multiple scattering in solids*. Springer Science & Business Media, 2012.

[80] J Korringa. On the calculation of the energy of a bloch wave in a metal. *Physica*, 13(6-7):392–400, 1947.

[81] Wo Kohn and No Rostoker. Solution of the schrödinger equation in periodic lattices with an application to metallic lithium. *Physical Review*, 94(5):1111, 1954.

[82] JL Beeby. The density of electrons in a perfect or imperfect lattice. 302(1468):113–136, 1967.

[83] JS Faulkner. Scattering theory and cluster calculations. *Journal of Physics C: Solid State Physics*, 10(23):4661, 1977.

[84] JS Faulkner. Multiple-scattering approach to band theory. *Physical Review B*, 19(12):6186, 1979.

[85] BL Györffy and GM Stocks. First principles band theory for random metallic alloys. In *Electrons in Disordered Metals and at Metallic Surfaces*, pages 89–192. Springer, 1979.

[86] JS Faulkner and GM Stocks. Calculating properties with the coherent-potential approximation. *Physical Review B*, 21(8):3222, 1980.

[87] Yositaka Onodera and Makoto Okazaki. Relativistic theory for energy-band calculation. *Journal of the Physical Society of Japan*, 21(7):1273–1281, 1966.

[88] Paul Strange, H Ebert, JB Staunton, and Balazs L Gyorffy. A relativistic spin-polarised multiple-scattering theory, with applications to the calculation of the electronic structure of condensed matter. *Journal of Physics: Condensed Matter*, 1(18):2959, 1989.

[89] Paul Strange. *Relativistic Quantum Mechanics: with applications in condensed matter and atomic physics*. Cambridge University Press, 1998.

[90] H Ebert. Fully relativistic band structure calculations for magnetic solids-formalism and application. In *Electronic Structure and Physical Properies of Solids*, pages 191–246. Springer, 1999.

[91] E Tamura. Relativistic single-site green function for general potentials. *Physical Review B*, 45(7):3271, 1992.

[92] Luca Perfetti, Panagiotis A Loukakos, Martin Lisowski, Uwe Bovensiepen, Martin Wolf, Helmuth Berger, Silke Biermann, and Antoine Georges. Femtosecond dynamics of electronic states in the mott insulator 1T-TaS_2 by time resolved photoelectron spectroscopy. *New Journal of Physics*, 10(5):053019, 2008.

[93] H Petek and S Ogawa. Femtosecond time-resolved two-photon photoemission studies of electron dynamics in metals. *Progress in surface science*, 56(4):239–310, 1997.

[94] Fengyou Wang, Yanbo Gao, Zhenyu Pang, Lili Yang, and Jinghai Yang. Insights into the role of the interface defects density and the bandgap of the back surface field for efficient p-type silicon heterojunction solar cells. *RSC Advances*, 7(43):26776–26782, 2017.

[95] Wolfgang SM Werner, Werner Smekal, and Cedric J Powell. Nist database for the simulation of electron spectra for surface analysis (sessa). In *Version 1.3, Standard Reference Program Database 100, US Department of Commerce*. National Institute of Standards and Technology Gaithersburg, MD, 2011.

[96] Takahiro Maruyama and Shigeya Naritsuka. Initial growth process of carbon nanotubes in surface decomposition of sic. In *Carbon Nanotubes-Synthesis, Characterization, Applications*. InTech, 2011.

[97] Bingbing Liu, Lingqin Huang, Qiaozhi Zhu, Fuwen Qin, and Dejun Wang. Chemical and electronic passivation of 4h-sic surface by hydrogen-nitrogen mixed plasma. *Applied Physics Letters*, 104(20):202101, 2014.

[98] G Le Lay, V Yu Aristov, and M Fontaine. Surface core-level shifts of si (111) 7x7. *Le Journal de Physique IV*, 4(C9):C9–213, 1994.

[99] A Redondo, WA Goddard III, CA Swarts, and TC McGill. Oxidation of silicon surfaces. *Journal of Vacuum Science and Technology*, 19(3):498–501, 1981.

[100] GF Cerofolini, C Galati, and L Renna. Si 2p xps spectrum of the hydrogen-terminated (100) surface of device-quality silicon. *Surface and interface analysis*, 35(12):968–973, 2003.

[101] Bibhu P Swain and Nong M Hwang. Study of structural and electronic environments of hydrogenated amorphous silicon carbonitride (a-sicn: H) films deposited by hot wire chemical vapor deposition. *Applied Surface Science*, 254(17):5319–5322, 2008.

[102] U Köster. Crystallization of amorphous silicon films. *Physica status solidi (a)*, 48(2):313–321, 1978.

[103] Joseph C Woicik. *Hard X-ray Photoelectron Spectroscopy (HAXPES)*. Springer, 2016.

[104] G Grancini, C Roldán-Carmona, I Zimmermann, E Mosconi, X Lee, D Martineau, S Narbey, F Oswald, F De Angelis, M Graetzel, et al. One-year stable perovskite solar cells by 2d/3d interface engineering. *Nature communications*, 8:15684, 2017.

[105] J-C Blancon, Hsinhan Tsai, Wanyi Nie, Costas C Stoumpos, Laurent Pedesseau, Claudine Katan, Mikaël Kepenekian, Chan Myae Myae Soe, Kannatassen Appavoo, Matthew Y Sfeir, et al. Extremely efficient internal exciton dissociation through edge states in layered 2d perovskites. *Science*, page eaal4211, 2017.

[106] Ian C Smith, Eric T Hoke, Diego Solis-Ibarra, Michael D McGehee, and Hemamala I Karunadasa. A layered hybrid perovskite solar-cell absorber with enhanced moisture stability. *Angewandte Chemie*, 126(42):11414–11417, 2014.

[107] Hsinhan Tsai, Wanyi Nie, Jean-Christophe Blancon, Constantinos C Stoumpos, Reza Asadpour, Boris Harutyunyan, Amanda J Neukirch, Rafael Verduzco, Jared J Crochet, Sergei Tretiak, et al. High-efficiency two-dimensional ruddlesden–popper perovskite solar cells. *Nature*, 536(7616):312, 2016.

[108] Fan Zheng, Liang Z Tan, Shi Liu, and Andrew M Rappe. Rashba spin–orbit coupling enhanced carrier lifetime in ch3nh3pbi3. *Nano letters*, 15(12):7794–7800, 2015.

[109] Peng Zhang, P Richard, T Qian, Y-M Xu, X Dai, and H Ding. A precise method for visualizing dispersive features in image plots. *Review of Scientific Instruments*, 82(4):043712, 2011.

[110] Wei Geng, Le Zhang, Yan-Ning Zhang, Woon-Ming Lau, and Li-Min Liu. First-principles study of lead iodide perovskite tetragonal and orthorhombic phases for photovoltaics. *The Journal of Physical Chemistry C*, 118(34):19565–19571, 2014.

[111] T Umebayashi, K Asai, T Kondo, and A Nakao. Electronic structures of lead iodide based low-dimensional crystals. *Physical Review B*, 67(15):155405, 2003.

[112] Tom Baikie, Yanan Fang, Jeannette M Kadro, Martin Schreyer, Fengxia Wei, Subodh G Mhaisalkar, Michael Graetzel, and Tim J White. Synthesis and crystal chemistry of the hybrid perovskite (ch 3 nh 3) pbi 3 for solid-state sensitised solar cell applications. *Journal of Materials Chemistry A*, 1(18):5628–5641, 2013.

[113] Paolo Umari, Edoardo Mosconi, and Filippo De Angelis. Relativistic gw calculations on ch 3 nh 3 pbi 3 and ch 3 nh 3 sni 3 perovskites for solar cell applications. *Scientific reports*, 4:4467, 2014.

[114] George C Papavassiliou, IB Koutselas, A Terzis, and M-H Whangbo. Structural and electronic properties of the natural quantum-well system (c6h5ch2ch2nh3) 2sni4. *Solid state communications*, 91(9):695–698, 1994.

[115] Wan-Jian Yin, Ji-Hui Yang, Joongoo Kang, Yanfa Yan, and Su-Huai Wei. Halide perovskite materials for solar cells: a theoretical review. *Journal of Materials Chemistry A*, 3(17):8926–8942, 2015.

[116] Federico Brivio, Keith T Butler, Aron Walsh, and Mark Van Schilfgaarde. Relativistic quasiparticle self-consistent electronic structure of hybrid halide perovskite photovoltaic absorbers. *Physical Review B*, 89(15):155204, 2014.

[117] Anna Amat, Edoardo Mosconi, Enrico Ronca, Claudio Quarti, Paolo Umari, Md K Nazeeruddin, Michael Grätzel, and Filippo De Angelis. Cation-induced band-gap tuning in organohalide perovskites: interplay of spin–orbit coupling and octahedra tilting. *Nano letters*, 14(6):3608–3616, 2014.

[118] Weiwei Gao, Xiang Gao, Tesfaye A Abtew, Yi-Yang Sun, Shengbai Zhang, and Peihong Zhang. Quasiparticle band gap of organic-inorganic hybrid perovskites: Crystal structure, spin-orbit coupling, and self-energy effects. *Physical Review B*, 93(8):085202, 2016.

[119] Fan Zheng, Hiroyuki Takenaka, Fenggong Wang, Nathan Z Koocher, and Andrew M Rappe. First-principles calculation of the bulk photovoltaic effect in ch3nh3pbi3 and ch3nh3pbi3–x cl x. *The journal of physical chemistry letters*, 6(1):31–37, 2014.

[120] Youwei Wang, Yubo Zhang, Peihong Zhang, and Wenqing Zhang. High intrinsic carrier mobility and photon absorption in the perovskite ch 3 nh 3 pbi 3. *Physical Chemistry Chemical Physics*, 17(17):11516–11520, 2015.

[121] Yuping He and Giulia Galli. Perovskites for solar thermoelectric applications: A first principle study of ch3nh3ai3 (a= pb and sn). *Chemistry of Materials*, 26(18):5394–5400, 2014.

[122] Benjamin J Foley, Daniel L Marlowe, Keye Sun, Wissam A Saidi, Louis Scudiero, Mool C Gupta, and Joshua J Choi. Temperature dependent energy levels of methylammonium lead iodide perovskite. *Applied Physics Letters*, 106(24):243904, 2015.

[123] Rebecka Lindblad, Dongqin Bi, Byung-wook Park, Johan Oscarsson, Mihaela Gorgoi, Hans Siegbahn, Michael Odelius, Erik MJ Johansson, and Håkan Rensmo. Electronic structure of tio2/ch3nh3pbi3 perovskite solar cell interfaces. *The journal of physical chemistry letters*, 5(4):648–653, 2014.

[124] Philip Schulz, Eran Edri, Saar Kirmayer, Gary Hodes, David Cahen, and Antoine Kahn. Interface energetics in organo-metal halide perovskite-based photovoltaic cells. *Energy & Environmental Science*, 7(4):1377–1381, 2014.

[125] Yukihiko Kawamura, Hiroyuki Mashiyama, and Katsuhiko Hasebe. Structural study on cubic–tetragonal transition of ch3nh3pbi3. *Journal of the Physical Society of Japan*, 71(7):1694–1697, 2002.

[126] Robin Ohmann, Luis K Ono, Hui-Seon Kim, Haiping Lin, Michael V Lee, Youyong Li, Nam-Gyu Park, and Yabing Qi. Real-space imaging of the atomic structure of organic–inorganic perovskite. *Journal of the American Chemical Society*, 137(51):16049–16054, 2015.

[127] Limin She, Meizhuang Liu, and Dingyong Zhong. Atomic structures of ch3nh3pbi3 (001) surfaces. *ACS nano*, 10(1):1126–1131, 2015.

[128] J Voit, L Perfetti, F Zwick, H Berger, G Margaritondo, G Grüner, H Höchst, and M Grioni. Electronic structure of solids with competing periodic potentials. *Science*, 290(5491):501–503, 2000.

[129] D Malterre, B Kierren, Y Fagot-Revurat, S Pons, A Tejeda, C Didiot, H Cercellier, and A Bendounan. Arpes and sts investigation of shockley states in thin metallic films and periodic nanostructures. *New Journal of Physics*, 9(10):391, 2007.

[130] C Didiot, A Tejeda, Y Fagot-Revurat, V Repain, B Kierren, S Rousset, and D Malterre. Interacting quantum box superlattice by self-organized co nanodots on au (788). *Physical Review B*, 76(8):081404, 2007.

[131] Jérôme Faure, J Mauchain, E Papalazarou, W Yan, J Pinon, M Marsi, and Luca Perfetti. Full characterization and optimization of a femtosecond ultraviolet laser source for time and angle-resolved photoemission on solid surfaces. *Review of Scientific Instruments*, 83(4):043109, 2012.

[132] Martin A Green, Yajie Jiang, Arman Mahboubi Soufiani, and Anita Ho-Baillie. Optical properties of photovoltaic organic–inorganic lead halide perovskites. *The journal of physical chemistry letters*, 6(23):4774–4785, 2015.

[133] Haiming Zhu, Kiyoshi Miyata, Yongping Fu, Jue Wang, Prakriti P Joshi, Daniel Niesner, Kristopher W Williams, Song Jin, and X-Y Zhu. Screening in crystalline liquids protects energetic carriers in hybrid perovskites. *Science*, 353(6306):1409–1413, 2016.

[134] Daniel Niesner, Haiming Zhu, Kiyoshi Miyata, Prakriti P Joshi, Tyler JS Evans, Bryan J Kudisch, M Tuan Trinh, Manuel Marks, and X-Y Zhu. Persistent energetic electrons in methylammonium lead iodide perovskite thin films. *Journal of the American Chemical Society*, 138(48):15717–15726, 2016.

[135] Hiroshi Tanimura, Jun'ichi Kanasaki, Katsumi Tanimura, Jelena Sjakste, Nathalie Vast, Matteo Calandra, and Francesco Mauri. Formation of hot-electron ensembles quasiequilibrated in momentum space by ultrafast momentum scattering of highly excited hot electrons photoinjected into the γ valley of gaas. *Physical Review B*, 93(16):161203, 2016.

[136] Federico Brivio, Jarvist M Frost, Jonathan M Skelton, Adam J Jackson, Oliver J Weber, Mark T Weller, Alejandro R Goni, Aurélien MA Leguy, Piers RF Barnes, and Aron Walsh. Lattice dynamics and vibrational spectra of the orthorhombic, tetragonal, and cubic phases of methylammonium lead iodide. *Physical Review B*, 92(14):144308, 2015.

[137] Daniel B Straus, Sebastian Hurtado Parra, Natasha Iotov, Julian Gebhardt, Andrew M Rappe, Joseph E Subotnik, James M Kikkawa, and Cherie R Kagan. Direct observation of electron–phonon coupling and slow vibrational relaxation in organic–inorganic hybrid perovskites. *Journal of the American Chemical Society*, 138(42):13798–13801, 2016.

[138] Ye Yang, Yong Yan, Mengjin Yang, Sukgeun Choi, Kai Zhu, Joseph M Luther, and Matthew C Beard. Low surface recombination velocity in solution-grown ch 3 nh 3 pbbr 3 perovskite single crystal. *Nature communications*, 6:7961, 2015.

[139] Rebecca L Milot, Giles E Eperon, Henry J Snaith, Michael B Johnston, and Laura M Herz. Temperature-dependent charge-carrier dynamics in ch3nh3pbi3 perovskite thin films. *Advanced Functional Materials*, 25(39):6218–6227, 2015.

[140] Khaoula Jemli, Hiba Diab, Ferdinand Lédée, Gaelle Trippé-Allard, Damien Garrot, Bernard Geffroy, Jean-Sébastien Lauret, Pierre Audebert, and Emmanuelle Deleporte. Using low temperature photoluminescence spectroscopy to investigate ch3nh3pbi3 hybrid perovskite degradation. *Molecules*, 21(7):885, 2016.

[141] I Deretzis, A Alberti, G Pellegrino, E Smecca, F Giannazzo, N Sakai, T Miyasaka, and A La Magna. Atomistic origins of ch3nh3pbi3 degradation to pbi2 in vacuum. *Applied Physics Letters*, 106(13):131904, 2015.

List of Figures

List of Tables

université PARIS-SACLAY
ÉCOLE DOCTORALE
Physique en île-de-France (EDPIF)

Titre : Structure atomique, états électroniques et dynamique de relaxation dans des matériaux et interfaces photovoltaïques par spectroscopies connexes à la photoémission

Mots clés : photovoltaïque, interfaces, propriétés électroniques, structure atomique, dynamique ultra-rapide

Résumé : L'efficacité du processus photovoltaïque dépend du matériau actif à travers sa structure de bandes et la dynamique des porteurs de charge. Dans cette thèse, nous avons relié les propriétés électroniques et la dynamique de relaxation à la structure atomique des matériaux utilisés dans deux technologies de cellules solaires: celle à base d'hétérojunction de silicium, et celle à base de pérovskites hybrides organique-inorganique.

Dans les cellules solaires de silicium, nous avons analysé l'influence des défauts sur les propriétés électroniques des hétérojunction a-Si:H/c-Si par des spectroscopies des niveaux de coeur et de la bande de valence. En particulier, nous avons quantifié le nombre de liaisons pendantes induites dans la couche a-Si:H par irradiation, et nous avons identifié les états électroniques qui leur sont associés. Enfin nous avons expliqué les transitions précédemment observées par photoluminescence.

Dans les cellules solaires à pérovskite hybride, nous avons corrélé la structure atomique, la structure électronique et la dynamique électronique pour des pérovskites bi- et tridimensionnelles. Dans ce but nous avons utilisé tout un panel de techniques complémentaires: diffraction des rayons X, spectroscopie de photoémission résolue en angle, spectroscopie de photoémission inverse et photoémission à deux photons résolue en temps. Pour la pérovskite bidimensionnelle $(C_6H_5C_2H_4NH_3)_2PbI_4$, nous avons déterminé expérimentalement les bandes de valence et de conduction et nous les avons comparées aux simulations de la fonction spectrale.

Pour la pérovskite tridimensionnelle $CH_3NH_3PbI_3$, nous avons aussi déterminé les structures de bande expérimentale et simulée. Des signatures spectrales très larges ont été observées expérimentalement, ce qui relaxe les conditions de transition optique avec un impact éventuel sur l'efficacité des cellules solaires. Aussi lien dans les expériences que dans les calculs, nous observons que le poids spectral suit une périodicité cubique alors que le système est structurellement dans une phase tétragonale. Cette contradiction apparente s'explique par la largeur spectrale des bandes, qui cache le repliement dû à la distorsion tétragonale. En ce qui concerne la dynamique de relaxation, nous avons observé que les porteurs photoexcités se thermalisent dans une échelle de temps subpicoseconde par couplage aux vibrations des cations organiques. À des échelles de temps plus longues (10 ~ 100 picosecondes), la diffusion électronique contrôle la dynamique. Cette dynamique est affectée par les défauts induits par recuit, qui localisent les électrons photoexcités pendant plus de 300 picosecondes.

Université Paris-Saclay
Espace Technologique / Immeuble Discovery
Route de l'Orme aux Merisiers RD 128 / 91190 Saint-Aubin, France

université PARIS-SACLAY
ÉCOLE DOCTORALE
Physique en île-de-France (EDPIF)

Title : Atomic structure, electronic states and relaxation dynamics in photovoltaic materials and interfaces from photoemission-related spectroscopies

Keywords : photovoltaic, interfaces, electronic properties, structure atomic, ultra-fast dynamics

Abstract : The efficiency of the photovoltaic process depends on the electronic band structure of the active material and the charge carrier dynamics. In this thesis, we have studied how these issues are related to the atomic structure of the materials for two types of technologies of solar cells, namely silicon heterojunction solar cells, and hybrid organic-inorganic perovskite solar cells.

In silicon heterojunction solar cells, we have analyzed the impact of defects on the electronic properties of amorphous silicon heterojunction (a-Si:H/c-Si) by core level and valence band spectroscopies. In particular, we have quantified the number of dangling bonds in the a-Si:H layer upon irradiation, we have identified the electronic states associated to them, and have understood the transitions previously observed by photoluminescence.

In perovskite solar cells, we have correlated the atomic structure, the electronic structure and the electronic dynamics for two- and three-dimensional hybrid organic-inorganic perovskites. We have used for this goal a whole panel of complementary techniques: X-ray diffraction, angle-resolved photoemission spectroscopy, inverse photoemission spectroscopy, and time-resolved two-photon photoemission. In the two-dimensional perovskite $(C_6H_5C_2H_4NH_3)_2PbI_4$, the valence and conduction bands have been determined experimentally and compared to spectral function simulations.

In the three-dimensional perovskite $CH_3NH_3PbI_3$, we have again determined the band structure and simulated it. Very broad spectral features have been experimentally observed, which relax the optical transition conditions impacting in the solar cell efficiencies. In both experiments and calculations, we observe that the spectral weight follows a cubic periodicity while the system is structurally in the tetragonal phase. This apparent contradiction is explained by the band broadness, which hides the band folding of the tetragonal distortion. As for the relaxation dynamics, we have observed that the photoexcited carriers thermalize in a subpicosecond time scale through the coupling to organic cation vibrations. At longer timescales (10~100 picoseconds), the electron diffusion controls the dynamics. This dynamics is affected by the annealing-induced defects, which localize the photoexcited electrons for more than 300 picoseconds.

Université Paris-Saclay
Espace Technologique / Immeuble Discovery
Route de l'Orme aux Merisiers RD 128 / 91190 Saint-Aubin, France